

The work aims to provide a comparative study of various procedures that define the Element-free Galerkin method(EFGM) and the modifications or alterations that took place to improve the workability of EFGM. Every part of EFG process has been described in a different chapter and conclusions are provided in the end to help readers comprehend the improvements and alterations in the process. The book covers all the important literature works related to the analysis of fracture problems using EFGM.

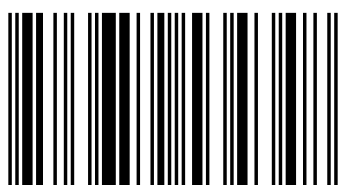
Meshfree Techniques And Fracture



Sahil Garg
Mohit Pant
Ajay Kumar

EFGM: Evolution and Applications With Respect To Fracture Problems

A Comparative Anthology



978-3-659-53434-8

Garg, Pant, Kumar

LAP LAMBERT
Academic Publishing

**Sahil Garg
Mohit Pant
Ajay Kumar**

**EFGM: Evolution and Applications With Respect To Fracture
Problems**

**Sahil Garg
Mohit Pant
Ajay Kumar**

**EFGM: Evolution and Applications
With Respect To Fracture Problems**

A Comparative Anthology

LAP LAMBERT Academic Publishing

Impressum / Imprint

Bibliografische Information der Deutschen Nationalbibliothek: Die Deutsche Nationalbibliothek verzeichnet diese Publikation in der Deutschen Nationalbibliografie; detaillierte bibliografische Daten sind im Internet über <http://dnb.d-nb.de> abrufbar.

Alle in diesem Buch genannten Marken und Produktnamen unterliegen warenzeichen-, marken- oder patentrechtlichem Schutz bzw. sind Warenzeichen oder eingetragene Warenzeichen der jeweiligen Inhaber. Die Wiedergabe von Marken, Produktnamen, Gebrauchsnamen, Handelsnamen, Warenbezeichnungen u.s.w. in diesem Werk berechtigt auch ohne besondere Kennzeichnung nicht zu der Annahme, dass solche Namen im Sinne der Warenzeichen- und Markenschutzgesetzgebung als frei zu betrachten wären und daher von jedermann benutzt werden dürften.

Bibliographic information published by the Deutsche Nationalbibliothek: The Deutsche Nationalbibliothek lists this publication in the Deutsche Nationalbibliografie; detailed bibliographic data are available in the Internet at <http://dnb.d-nb.de>.

Any brand names and product names mentioned in this book are subject to trademark, brand or patent protection and are trademarks or registered trademarks of their respective holders. The use of brand names, product names, common names, trade names, product descriptions etc. even without a particular marking in this work is in no way to be construed to mean that such names may be regarded as unrestricted in respect of trademark and brand protection legislation and could thus be used by anyone.

Coverbild / Cover image: www.ingimage.com

Verlag / Publisher:

LAP LAMBERT Academic Publishing
ist ein Imprint der / is a trademark of
ICS Morebooks! Marketing SRL
4, Industriala street, 3100 Balti, Republic of Moldova
Email: info@omnascriptum.com

Herstellung: siehe letzte Seite /

Printed at: see last page

ISBN: 978-3-659-53434-8

Zugl. / Approved by: National Institute of Technology, Hamirpur, 2017

Copyright © Sahil Garg, Mohit Pant, Ajay Kumar

Copyright © 2017 ICS Morebooks! Marketing SRL

Alle Rechte vorbehalten. / All rights reserved. Balti2017

**EFGM: Evolution and Applications With Respect To Fracture
Problems**

**This book is dedicated to my parents because they are the reason I
am here and make what I
am doing meaningful.**

Acknowledgements

First of all, I take this wonderful opportunity to offer my sincere gratitude to my mentor and supervisor, **Dr. Mohit Pant**, for his general advice, inspiring supervision and continuous encouragement throughout the course of my research. He is the best teacher I have ever found. His in-depth knowledge in different areas of engineering such as fracture mechanics, computational solid mechanics and numerical analysis has always been valuable for me. He has always been available for discussions of new findings and new ideas in spite of his busy schedule. I will always remain indebted to him for his comments, advices and valuable suggestions provided by him during the entire course of my research. I thank him for the valuable time that he devoted to me and working with him was indeed an unforgettable experience of my life.

Finally, I owe a great deal of appreciation to my family members, especially my parents **Sanjay Garg and Sunita Garg**, for their encouragement and unconditional help at every stage of my personal and academic life. I owe my parents everything of what I am today. A very special thanks to my beloved wife **Dr. Aeshwarya Garg** for her love and moral support. This work is by all means is also devoted to my brother **Sudhanshu** and my dear sister-in-law **Bhavya** for their continuous care and support them because they are the reason I am here and make what I am doing meaningful.

Thanks to Lord almighty God for bestowing me with the courage and vision to contribute to this eminent field of research.

Abstract

The anthology presented in this work is aimed to present a concise overview about the procedural development of element free Galerkin method (EFGM) for analyzing problems in the field of fracture mechanics. The work covers all the modifications in the methods for construction of shape functions and various methods employed for enforcement of boundary conditions with a prime focus on elaborating the mathematical modifications that took place in the earliest work in the area of fracture mechanics using EFGM. Various methods to deal with strong and weak discontinuities are also described. For improving the results and accuracy coupling of EFGM with other mesh based and meshless methods is presented. The modifications and comparison of interaction integral approach for calculation of stress intensity factors(SIFs) for various types of loadings is specified. All the sections dealing with various improvements in EFGM are concluded with a comparative statement to enable researchers select best parameters for an EFG simulation. The work is concluded with results obtained by using various EFG modifications encompassing all major variations related to fracture problems.

Keywords: *Meshless methods, EFGM, Fracture mechanics, Crack, Enrichment*

Table of Contents

CONTENTS	PAGE NO.
Dedication	2
Acknowledgements	3
Abstract	4
Chapter 1 Introduction To Meshless Methods	7
1.1 Introduction	7
1.1.1 Classification of Meshless Methods	9
1.2 Element Free Galerkin Method	11
1.2.1. Basic Approximations	11
1.2.2. Kernel (Weight) Function	12
1.2.3. Completeness	12
1.2.4. Partition Of Unity	12
Chapter 2 Construction Of Shape Functions	13
2.1 Methods For Construction Of Shape Functions	13
2.1.1 Moving Least Square (MLS) Approximation	13
2.1.1.1 Efficient Shape Function Calculation	18
2.1.1.2 Orthogonal Basis Functions For MLS Interpolant	19
2.1.1.3 Weight Function	21
2.1.1.4 Enriched Basis Function	26
2.1.2 Radial Basis Function For Construction Of Shape Function	27
2.2 Conclusion	30
Chapter 3 Enforcing Boundary Conditions In EFGM	31
3.1 Enforcement Of Essential Boundary Conditions	31
3.1.1 Lagrange Multiplier Method	31
3.1.2 Modified Variational Principle	34
3.1.3 Penalty Function	35
3.1.4 Transformation Method	35
3.2 Conclusion	39

Chapter 4 Discontinuity Modeling In EFGM	40
4.1 Discontinuities	40
4.1.1 Modeling Of Weak Discontinuities	40
4.1.2 Modeling Of Strong Discontinuities	47
4.2 Conclusion	67
Chapter 5 Modifications In EFGM	69
5.1 Coupled Techniques	69
5.1.1 Coupled Finite Element And Element Free Galerkin Method (FE-EFG)	70
5.1.2 Coupled Fractal Finite Element And Element Free Galerkin Method	71
5.1.3 Coupled Radial Point Interpolation And Element Free Galerkin Method	72
5.2 Optimized Element Free Galerkin Method (OEGF)	74
5.3 Conclusion	80
Chapter 6 Numerical Integration And Stress Intensity Factor Calculation In EFGM	81
6.1 Numerical Integration	81
6.2 Calculation Of Stress Intensity Factor For Various Cases	82
6.3 Conclusion	89
Chapter 7 Numerical Results	90
Numerical Examples	90
Chapter 8 Conclusions And Future Scope	104
8.1 Conclusions	104
8.2 Future Scope	105
References	107

CHAPTER 1

INTRODUCTION TO MESHLESS METHODS

1.1 Introduction

Computational fracture mechanics has always presented a tough challenge to researchers in terms of accuracy in results and capturing stress field oscillations near the crack tip area. The finite element method(FEM) has been extensively used for many problems related to fracture mechanics. It has proven its prowess as well, but it is not without limitations. Due to the limitations of this method in meshing moving boundary problems, distorted and low quality meshes producing erroneous results a hard labor and excessive time is required.

Moreover, due to the primitive structure of the classical mesh-based methods, they are not well suited to treat problems with discontinuities that fall out of alignment with element edges. One scheme to deal with moving discontinuities in mesh-based methods is remeshing or discontinuous enrichment. However, remeshing is a costly and tedious task also it is difficult in three dimensions and requires projection of quantities between successive meshes and substantial degradation of accuracy. A substitute to remeshing with a finite element background is the extended finite element method (XFEM) [1–5] enriches the approximation space so that weak and strong discontinuities can be captured. Amelioration of results for mesh based methods led to the development of Meshless/Meshfree Methods (MMs). In MMs approximation is built with the help of nodal points only. The first meshless method is smooth particle hydrodynamics (SPH) [6–8] and it was able to solve problems of fluid dynamics, heat conduction, machining [9,10] and solid mechanics [11] with ease. While SPH and their corrected adaptations were strong form based, other methods were developed in the 1990s, based on a weak form. Major utilization of these methods was in solid mechanics. The element-free Galerkin (EFG) method [12] was developed in 1994 and was one of the first meshless methods that used global weak form as its basic structure. The element-free Galerkin (EFG) method has been most widely used meshless method in the field of fracture mechanics [13–17] and has successfully solved a variety of problems whether under various loadings or conditions immaculately.

The earliest development of EFG method involved the construction of shape function using moving least square (MLS) approximation [18] and Lagrange's multiplier [19] approach for enforcement of boundary conditions [20,21]. A problem encountered with MLS methodology was that a set of linear algebraic equations have to be solved at every node at which the primary dependent variable are calculated [22], henceforth the moment matrix has to be inverted at every Gauss point when discrete equations are assembled. This problem was solved by constructing weighted orthogonal basis function [23,24] for MLS interpolants using Gram Schmidt-orthogonalization process [25]. The MLS shape functions lack Kronecker delta property hence enforcement of boundary conditions is difficult, also the use of Lagrange multiplier method leads to an escalation in number of unknowns which is troublesome for the solver, therefore, to circumvent the use of Lagrange multiplier along with maintaining the satisfaction of essential boundary conditions modified variational principle was used in which Lagrange multipliers were replaced by their physical meaning. The modified variational principle provided a set of banded equations but these equations are not necessarily positive-definite also it was somewhat less accurate than Lagrange multiplier method hence enforcement of boundary conditions was done by penalty method [26,27] which leads to banded positive-definite equations. Recently radial basis function [28–30] in conjugation with MLS approach has been used for the construction of shape function but failed to reach the desired accuracy in results. Efforts have been made to improve EFGM procedures involving the construction of shape function [23,24,31] and enforcement of essential boundary conditions[26,27]. Apart from these some researchers tried to improve the EFG solution by working on selectable parameters [32,33] but did not comment on range or standards that can be selected for these parameters.

In analyzing fracture problems discontinuities can be present in the domain the form of strong or weak discontinuities. Cordes and Moran [34,35] in their work presented two methods to deal with material discontinuity, later on modifications were made by introduction of jump function [16,36–39] approach and implementing signed distance enrichment functions. Fleming et. al [40] provided the enriched EFG formulations for analysis of fracture problems and Belytschko et. al [41] developed smoothening techniques for treating cracks and holes in the

domain. Recently level set methodology has also been employed to analyze fatigue crack growth using EFGM[17].

In fracture mechanics, the region around the crack tip called the singularity dominated zone is the major area of concern for capturing stress field oscillations. The computational time engineering effort required for such analysis should be minimized to save the overall cost of the project. Hence, to save time, minimize engineering effort and to overcome the inherent flaws of EFGM, EFG was coupled with finite element methods (FEM) [42,43] and fractal finite element methods (FFEM) [44,45] using ramp function approach. EFG was also coupled with RPIM [46] which can also be categorized as a true meshless method in contrast to coupled FE-EFG approach. This class of hybrid methods acts like a two-edged sword in which the shape functions fulfills the Kronecker delta property along with the smoothness and higher order of continuity of EFGM shape functions.

EFGM [12] is a type of meshless method widely used for analysis of fracture problems[47–51]. EFGM scores over other meshless methods of fracture analysis by eliminating the need of remeshing and redistribution of nodal arrangements. EFGM also provides higher rates of convergence, higher adaptivity and can handle large material distortions easily[52]. EFGM formulation generates symmetric matrices and simpler forms of final integrand when compared to MLPG and Diffuse Element Method[53], also in comparison to partition of unity (PU) based methods like XFEM, EFG is computationally efficient[54].

1.1.1 Classification Of Meshless Methods

The difference in FEM procedure can be easily depicted by the flow diagram (Fig. 1.1), which shows the basic procedure applied for solving any problem using meshfree methods. There are a number of versions of meshfree methods developed so far and since this is in development stage, some new ones will continue to appear in the future. According to the approaches to arrive at the discrete governing equations, they largely fall into three categories. The first category is the meshfree methods based on strong-form formulation, second is based on weak-form formulation and the last one is mixed of both i.e. based on strong-weak form formulation as shown in Fig.1.2. They can also be classified in terms of approximation schemes used during the formulation as shown in Fig.1.3.

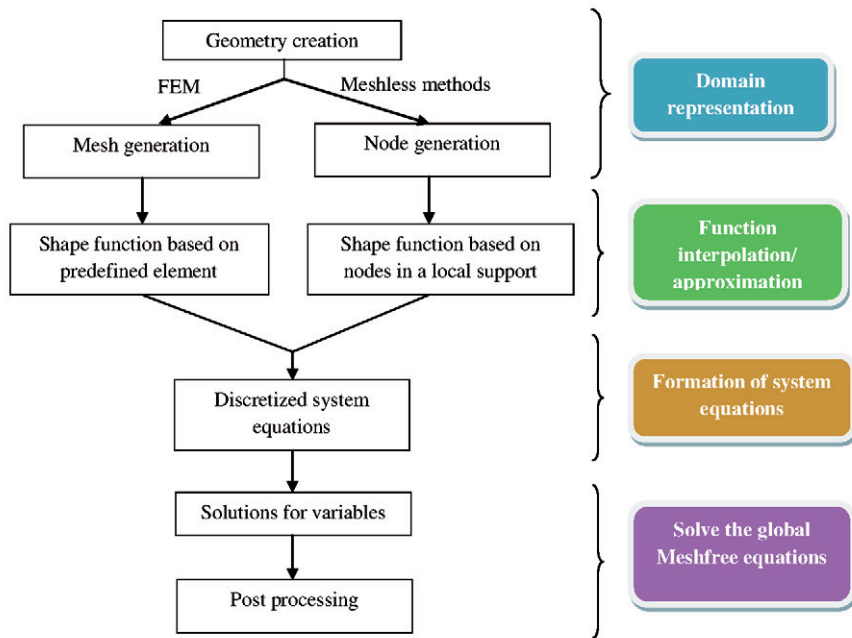


Fig 1.1: Meshfree procedure

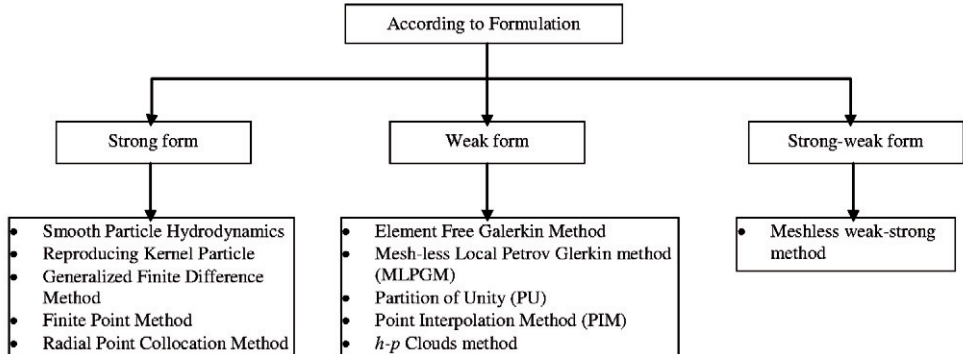


Fig 1.2: Classifications according to formulation

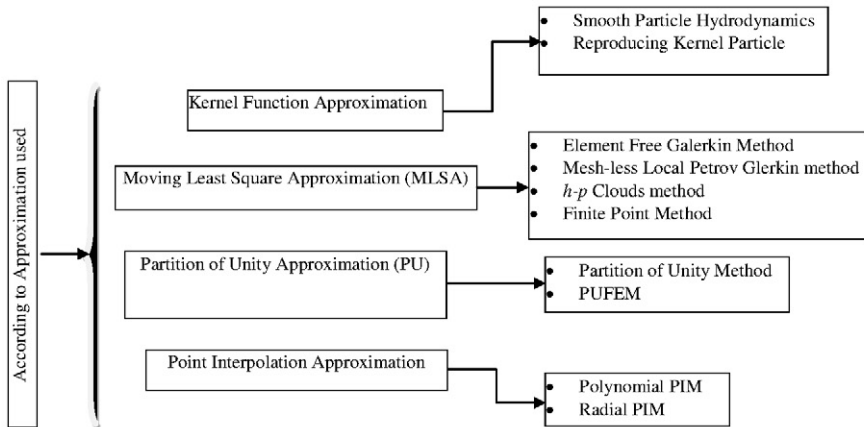


Fig. 1.3: Classifications according to approximation

1.2 Element Free Galerkin Method (EFGM)

EFGM has been considered a meshfree method because it requires only a set of nodes over the given domain along with boundary description to construct the approximation function. Hence, there is no need of element and element connectivity data like finite element method. In this method, both trial and test functions are constructed from the same space using MLS approximants.

1.2.1 Basic Approximations

Using the Lagrangian co-ordinates, we can write the meshless approximation for a scalar function u as

$$u(x,t) = \sum_{l \in S} \phi_l(x) u_l(t) \quad (1.1)$$

where $\phi_I: \Omega \rightarrow R$ are shape functions and u_I 's are the nodal values at particle I located at position x_I and S is the set of nodes I for which $\phi_I(x) \neq 0$. It should be observed that the above form is similar to FEM approximation. The difference lies in the fact that the shape functions in Eq.(1.1) are only approximations not interpolants, as $u_I \neq u(x_I)$. Henceforth special procedures are to be followed for treatment of essential boundary conditions.

1.2.2 Kernel (Weight) Function

The shape functions ϕ_I are extracted from kernel functions, commonly called as window or weighting functions, which are denoted by $w_I : \Omega \rightarrow R$. The kernel weight functions have compact support. The size of the support domain is defined by a dimensionless parameter called as dilatation parameter or smoothening length. This parameter plays a vital role in shaping accuracy and stability of analysis. Further characteristics of weight function will be discussed in subsequent section.

1.2.3 Completeness

If there is a notion of consistency in finite difference methods the Galerkin methods have the same concept called as completeness. Completeness can be called as reproducibility or the ability of an approximation to regenerate a polynomial of a certain order. A zero order complete approximation is the one which can reproduce constant functions exactly. If linear functions can be reproduced exactly it can be judged as linear(first order) complete, and so on for higher orders of completeness.

1.2.4 Partition Of Unity

A partition of unity (PU) [52] is an archetype where a domain is bifurcated into overlapping subdomains Ω_I , each one of which is related to a function $\phi_I(x)$ which is non-zero only in Ω_I and is defined by the following property

$$\sum_{I=1}^N \phi_I(x) = 1 \text{ in } \Omega \quad (1.2)$$

From Eq. (1.1). we can infer that there are basically two ways to increase the order of completeness of that approximation. To achieve this, the first method is to increase the completeness of the shape function intrinsically, i.e. by increasing the order of completeness of the shape functions directly. Alternatively, the order of completeness may be increased by modifying Eq. (1.1) using the partition of unity (PU) concept. In this case, a low-order approximation space (low-order shape functions Φ_I) is enriched with additional functions, which increases the order of completeness.

CHAPTER 2

CONSTRUCTION OF SHAPE FUNCTIONS

2.1 Methods For Construction Of Shape Functions

Shape functions in finite element approximations or meshfree approximations interpolate the solution between the discrete values obtained at the mesh nodes. The methods used for the construction of shape function influences the whole analysis as it will also be further used for enforcement of Dirichlet boundary conditions as well. Hence, the method for shape function construction should be carefully selected. In the analysis of fracture problems using EFGM, moving least square approximation is most widely used but it lacks Kronecker delta property, hence modifications in MLS approach and other methods to obtain shape functions were developed which will be discussed in following sections.

2.1.1 Moving Least Square (MLS) Approximation

The MLS approximant requires only a set of nodes for its construction [22] and is made up of three components: a compact support weight function associated with each node, a polynomial basis function and a set of coefficients that depends on node position. The support of the weight function defines the nodal domain of influence, over which a particular node contributes to the approximation. The overlap of the node's domain of influence defines the nodal connectivity.

In EFGM, the field variable u is approximated by MLS approximation, $u^h(\mathbf{x})$ from Belytschko et al. [12] which is given by

$$u^h(\mathbf{x}) = \sum_{j=1}^m p_j(\mathbf{x}) a_j(\mathbf{x}) \equiv \mathbf{p}^T(\mathbf{x}) \mathbf{a}(\mathbf{x}) \quad (2.1)$$

where, $\mathbf{p}(\mathbf{x})$ is a vector of complete basis functions (usually polynomial) is given as: $\mathbf{p}^T(\mathbf{x}) = [1, x, y, z, xy, yz, zx, \dots x^k, y^k, z^k]$ (2.2)

and $\mathbf{a}(\mathbf{x})$ is a vector of unknown coefficients

$$\mathbf{a}^T(\mathbf{x}) = [a_1(\mathbf{x}), a_2(\mathbf{x}), a_3(\mathbf{x}), \dots a_m(\mathbf{x})] \quad (2.3)$$

where, $\mathbf{x}^T = [x \ y \ z]$, k' is the degree of the polynomial and m is the number of terms in the basis. Some complete polynomial basis functions and corresponding coefficient vectors are given as

1-D: Linear basis

$$\mathbf{p}^T(\mathbf{x}) = [1, x], \quad (m = 2, \text{ linear}) \quad (2.4)$$

$$\mathbf{a}^T(\mathbf{x}) = [a_1(x), a_2(x)] \quad (2.5)$$

Quadratic basis

$$\mathbf{p}^T(\mathbf{x}) = [1, x, x^2], \quad (m = 3, \text{ quadratic}) \quad (2.6)$$

$$\mathbf{a}^T(\mathbf{x}) = [a_1(x), a_2(x), a_3(x)] \quad (2.7)$$

2-D: Linear basis

$$\mathbf{p}^T(\mathbf{x}) = [1, x, y] \quad (m = 3, \text{ linear}) \quad (2.8)$$

$$\mathbf{a}^T(\mathbf{x}) = [a_1(\mathbf{x}), a_2(\mathbf{x}), a_3(\mathbf{x})] \quad (2.9)$$

Quadratic basis

$$\mathbf{p}^T(\mathbf{x}) = [1, x, y, xy, x^2, y^2], \quad (m = 6, \text{ quadratic}) \quad (2.10)$$

$$\mathbf{a}^T(\mathbf{x}) = [a_1(\mathbf{x}), a_2(\mathbf{x}), a_3(\mathbf{x}), a_4(\mathbf{x}), a_5(\mathbf{x}), a_6(\mathbf{x})] \quad (2.11)$$

3-D: Linear basis

$$\mathbf{p}^T(\mathbf{x}) = [1 \ x \ y \ z] \quad (m = 4, \text{ linear}) \quad (2.12)$$

$$\mathbf{a}^T(\mathbf{x}) = [a_1(\mathbf{x}), a_2(\mathbf{x}), a_3(\mathbf{x}), a_4(\mathbf{x})] \quad (2.13)$$

Quadratic basis

$$\mathbf{p}^T(\mathbf{x}) = [1, x, y, z, xy, yz, zx, x^2, y^2, z^2] \quad (m = 10, \text{ quadratic}) \quad (2.14)$$

$$\mathbf{a}^T(\mathbf{x}) = [a_1(\mathbf{x}), a_2(\mathbf{x}), a_3(\mathbf{x}), a_4(\mathbf{x}), a_5(\mathbf{x}), a_6(\mathbf{x}), a_7(\mathbf{x}), a_8(\mathbf{x}), a_9(\mathbf{x}), a_{10}(\mathbf{x})] \quad (2.15)$$

The unknown coefficients $\mathbf{a}(\mathbf{x})$ are obtained by minimizing a weighted least square sum of the difference between local approximation, $u^h(\mathbf{x})$ and field function nodal parameters u_I . The weighted least square sum denoted by $L(\mathbf{x})$ can be written in following quadratic form:

$$L(\mathbf{x}) = \sum_{I=1}^n w(\mathbf{x} - \mathbf{x}_I) [\mathbf{p}^T(\mathbf{x})\mathbf{a}(\mathbf{x}) - u_I]^2 \quad (2.16)$$

where, u_I is the nodal parameter associated with node I at $\mathbf{x} = \mathbf{x}_I$ but these are not the nodal values of $u^h(\mathbf{x} = \mathbf{x}_I)$ because $u^h(\mathbf{x})$ as an approximant not an interpolant (the difference between u_I and $u^h(\mathbf{x} = \mathbf{x}_I)$ is shown in Fig.2.1), $w(\mathbf{x} - \mathbf{x}_I)$ is the weight function having compact support associated with node I , and n is the number of nodes with domain of influence containing the point \mathbf{x} , i.e. $w(\mathbf{x} - \mathbf{x}_I) \neq 0$ as shown in Fig. 2.2

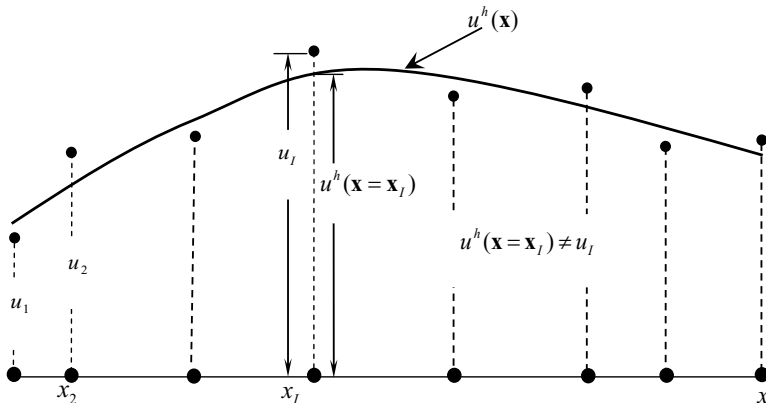


Fig. 2.1: Difference between u_I and $u^h(\mathbf{x})$

By setting $\frac{\partial L}{\partial \mathbf{a}} = 0$, the following set of linear equations is obtained

$$\mathbf{A}(\mathbf{x})\mathbf{a}(\mathbf{x}) = \mathbf{B}(\mathbf{x})\mathbf{u} \quad (2.17)$$

Or

$$\mathbf{a}(\mathbf{x}) = \mathbf{A}^{-1}(\mathbf{x})\mathbf{B}(\mathbf{x})\mathbf{u} \quad (2.18)$$

Where, $\mathbf{A}(\mathbf{x})$ and $\mathbf{B}(\mathbf{x})$ are given as:

In 1-D

$$\mathbf{A}(\mathbf{x}) = \sum_{I=1}^n w(x - x_I) \mathbf{p}(x_I) \mathbf{p}^T(x_I) = w(x - x_1) \begin{bmatrix} 1 & x_1 \\ x_1 & x_1^2 \end{bmatrix} + \dots + w(x - x_n) \begin{bmatrix} 1 & x_n \\ x_n & x_n^2 \end{bmatrix} \quad (2.19)$$

$$\mathbf{B}(\mathbf{x}) = [w(x - x_1)\mathbf{p}(x_1), \dots, w(x - x_n)\mathbf{p}(x_n)] = \left\{ w(x - x_1) \begin{bmatrix} 1 \\ x_1 \end{bmatrix}, \dots, w(x - x_n) \begin{bmatrix} 1 \\ x_n \end{bmatrix} \right\} \quad (2.20)$$

In 2-D

$$\begin{aligned} \mathbf{A}(\mathbf{x}) &= \sum_{I=1}^n w(\mathbf{x} - \mathbf{x}_I) \mathbf{p}(\mathbf{x}_I) \mathbf{p}^T(\mathbf{x}_I) \\ &= w(\mathbf{x} - \mathbf{x}_1) \begin{bmatrix} 1 & x_1 & y_1 \\ x_1 & x_1^2 & x_1 y_1 \\ y_1 & x_1 y_1 & y_1^2 \end{bmatrix} + w(\mathbf{x} - \mathbf{x}_2) \begin{bmatrix} 1 & x_2 & y_2 \\ x_2 & x_2^2 & x_2 y_2 \\ y_2 & x_2 y_2 & y_2^2 \end{bmatrix} + \dots \\ &\quad + w(\mathbf{x} - \mathbf{x}_n) \begin{bmatrix} 1 & x_n & y_n \\ x_n & x_n^2 & x_n y_n \\ y_n & x_n y_n & y_n^2 \end{bmatrix} \end{aligned} \quad (2.21)$$

$$\begin{aligned} \mathbf{B}(\mathbf{x}) &= \{w(\mathbf{x} - \mathbf{x}_1)\mathbf{p}(\mathbf{x}_1), w(\mathbf{x} - \mathbf{x}_2)\mathbf{p}(\mathbf{x}_2), \dots, w(\mathbf{x} - \mathbf{x}_n)\mathbf{p}(\mathbf{x}_n)\} \\ &= \left\{ w(\mathbf{x} - \mathbf{x}_1) \begin{bmatrix} 1 \\ x_1 \\ y_1 \end{bmatrix}, w(\mathbf{x} - \mathbf{x}_2) \begin{bmatrix} 1 \\ x_2 \\ y_2 \end{bmatrix}, \dots, w(\mathbf{x} - \mathbf{x}_n) \begin{bmatrix} 1 \\ x_n \\ y_n \end{bmatrix} \right\} \end{aligned} \quad (2.22)$$

In 3-D

$$\mathbf{A}(\mathbf{x}) = \sum_{I=1}^n w(\mathbf{x} - \mathbf{x}_I) \mathbf{p}(\mathbf{x}_I) \mathbf{p}^T(\mathbf{x}_I)$$

$$= w(\mathbf{x} - \mathbf{x}_1) \begin{bmatrix} 1 & x_1 & y_1 & z_1 \\ x_1 & x_1^2 & x_1 y_1 & x_1 z_1 \\ y_1 & x_1 y_1 & y_1^2 & y_1 z_1 \\ z_1 & x_1 z_1 & y_1 z_1 & z_1^2 \end{bmatrix} + w(\mathbf{x} - \mathbf{x}_2) \begin{bmatrix} 1 & x_2 & y_2 & z_2 \\ x_2 & x_2^2 & x_2 y_2 & x_2 z_2 \\ y_2 & x_2 y_2 & y_2^2 & y_2 z_2 \\ z_2 & x_2 z_2 & y_2 z_2 & z_2^2 \end{bmatrix} + \dots \\ + w(\mathbf{x} - \mathbf{x}_n) \begin{bmatrix} 1 & x_n & y_n & z_n \\ x_n & x_n^2 & x_n y_n & x_n z_n \\ y_n & x_n y_n & y_n^2 & y_n z_n \\ z_n & x_n z_n & y_n z_n & z_n^2 \end{bmatrix} \quad (2.23)$$

$$\mathbf{B}(\mathbf{x}) = \{w(\mathbf{x} - \mathbf{x}_1)\mathbf{p}(\mathbf{x}_1), w(\mathbf{x} - \mathbf{x}_2)\mathbf{p}(\mathbf{x}_2), \dots, w(\mathbf{x} - \mathbf{x}_n)\mathbf{p}(\mathbf{x}_n)\} \quad (2.24)$$

By substituting Eq. (2.6) in Eq. (2.1), the MLS approximation is obtained as:

$$u^h(\mathbf{x}) = \sum_{I=1}^n \Phi_I(\mathbf{x}) u_I = \Phi^T(\mathbf{x}) \mathbf{u} \quad (2.25)$$

Where,

$$\Phi^T(\mathbf{x}) = \{\Phi_1(\mathbf{x}), \Phi_2(\mathbf{x}), \Phi_3(\mathbf{x}), \dots, \Phi_n(\mathbf{x})\} \quad (2.26)$$

$$\mathbf{u}^T = [u_1, u_2, u_3, \dots, u_n] \quad (2.27)$$

The mesh free shape function $\Phi_I(\mathbf{x})$ is defined as:

$$\Phi_I(\mathbf{x}) = \sum_{j=1}^m p_j(\mathbf{x}) (\mathbf{A}^{-1}(\mathbf{x}) \mathbf{B}(\mathbf{x}))_{jl} = \mathbf{p}^T \mathbf{A}^{-1} \mathbf{B}_I \quad (2.28)$$

The linear consistency requirements for the shape function $\Phi_I(\mathbf{x})$ from [53] are given as:

$$\sum_{I=1}^n \Phi_I(\mathbf{x}) = 1 \quad (2.29a)$$

$$\sum_{I=1}^n \Phi_I(\mathbf{x}) x_I = x \quad (2.29b)$$

$$\sum_{I=1}^n \Phi_I(\mathbf{x}) y_I = y \quad (2.29c)$$

$$\sum_{I=1}^n \Phi_I(\mathbf{x}) z_I = z \quad (2.29d)$$

The derivatives of MLS shape function are computed as:

$$\Phi_{I,x}(\mathbf{x}) = (\mathbf{p}^T \mathbf{A}^{-1} \mathbf{B}_I)_{,x} = \mathbf{p}_{,x}^T \mathbf{A}^{-1} \mathbf{B}_I + \mathbf{p}^T (\mathbf{A}^{-1})_{,x} \mathbf{B}_I + \mathbf{p}^T \mathbf{A}^{-1} \mathbf{B}_{I,x} \quad (2.30)$$

where,

$$\mathbf{B}_{I,x}(\mathbf{x}) = \frac{dw}{d\mathbf{x}}(\mathbf{x} - \mathbf{x}_I) \mathbf{p}(\mathbf{x}_I) \quad (2.31)$$

and $\mathbf{A}^{-1,x}$ is computed by

$$\mathbf{A}^{-1,x} = -\mathbf{A}^{-1} \mathbf{A}_{,x} \mathbf{A}^{-1} \quad (2.32)$$

where,

$$\mathbf{A}_{,x} = \sum_{I=1}^n \frac{dw}{d\mathbf{x}}(\mathbf{x} - \mathbf{x}_I) \mathbf{p}(\mathbf{x}_I) \mathbf{p}^T(\mathbf{x}_I) \quad (2.33)$$

2.1.1.1 Efficient Shape Function Calculation

To compute the meshfree shape functions Φ_I , it is necessary to calculate \mathbf{A}^{-1} . In 1-D problems, this operation of inverting the matrix is not very difficult but in 2-D and 3-D problems, this exercise becomes very much burdensome and expensive from the computational point of view. To overcome this situation, Dolbow and Belytschko [55] proposed a computationally inexpensive alternative approach. This approach involves the LU decomposition [56] of the \mathbf{A} matrix. The shape function is given as:

$$\Phi_I(\mathbf{x}) = \mathbf{p}^T(\mathbf{x}) \mathbf{A}^{-1}(\mathbf{x}) \mathbf{B}_I(\mathbf{x}) = \gamma^T(\mathbf{x}) \mathbf{B}_I(\mathbf{x}) \quad (2.34)$$

Where,

$$\gamma^T(\mathbf{x}) = \mathbf{p}^T(\mathbf{x}) \mathbf{A}^{-1}(\mathbf{x}). \quad (2.35)$$

This leads to the relationship

$$\mathbf{A}(\mathbf{x}) \gamma(\mathbf{x}) = \mathbf{p}(\mathbf{x}) \quad (2.36)$$

The vector $\gamma(\mathbf{x})$ is to be calculated using LU decomposition of the matrix \mathbf{A} followed by back substitution.

The partial derivatives of $\gamma(\mathbf{x})$ can be recursively calculated as:

$$\mathbf{A}(\mathbf{x})\gamma_{,x}(\mathbf{x}) = \mathbf{p}_{,x}(\mathbf{x}) - \mathbf{A}_{,x}(\mathbf{x})\gamma(\mathbf{x}) \quad (2.37)$$

$$\mathbf{A}(\mathbf{x})\gamma_{,y}(\mathbf{x}) = \mathbf{p}_{,y}(\mathbf{x}) - \mathbf{A}_{,y}(\mathbf{x})\gamma(\mathbf{x}) \quad (2.38)$$

$$\mathbf{A}(\mathbf{x})\gamma_{,z}(\mathbf{x}) = \mathbf{p}_{,z}(\mathbf{x}) - \mathbf{A}_{,z}(\mathbf{x})\gamma(\mathbf{x}) \quad (2.39)$$

The derivatives of shape function are given as:

$$\Phi_{I,x}(\mathbf{x}) = \gamma^T_{,x}(\mathbf{x})\mathbf{B}_I(\mathbf{x}) + \gamma^T(\mathbf{x})\mathbf{B}_{I,x}(\mathbf{x}) \quad (2.40)$$

$$\Phi_{I,y}(\mathbf{x}) = \gamma^T_{,y}(\mathbf{x})\mathbf{B}_I(\mathbf{x}) + \gamma^T(\mathbf{x})\mathbf{B}_{I,y}(\mathbf{x}) \quad (2.41)$$

$$\Phi_{I,z}(\mathbf{x}) = \gamma^T_{,z}(\mathbf{x})\mathbf{B}_I(\mathbf{x}) + \gamma^T(\mathbf{x})\mathbf{B}_{I,z}(\mathbf{x}) \quad (2.42)$$

2.1.1.2 Orthogonal Basis Functions For MLS Interpolant

To avoid the inversion of moment matrix at every quadrature point diagonalizing of matrix $A(x)$ can be done. To perform this operation on the matrix $A(x)$ from Eqs. (2.17-2.18) for arbitrary x , the condition of orthogonality which is imposed at any point x where $a(x)$ is to be computed is given by

$$\sum_I^n w(x - x_I)q_k(x_I)q_i(x_I) = 0, \quad k \neq i. \quad (2.43)$$

To obtain the orthogonal basis functions $q(x)$, it is necessary to distinguish the point at which we are evaluating $u(x)$ from the dependence of the polynomial on x . Let the point at which we are evaluating $a(x)$ be denoted by \bar{x} , and assume that the spatial variable be denoted by x . Then the MLS interpolant can be written as

$$u^h(x) = \sum_j^m q_j(x, \bar{x})a_j(\bar{x}) \equiv q^t(x, \bar{x})a(\bar{x}) \quad (2.44)$$

where the basis functions $q_j(x, \bar{x})$ are constructed so that the following orthogonality condition is satisfied

$$\sum_I^n w(x_I - \bar{x})q_k(x_I, \bar{x})q_j(x, \bar{x}) = 0, \quad k \neq j. \quad (2.45)$$

For the given arbitrary basis functions $p_k(x)$ ($k = 1, \dots, m$), the orthogonal basis functions $q_k(x, \bar{x})$ can be obtained by using Schmidt-orthogonalization method

$$q_k(x, \bar{x}) = p_k(x) - \sum_j^{k-1} \alpha_{kj}(\bar{x})q_j(x, \bar{x}), \quad k = 1, \dots, m \quad (2.46)$$

where

$$\alpha_{kj}(\bar{x}) = \frac{\sum_I^n w_I(\bar{x}) p_k(x_I) q_j(x_I, \bar{x})}{\sum_I^n w_I(\bar{x}) q_j^2(x_I, \bar{x})} \quad (2.47)$$

Using Eq. (4) the orthogonal basis functions $q_j(x, \bar{x})$ in one dimension can be given in special form

$$q_1(x, \bar{x}) = 1 \quad (2.48)$$

$$q_2(x, \bar{x}) = x - \beta_1(\bar{x}) \quad (2.49)$$

$$q_{j+2}(x, \bar{x}) = (x - \beta_{j+1}(\bar{x})) q_{j+1}(x, \bar{x}) - \gamma_j(\bar{x}) q_j(x, \bar{x}), \quad j = 1, \dots, m-2 \quad (2.50)$$

where

$$\beta_{j+1}(\bar{x}) = \frac{\sum_I^n w_I(\bar{x}) x_I q_{j+1}^2(x_I, \bar{x})}{\sum_I^n w_I(\bar{x}) q_{j+1}^2(x_I, \bar{x})}, \quad j = 0, \dots, m-2 \quad (2.51)$$

$$\gamma_j(\bar{x}) = \frac{\sum_I^n w_I(\bar{x}) q_{j+1}^2(x_I, \bar{x})}{\sum_I^n w_I(\bar{x}) q_j^2(x_I, \bar{x})}, \quad j = 1, \dots, m-2 \quad (2.52)$$

Now it can be inferred that the matrix A has become diagonal due to the orthogonality condition stated above and its coefficients $a_j(\bar{x})$ can be directly obtained from Eq. (2.17)

$$a_j(\bar{x}) = \frac{\sum_I^n w_I(\bar{x}) q_j(x_I, \bar{x}) u_I}{b_j(\bar{x})}, \quad j = 1, \dots, m, \quad (2.53a)$$

and

$$b_j(\bar{x}) = \sum_I^n w_I(\bar{x}) q_j^2(x_I, \bar{x}) \quad (2.53b)$$

The distinction between x and \bar{x} is only needed in the least square minimization. Once this is completed, the coefficients are determined at a point x , the distinction between x and \bar{x} is no longer necessary, so we can replace the variable \bar{x} by x in Eq. (2.44) and Eq. (2.53). Thus, the MLS interpolant can be written as follows:

$$u^h(x) = \sum_I^n \phi_I(x) u_I, \quad (2.54)$$

Now the shape function $\phi_I(x)$ can be written as

$$\phi_I(x) = w_I(x) \sum_j^m C_{jI}(x), \quad (2.55a)$$

$$C_{jl}(x) = \frac{q_j(x,x)q_j(x_l,x)}{b_j(x)} \quad (2.55b)$$

The partial derivatives of $\phi_l(x)$ can be calculated as follows

$$\phi_{l,k}(x) = w_{l,k}(x) \sum_j^m C_{jl}(x) + w_l(x) \sum_j^m C_{j,l,k}(x) \quad (2.56)$$

where

$$C_{j,l,k}(x) = [q_{j,k}(x,x)q_j(x_l,x) + q_j(x,x)q_{j,k}(x_l,x) - b_{j,k}(x)C_{jl}(x)]/b_j(x) \quad (2.57a)$$

$$b_{j,k}(x) = \sum_j^n [w_{j,k}(x)q_j^2(x_l,x) + 2w_j(x)q_j(x_l,x)q_{j,k}(x_l,x)] \quad (2.57b)$$

The advantage of using orthogonal basis functions is that it not only reduces the computational cost but also improves the accuracy of interpolates when the condition number of matrix A is very small. It should be noted that Eq. (2.55) and Eq. (2.57) also, hold for three-dimensional problems.

2.1.1.3 Weight Function

The choice of weight function $w(\mathbf{x} - \mathbf{x}_l)$ affects the resulting approximation $u^h(\mathbf{x}_l)$ in EFG method. Therefore, the selection of appropriate weight function is essential in these methods. The weight function is non-zero only over a small neighborhood of a node \mathbf{x}_l , called the support or domain of influence of node l . The smoothness and continuity of the shape function $\Phi_l(\mathbf{x})$ depends on the smoothness and continuity of the weight function $w(\mathbf{x} - \mathbf{x}_l)$. If weight function is C^1 continuous then shape function will also have C^1 continuity (This property is represented in Fig.2.3).

A weight function must satisfy the following conditions from [54,57]

- It must be positive, continuous and differentiable in the domain of influence.
- It should decrease in magnitude as the distance from x to x_l increases so that local character of MLS approximation can be maintained.
- It should be zero outside the domain of influence.
- It should have a relatively larger value for a node, which is closer to the evaluation point than those of far nodes.

- The nodes in the domain of influence should not be collinear (except 1-D) and the number of nodes must be larger than the number of terms in the basis function ($n > m$).

The different weight functions used in fracture analysis are written as a function of normalized radius \bar{r} as:

The cubic spline (C.S.) weight function

$$w(\mathbf{x} - \mathbf{x}_I) = w(\bar{r}) = \begin{cases} \frac{2}{3} - 4\bar{r}^2 + 4\bar{r}^3 & \bar{r} \leq \frac{1}{2} \\ \frac{4}{3} - 4\bar{r} + 4\bar{r}^2 - \frac{4}{3}\bar{r}^3 & \frac{1}{2} < \bar{r} \leq 1 \\ 0 & \bar{r} > 1 \end{cases} \quad (2.58a)$$

The quadratic spline (Q.S.) weight function

$$w(\mathbf{x} - \mathbf{x}_I) = w(\bar{r}) = \begin{cases} 1 - 6\bar{r}^2 + 8\bar{r}^3 - 3\bar{r}^4 & 0 \leq \bar{r} \leq 1 \\ 0 & \bar{r} > 1 \end{cases} \quad (2.58b)$$

$$\text{where, } (\bar{r}) = \frac{\|\mathbf{x} - \mathbf{x}_I\|}{d_{mI}}$$

$\|\mathbf{x} - \mathbf{x}_I\|$ is the distance from a sampling point \mathbf{x} to a node \mathbf{x}_I and d_{mI} is the domain of influence of node I .

In 3-D

$$(\bar{r}_x) = \frac{\|\mathbf{x} - \mathbf{x}_I\|}{d_{mxI}} \quad (2.59a)$$

$$(\bar{r}_y) = \frac{\|\mathbf{x} - \mathbf{x}_I\|}{d_{myI}} \quad (2.59b)$$

$$(\bar{r}_z) = \frac{\|\mathbf{x} - \mathbf{x}_I\|}{d_{mzI}} \quad (2.59c)$$

and

$$d_{mxI} = d_{\max} c_{xI} \quad (2.60a)$$

$$d_{myI} = d_{\max} c_{yI} \quad (2.60b)$$

$$d_{mzI} = d_{\max} c_{zI} \quad (2.60c)$$

d_{\max} = scaling parameter which defines the size of the domain of influence and c_{xI} , c_{yI} and c_{zI} at node I are the distances to the nearest neighbors. d_{mxI} , d_{myI} and d_{mzI} are chosen such that the matrix is non-singular at every point in the domain. Properly choosing the domain of influence or nodal support is an important aspect of meshless methods. The size of the support should be sufficiently large so that the stiffness matrix is regular and well-conditioned. But too large domains of influence lead to a great deal of computational expense in forming the approximations as well as assembling the stiffness matrix. The domain of influence multiplier d_{\max} is typically 1.5-3 for static analysis and 2-2.5 for dynamic analysis.

The weight function at any given point is obtained as:

$$w(\mathbf{x} - \mathbf{x}_I) = w(\bar{r}_x) w(\bar{r}_y) w(\bar{r}_z) = w_x w_y w_z \quad (2.61)$$

where, $w(\bar{r}_x)$, $w(\bar{r}_y)$ and $w(\bar{r}_z)$ can be calculated by replacing \bar{r} by \bar{r}_x , \bar{r}_y and \bar{r}_z in the expression of $w(\bar{r})$.

The derivatives of the weight functions are calculated as:

$$w_{,x} = \frac{dw_x}{dx} w_y w_z \quad (2.62a)$$

$$w_{,y} = \frac{dw_y}{dy} w_x w_z \quad (2.62b)$$

$$w_{,z} = \frac{dw_z}{dz} w_x w_y \quad (2.62c)$$

Another method called the improved element free Galerkin (IEFG) method was proposed [58] to remove the singularities associated with the weight functions in which the basis function is obtained by normalizing the function $p_j(x)$. As there are fewer coefficients in the IEFG approximation than the standard EFG method fewer nodes need to be selected in the entire domain. So, these can be an increase in computation speed in IEFG [24]. For two-dimensional fracture problems, the IEFG

method can be modified by using enriched basis function which has a better potential in capturing the stress field oscillations around the crack tip [24].

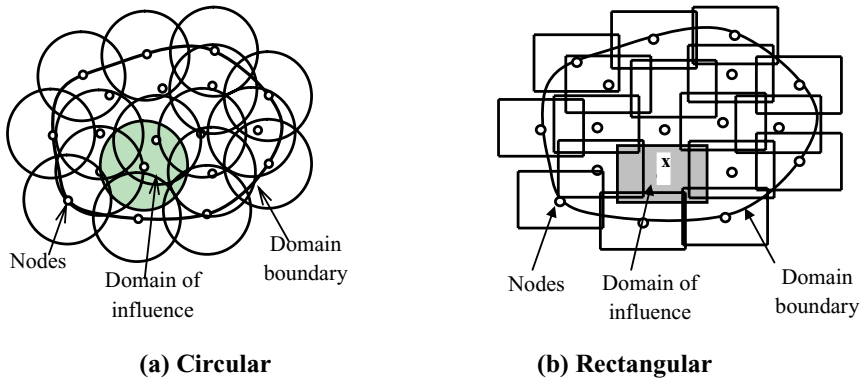


Fig. 2.2 A computational model for Meshless method showing the boundary, nodes and domain of influence

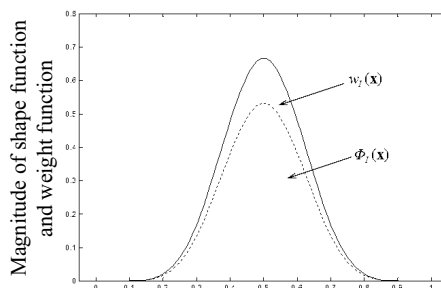


Fig. 2.3: A plot of weight function and corresponding shape function

2.1.1.3.1 Modifications In Weight Function

An important component of EFGM or other meshless methods is the weight function and selection of appropriate weight function has a huge impact on the accuracy of the analysis. The weight function further helps in calculation of shape functions. In most of the works on fracture mechanics by EFGM weight functions defined by Eq.(2.58) are used, but a few modifications were made by selection of

new kind of weight functions and modifying original weight functions to improve their capability.

2.1.1.3.1.1 Weight Function Based On Student's-t-Distribution

This formulation was first used in their works by [59]

$$w(x - x_I) = \begin{cases} \frac{\left(1 + \beta^2 \left(\frac{d_I^2}{d_{ml}^2}\right)\right)^{-\frac{1+\beta}{2}}}{1 - (1 + \beta^2)^{-\frac{1+\beta}{2}}}, & d_I \leq d_{ml} \\ 0, & d_I > d_{ml} \end{cases} \quad (2.63)$$

where β is the parameter controlling the shape of the weight function, $d_I = \|x - x_I\|$ is the distance from a sampling point x to a node x_I , d_{ml} is the domain of influence of node I such that

$$d_{ml} = d_{max} c_I \quad (2.64)$$

In which c_I is a characteristic nodal spacing distance which is chosen such that the node I have enough number of neighbors sufficient for regularity of $A(x)$ in Eq.(2.19) (which is used to determine the MLS approximation), and d_{max} is a scaling parameter. It is to be noted that the t-distribution used in Eq.(2.63) stands for the probability density function of a standard Gaussian random variable divided by the square root of a χ^2 random variable with β degrees of freedom.

To avoid any discontinuities in the shape functions due to the presence of cracks, a diffraction method [60] can be used to modify d_I in the weight function. According to this method, when the line joining the node x_I to the sampling point x intersects the crack segment and the crack tip within the domain of influence of the node x_I , d_I is modified as [40]

$$d_I = \left(\frac{(s_1 + s_2(x))^\lambda}{s_0(x)} \right) s_0(x) \quad (2.65)$$

where

$s_1 = \|x_I - x_c\|$, $s_2(x) = \|x - x_c\|$, $s_0(x) = \|x - x_I\|$, x and x_c are the coordinates of sampling point and crack tip, and $1 \leq \lambda \geq 2$ is a parameter for

adjusting the distance of the support on the opposite side of the crack. This method is explained in further sections.

2.1.1.3.1.2 Enriched Weight Function (EWF)

There exists a well-defined relationship between meshfree shape functions and their corresponding weight functions [61,62] which promote the intrinsic enrichment of kernel-based methods competently. Duflot and Nguyen-Dang utilized this relationship brought up the concept of enriched weight functions (EWFs) into light such that they can introduce a projection or distribution of the near-tip field solution into the approximation. The nodes or particles allied with EWFs can be directly added to crack tip which was earlier comprised of typical weight function. Duflot and Nguyen-Dang [61] provided a criteria upon which they suggested the following EWFs

$$w_{c_2}(x) := \xi \sqrt{r} \cos\left(\frac{\theta}{2}\right) w_{d^{tip}}(z), \quad (2.66a)$$

$$w_{s_2}^{top}(x) := \xi \sqrt{r} \left(1 + \sin\left(\frac{\theta}{2}\right)\right) w_{d^{tip}}(z) \quad (2.66b)$$

$$w_{s_2}^{bottom}(x) := \xi \sqrt{r} \left(1 - \sin\left(\frac{\theta}{2}\right)\right) w_{d^{tip}}(z) \quad (2.66c)$$

whose associated particles are located at the same position x^{tip} . The subscripts c_2 and s_2 in Eqs. (2.66a-2.66c) are shortened for the terms $\cos(\theta/2)$ and $\sin(\theta/2)$, respectively. The superscripts top and bottom, respectively, represent the top and bottom regions of the crack faces which are covered by the associated weight functions. $w_{d^{tip}}(z)$ is a usual weight function (e.g. cubic spline, quadratic spline, Student-t-distribution) with the same definitions for all its parameters as detailed in earlier in Eqs.(2.58,2.63). d^{tip} can be considered identical for all EWFs and determined by Eqs. (2.60a-2.60c) for a particle at the crack-tip. The dimensionless factor ξ controls the amplitude of EWFs relative to the regular weight functions

2.1.1.4 Enriched Basis Function

To avoid the cumbersome analysis with a large number of nodes around the crack tip singular functions associated with elastostatic fracture are incorporated by using special procedures in EFGM, this further reduces cost and eliminates problems

related to complex geometries. It was found that the incorporation of the singular fields in a meshfree method is substantially simpler and more trouble-free than in FEM. Enrichment of a meshfree method may be carried out extrinsically or intrinsically and it will be discussed in subsequent chapters.

2.1.1.4.1 The Partition Of Unity Finite Element Method (PUFEM)

The approximation of (PUFEM) [52] is given by

$$u^h(x) = \sum_{l=1}^N \phi_l(x) \sum_{j=1}^N p_j(x) v_{jl} = \sum_{l=1}^N \phi_l(x) p^T(x) v_l \quad (2.67)$$

where $\phi(x)$ are called the shape functions based on Lagrange polynomials. The coefficients of v_{jl} are nodal unknowns. In this approximation, the number of terms x^k governs the completeness of the approximation which makes it an attractive method to be worked upon. Another added advantage of this approximation is that, special enhancement functions, near crack tip fields in case of fracture mechanics, can be easily integrated into the approximation through this extrinsic basis.

2.1.2 Radial Basis Function (RBF) For Construction Of Shape Function

[63] brought the multiquadric radial basis function into the picture for the first time and later on developments were made in it by Kansa for spatial approximations. To overcome the difficulties associated with the general structure of meshfree methods Wen and Aliabadi [31] introduced a meshfree Galerkin method based on enriched radial basis function. As it is well established that the radial basis functions are globally defined, the consequential matrix for interpolation is crowded and can become ill-conditioned, particularly for a large number of interpolation points. It also causes potent stability problems and is also computationally inept. A sub-domain Ω_y , as shown in Fig.2.4. is the neighborhood of a point field point y and is also called its support domain.

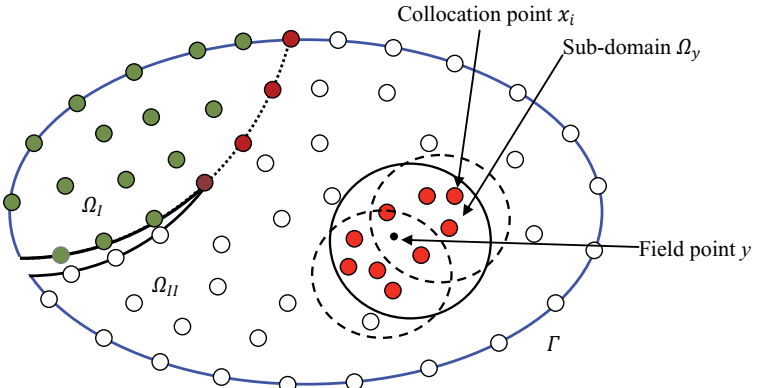


Fig.2.4 Sub-domain Ω_y for RBF interpolation of the field point y and support domains: \circ node in domain Ω_I ; \bullet node in domain Ω_{II} ; \blacksquare node on interface

The distribution of function u in the sub-domain Ω_y over a number of randomly distributed nodes $\{\mathbf{x}_i\}$, $i = 1, 2, \dots, n(y)$ can be interpolated at the point y by

$$u(y) = \sum_{i=1}^n R_i(y, x_i) a_i = R(y, x) a(y) \quad (2.68)$$

where $R(y, x) = \{R_1(y, x), R_2(y, x), \dots, R_n(y, x)\}$ is a set of radial basis functions centered at point y , $\{a_k\}_{k=1}^n$ are the unknown coefficients to be determined. The radial basis function can be assumed as [64]:

$$R_k(y, x_k) = \sqrt{c^2 + |y - x_k|^2} \quad (2.69)$$

where c is a free parameter. From the interpolation strategy in Eq. (2.69), a linear system for unknown coefficients a become

$$R_0 a = \hat{u} \quad (2.70)$$

where coefficient matrix

$$R_0 = \begin{bmatrix} R_1(x_1, x_1) & R_2(x_1, x_2) & \cdots & R_n(x_1, x_n) \\ R_1(x_2, x_1) & R_1(x_2, x_2) & \cdots & R_n(x_2, x_n) \\ \vdots & \vdots & \ddots & \vdots \\ R_1(x_n, x_1) & R_2(x_n, x_2) & \cdots & R_n(x_n, x_n) \end{bmatrix} \quad (2.71)$$

As the RBF are positive definite, the matrix R_θ is certain to be invertible. Therefore, we can obtain the vector of unknowns from Eq. (2.70)

$$a = R_0^{-1}(x)\hat{u}(x) \quad (2.72)$$

So that the approximation $u(y)$ can be represented, at domain point y , as

$$u(y) = R(y, x)R_0^{-1}(x)\hat{u}(x) = \bar{\Phi}(y, x)\hat{u} = \sum_{k=1}^n \phi_k \hat{u}_k \quad (2.73)$$

where the shape function is defined by

$$\bar{\Phi}(y, x) = R(y, x)R_0^{-1}(x) \quad (2.74)$$

The shape function possesses the Kronecker delta property and depends only on the distribution of speckled nodes within the support domain. The partial derivatives of shape function with respect to the field point can be easily evaluated as the inverse matrix of coefficient $R_0^{-1}(x)$ is a function of distributed node x_i in the support domain. From Eq. (2.73), the first derivative of displacement with respect to the domain field point y can be obtained directly

$$u(y) = \bar{\Phi}_{,k}(y, x)\hat{u} = \sum_{k=1}^n \phi_{i,k} \hat{u}_i, \quad k=1,2 \quad (2.75)$$

where

$$\bar{\Phi}(y, x) = R(y, x)R_0^{-1}(x) \quad (2.76)$$

Using Eq. (2.69) we have

$$R_{i,k} = \frac{y_k - x_k^i}{\sqrt{c^2 + |y - x_i|^2}} \quad (2.77)$$

To obtain the unique solution of the interpolation problem [65] a polynomial should be added to interpolation in Eq. (2.68) and can be written as:

$$u(y) = \sum_{k=1}^n R_k(y, x)a_k + \sum_{j=1}^t P_j(y)b_j = R_0(y, x)a + P(y)b \quad (2.78)$$

along with constraints

$$\sum_{j=1}^t P_k(x_j)a_j = 0, \quad 1 \leq k \leq t \quad (2.79)$$

where $\{P_k\}_{k=1}^t$ is the basis for P_{m-1} , the set of d-variate polynomials of the degree $\leq m - 1$ and

$$t = \binom{m+d-1}{d} \quad (2.80)$$

is the dimension of P_{m-1} . A set of linear equations can be written, in matrix form as

$$R_0 a + P^T b = \hat{u}, \quad Pa = 0 \quad (2.81)$$

$$P(x) = \begin{bmatrix} P_1(x_1) & P_2(x_1) & \dots & P_t(x_1) \\ P_1(x_2) & P_2(x_2) & \cdots & P_t(x_2) \\ \vdots & \vdots & \ddots & \vdots \\ P_1(x_n) & P_2(x_n) & \cdots & P_t(x_n) \end{bmatrix} \quad (2.82)$$

Solving Eq. (2.81) gives

$$b = (P^T R_0^{-1} P)^{-1} P^T R_0^{-1} \hat{u}, \quad (2.83)$$

$$a = R_0^{-1} [I - P(P^T R_0^{-1} P)^{-1} P^T R_0^{-1}] \hat{u} \quad (2.84)$$

where I denotes the diagonal unit matrix. It is obvious from above that the coefficients a and b are functions of nodal coordinate x in the support domain only.

2.2 Conclusion

This chapter provides an overview of the methods used to derive the shape functions to be used for EFGM. The following conclusions can be drawn:

- MLS approach is most widely used as it is most accurate but fails to provide Kronecker delta property which later on causes difficulty in enforcement of essential boundary conditions.
- Using orthogonal basis function for MLS approximation is slightly less accurate than conventional method although, it reduces engineering effort to invert the shape function matrix in every step. The numerical results have better convergence than FEM and BEM
- MLS has better accuracy than RBF but with proper selection of free parameters RBF can be more stable.

CHAPTER 3

ENFORCING BOUNDARY CONDITIONS IN EFGM

3.1 Enforcement Of Essential Boundary Conditions

The proper imposition of essential boundary condition is quite difficult in EFGM since MLS approximation does not satisfy the Kronecker delta function property i.e. $\Phi_i(x_j) \neq \delta_{ij}$. Many numerical techniques have been proposed to enforce the essential boundary conditions in EFGM. Lagrange multiplier method was first used by [12]. This technique is quite accurate, but its imposition loses the positive definite and bandedness properties of the system matrix. Further, Lagrange multiplier approach was modified using modified variational principle [23] where Lagrange multipliers were replaced by their physical meaning. Penalty method [14,27,66,67] was also used as it provides positive definite equations and also maintains the bandedness property. To minimize the computational time and engineering effort coupled approaches like coupling with finite element method and coupling with radial point interpolation method were proposed by Krongauz and Belytschko [42] and Cao et al [46] respectively for the imposition of essential boundary conditions. These approaches successfully entrapped the potentials of two methods consequently reducing error and computation time of analysis.

3.1.1 Lagrange Multiplier Method

We consider the two-dimensional (2D) problem with small displacements on the domain Ω bounded by Γ . The equilibrium equation is

$$\nabla \cdot \sigma + \mathbf{b} = 0 \quad \text{in } \Omega \quad (3.1)$$

Where, σ is the stress tensor, which corresponds to the displacement field u , b is a body force vector, $\nabla \cdot$ is the divergence operator. The boundary conditions are given as follows

$$(\text{natural b.c.}) \quad \sigma \cdot \mathbf{n} = \bar{\mathbf{t}} \quad \text{on } \Gamma_t \quad (3.2)$$

$$(\text{essential b.c.}) \quad \mathbf{u} = \bar{\mathbf{u}} \quad \text{on } \Gamma_u \quad (3.3)$$

in which the superposed bar denotes prescribed boundary values, and \mathbf{n} is the unit normal to the domain Ω .

The variational (or weak) form of the equilibrium Eq. (3.1) can be obtained as follows.

$$\int_{\Omega} \delta \boldsymbol{\varepsilon} : \boldsymbol{\sigma} d\Omega - \int_{\Omega} \delta \mathbf{u} \cdot \mathbf{b} d\Omega - \int_{\Gamma_u} \delta \mathbf{u} \cdot \bar{\mathbf{t}} d\Gamma - \delta \mathbf{W}_u(\mathbf{u}, \nabla_s \lambda) = 0 \quad (3.4)$$

Where $\delta \boldsymbol{\varepsilon} = \nabla_s(\delta \mathbf{u})$, ∇_s is the symmetric gradient operator. The term $\delta \mathbf{W}_u$ is a term to enforce the essential boundary conditions. The term $\delta \mathbf{W}_u$ is needed, because in contrast to finite element methods since $\Phi_I(x_J) \neq \delta_{IJ}$ it is not sufficient to set the nodal displacements to enforce the essential boundary conditions. Several forms of \mathbf{W}_u are possible. If, Lagrange multiplier method is considered, then

$$\mathbf{W}_u(\mathbf{u}, \lambda) = \int_{\Gamma_u} \lambda \cdot (\mathbf{u} - \bar{\mathbf{u}}) d\Gamma \quad (3.5)$$

$$\delta \mathbf{W}_u(\mathbf{u}, \lambda) = \int_{\Gamma_u} \delta \lambda \cdot (\mathbf{u} - \bar{\mathbf{u}}) d\Gamma + \int_{\Gamma_u} \delta \mathbf{u} \cdot \lambda d\Gamma \quad (3.6)$$

3.1.1.1 Discrete Equation

We now consider linear elasticity where

$$\boldsymbol{\varepsilon} = \nabla_s \mathbf{u} \quad (3.7)$$

$$\boldsymbol{\sigma} = \mathbf{D} \boldsymbol{\varepsilon} \quad (3.8)$$

Where, $\boldsymbol{\varepsilon}$ is the strain and \mathbf{D} is a matrix of material moduli. We consider the discrete equation for the weak form Eq.(3.4) with the essential boundary conditions in Eqs.(3.5) and (3.6). The Lagrange multiplier λ is expressed by

$$\begin{aligned} \lambda(\mathbf{x}) &= N_I(s)\lambda_I, & \mathbf{x} \in u \\ \delta \lambda(\mathbf{x}) &= N_I(s)\delta \lambda_I, & \mathbf{x} \in u \end{aligned} \quad (3.9)$$

where, $N_{I(s)}$ a Lagrange interpolant & s is the arc length along the boundary; the repeated indices designate summations. In the variational form of equilibrium Eq.(3.4), replace $u(\mathbf{x})$ with the EFG approximation $u^h(\mathbf{x})$, and replace the variation $\delta u(\mathbf{x})$ with the EFG approximation $\delta u^h(\mathbf{x})$, where δu^h , by Galerkin approximation technique is comprised of the same shape function as in

$$u^h : u^h(\mathbf{x}) = \sum_{I=1}^n \Phi_I(\mathbf{x}) u_I \quad (3.10)$$

and

$$\delta u^h(\mathbf{x}) = \sum_{I=1}^n \Phi_I(\mathbf{x}) \delta u_I \quad (3.11)$$

The nodal test function values δu_I are arbitrary, except on Γ_u , and can be eliminated from the equations.

Also, substitute Eq.(3.9) into the weak form Eq.(3.4), which yields:

$$\begin{bmatrix} \mathbf{K} & \mathbf{G} \\ \mathbf{G}^T & 0 \end{bmatrix} \begin{Bmatrix} \mathbf{u} \\ \lambda \end{Bmatrix} = \begin{Bmatrix} \mathbf{f} \\ \mathbf{q} \end{Bmatrix} \quad (3.12)$$

where,

$$\mathbf{K}_u = \int_{\Omega} \mathbf{B}^T \mathbf{D} \mathbf{B}_J d\Omega \quad (3.13a)$$

$$\mathbf{G}_{IK} = - \int_{\Gamma_u} \Phi_I \mathbf{N}_k d\Gamma_u \quad (3.13b)$$

$$\mathbf{f}_I = \int_{\Gamma_I} \Phi_I \bar{\mathbf{t}} d\Gamma_I + \int_{\Omega} \Phi_I \mathbf{b} d\Omega \quad (3.13c)$$

$$\mathbf{q}_k = - \int_{\Gamma_u} \mathbf{N}_k \bar{\mathbf{u}} d\Gamma_u \quad (3.14)$$

where,

$$\mathbf{B}_I = \begin{bmatrix} \Phi_{I,x} & 0 \\ 0 & \Phi_{I,y} \\ \Phi_{I,y} & \Phi_{I,x} \end{bmatrix} \quad (3.15)$$

$$\mathbf{N}_k = \begin{bmatrix} N_k & 0 \\ 0 & N_k \end{bmatrix} \quad (3.16)$$

$$\mathbf{D} = \frac{E}{(1+\nu)(1-2\nu)} \begin{bmatrix} 1-\nu & \nu & 0 \\ \nu & 1-\nu & 0 \\ 0 & 0 & \frac{1-2\nu}{2} \end{bmatrix} \quad \text{For plane strain} \quad (3.17)$$

$$\mathbf{D} = \frac{E}{1-\nu^2} \begin{bmatrix} 1 & \nu & 0 \\ \nu & 1 & 0 \\ 0 & 0 & \frac{1-\nu}{2} \end{bmatrix} \quad \text{For plane stress} \quad (3.18)$$

In which a comma designates a partial derivative with respect to the indicated spatial variable; E and ν are Young's modulus and Poisson's ratio, respectively.

3.1.2 Modified Variational Principle

The variational (or weak) form of the equilibrium Eq.(3.1) can be obtained as follows.

Consider trial functions $u(x) \in H^1$ and Lagrange multipliers $\lambda \in H^0$, test functions $\delta v(x) \in H^1$ and $\delta \lambda \in H^0$ then

$$\int_{\Omega} \nabla_s \delta u : \sigma d\Omega - \int_{\Omega} \delta u \cdot b d\Omega - \int_{\Gamma_t} \delta u \cdot \bar{t} d\Gamma - \int_{\Gamma_u} \delta \lambda \cdot (u - \bar{u}) d\Gamma - \int_{\Gamma_u} \delta u \cdot \lambda d\Gamma = 0$$

$$\forall \delta v \in H^1, \delta \lambda \in H^0 \quad (3.19)$$

Using Eq. (3.19) to obtain the modified variational principle integrate the first term on the left side by parts

$$\int_{\Gamma} \delta u \cdot t d\Gamma - \int_{\Omega} \delta u \cdot (\nabla \cdot \sigma + b) d\Omega - \int_{\Gamma_t} \delta u \cdot \bar{t} d\Gamma - \int_{\Gamma_u} \delta \lambda \cdot (u - \bar{u}) d\Gamma - \int_{\Gamma_u} \delta u \cdot \lambda d\Gamma \quad (3.20a)$$

or

$$-\int_{\Omega} \delta u \cdot (\nabla \cdot \sigma + b) d\Omega - \int_{\Gamma_t} \delta u \cdot (\bar{t} - t) d\Gamma - \int_{\Gamma_u} \delta \lambda \cdot (u - \bar{u}) d\Gamma - \int_{\Gamma_u} \delta u \cdot (\lambda - t) d\Gamma = 0 \quad (3.20b)$$

where $t = \sigma \cdot n$ is the traction along the boundary. It can be seen from the above equation that for all variations δu and $\delta \lambda$, the first term on the left side gives the equilibrium equation, the second term the natural boundary condition on Γ_t and the third term the essential boundary condition on Γ_u . The last term on the left side of Eq.(3.20b) must vanish for all variation δu which requires

$$\lambda = t \text{ on } \Gamma_u \quad (3.21)$$

i.e. the physical meaning of Lagrange multipliers λ is traction along the boundary Γ_u . Hence after substituting Eq.(3.21) into Eq.(3.19) the modified variational principle is obtained as

$$\int_{\Omega} \nabla_S \delta u : \sigma d\Omega - \int_{\Omega} \delta u \cdot b d\Omega - \int_{\Gamma_t} \delta u \cdot \bar{t} d\Gamma - \int_{\Gamma_u} \delta t \cdot (u - \bar{u}) d\Gamma - \int_{\Gamma_u} \delta u \cdot t d\Gamma = 0 \quad (3.22)$$

The discrete equation obtained by substituting test and trial functions in the weak form Eq.(3.22) will lead to K matrix which is symmetric and banded.

3.1.3 Penalty Function

In order to realize the penalty, an additional term appears in the variational equation in Eq.(3.4) as:

$$\frac{\alpha}{2} \int_{\Gamma} D(u)^T D(u) d\Gamma \quad (3.23)$$

Applying the penalty function to elastostatics, we get the following weak form

$$\int_{\Omega} \varepsilon^T(u) : D : \varepsilon(v) d\Omega = \int_{\Gamma} \bar{t} \cdot v d\Gamma + \int_{\Omega} b \cdot v d\Omega + \alpha \int_{\Gamma_u} u \cdot v d\Gamma - \alpha \int_{\Gamma_u} \bar{u} \cdot v d\Gamma \quad (3.24)$$

which gives the equation $Ku = f$, where

$$K_{IJ} = \int_{\Omega} B_I^T \cdot DB_J d\Omega - \alpha \int_{\Gamma_u} \phi_I \phi_J d\Gamma \quad (3.25)$$

$$f_{IJ} = \int_{\Gamma_t} \phi_I \cdot \bar{t} d\Gamma + \int_{\Omega} \phi_I b d\Omega - \alpha \int_{\Gamma_u} \phi_I \bar{u} d\Gamma \quad (3.26)$$

Penalty method is advantageous over Lagrange multiplier approach because there is no need of additional unknowns. However, the conditioning of the matrix much depends on the choice of the penalty parameter.

Another approach called as the augmented Lagrangian method has been proposed by to [68] handle essential boundary conditions in meshless methods. This method proved to be stable and effective, particularly in the case of contact problems where it has replaced the penalty and Lagrangian multipliers methods.

3.1.4 Transformation Method

As the MLS shape function lack the property of Kronecker delta the further formulation poses some difficulties in imposing essential boundary conditions in EFGM. In this section, a full transformation method [49], is elaborated for fracture mechanics applications [59].

Consider the transformations,

$$\hat{u} = \Lambda u \quad (3.27)$$

where,

$$\hat{u} = \begin{Bmatrix} u_1^h(x_1) \\ u_2^h(x_1) \\ u_1^h(x_2) \\ u_1^h(x_2) \\ \vdots \\ u_1^h(x_N) \\ u_1^h(x_N) \end{Bmatrix} \in \Re^{2N} \quad (3.28)$$

Is the nodal displacement vector

$$\Lambda = \begin{bmatrix} {G_{11}}^T \\ {G_{21}}^T \\ {G_{12}}^T \\ {G_{22}}^T \\ \vdots \\ {G_{1N}}^T \\ {G_{2N}}^T \end{bmatrix} \in \mathcal{L}(\Re^{2N} \times \Re^{2N}) \quad (3.29)$$

is the transformation matrix. Multiplying the first set of matrix equation in Eq.(3.11) by Λ^{-T} , one obtains

$$\begin{bmatrix} \Lambda^{-T} k & {I_{ij}}^T \\ G^T & 0 \end{bmatrix} \{u\} = \begin{Bmatrix} \Lambda^{-T} f \\ q \end{Bmatrix} \quad (3.30)$$

Where

$$I_{ij} = \Lambda^{-T} G^T = \begin{Bmatrix} 0 \\ \vdots \\ 0 \\ 1 \\ 0 \\ \vdots \\ 0 \end{Bmatrix} \leftarrow [2(j-1) + i] \text{ th row} \quad (3.31)$$

Let,

$$\hat{k} = \begin{bmatrix} \hat{k}_1^T \\ \vdots \\ \hat{k}_{2N}^T \end{bmatrix} = \Lambda^{-T} k \quad (3.32)$$

$$\hat{f} = \Lambda^{-T} f \quad (3.33)$$

where $\hat{k}_i^T = \{\hat{k}_{i1}, \hat{k}_{i2}, \dots, \hat{k}_{i(2N)}\}$, $i = 1, 2, \dots, 2N$. Eq. (3.30) can also be written as

$$\begin{bmatrix} \hat{k}_1^T & 0 \\ \vdots & \vdots \\ \hat{k}_{M-1}^T & 0 \\ \hat{k}_M^T & 1 \\ \hat{k}_{M+1}^T & 0 \\ \vdots & \vdots \\ \hat{k}_{2N}^T & 0 \\ \hat{\Phi}_j^{i^T} & 0 \end{bmatrix} \begin{Bmatrix} u \\ \lambda \end{Bmatrix} = \begin{Bmatrix} \hat{f}_1 \\ \vdots \\ \hat{f}_{M-1} \\ \hat{f}_M \\ \hat{f}_{M+1} \\ \vdots \\ \hat{f}_{2N} \\ q \end{Bmatrix} \quad (3.34)$$

where \hat{f}_{M-1} is the $[2(j-1)+i]$ th row and q is the $(2N+1)$ th row and $M = (2j-1) + i$. Exchanging the M th and the last row of Eq.(3.34) leads to

$$\begin{bmatrix} \hat{k}_1^T & 0 \\ \vdots & \vdots \\ \hat{k}_{M-1}^T & 0 \\ G^T & 1 \\ \hat{k}_{M+1}^T & 0 \\ \vdots & \vdots \\ \hat{k}_{2N}^T & 0 \\ \hat{k}_M^T & 0 \end{bmatrix} \begin{Bmatrix} u \\ \lambda \end{Bmatrix} = \begin{Bmatrix} \hat{f}_1 \\ \vdots \\ \hat{f}_{M-1} \\ q \\ \hat{f}_{M+1} \\ \vdots \\ \hat{f}_{2N} \\ \hat{f}_M \end{Bmatrix} \quad (3.35)$$

where \hat{f}_{M-1} is the $[2(j-1)+i]$ th row and \hat{f}_M is the $(2N+1)$ th row which can be uncoupled as

$$Ku = F \quad (3.36)$$

$$\hat{k}_M^T u + \lambda = \hat{f}_M \quad (3.37)$$

$$K = \mathcal{M}_{ij}(\hat{k}) = \begin{bmatrix} \hat{k}_1^T \\ \vdots \\ \hat{k}_{M-1}^T \\ G^T \\ \hat{k}_{M+1}^T \\ \vdots \\ \vdots \\ \hat{k}_{2N}^T \end{bmatrix} \leftarrow [2(j-1) + i] \quad (3.38)$$

and

$$F = \aleph_{ij}(\hat{f}) = \begin{bmatrix} \hat{f}_1 \\ \vdots \\ \hat{f}_{M-1} \\ q \\ \hat{f}_{M+1} \\ \vdots \\ \vdots \\ \hat{f}_{2N} \end{bmatrix} \leftarrow [2(j-1) + i]^{th} row \quad (3.39)$$

are the modified stiffness matrix and force vectors respectively. There is no need for Lagrange multipliers as the generalized displacement vector, u can be solved efficiently using Eq. (3.36).

In Eqs.(3.38) and (3.39) \mathcal{M}_{ij} is a matrix operator that replaces the $[2(j-1) + i]^{th}$ row of \hat{k} by G^T and \aleph_{ij} is another matrix operator that replaces the $[2(j-1) + i]^{th}$ row of \hat{f} by q due to the applications of a single boundary constraint at node J . For multiple boundary constraints, similar operations can be repeated. Suppose ,there are N_e number of essential boundary conditions , i_1, i_2, \dots, i_{N_e} ,respectively. Hence, the resulting modified stiffness matrix and force vectors are

$$K = \prod_{l=1}^{N_e} \mathcal{M}_{ilj}(\hat{k}) \quad (3.40)$$

and,

$$F = \prod_{l=1}^{N_e} \aleph_{ilj}(\hat{f}) \quad \text{respectively.} \quad (3.41)$$

3.2 Conclusion

This chapter summarizes the various methods used in EFGM for enforcement of essential boundary conditions:

- Lagrange multiplier approach provides best accuracy in results compared to other methods.
- Transformation method eliminates the problems with Lagrange's multiplier method like loss of Kronecker delta property.

CHAPTER 4

DISCONTINUITY MODELING IN EFGM

4.1 Discontinuities

EFGM is one of the best tools to carry out discretization of partial differential equations because there is no need of arduous mesh generation and it can handle the growth of discontinuities such as cracks and interfaces easily. Also, there is no need of post processing of partial derivatives of the approximations, such as strains in the elastic problem as these methods naturally lead to continuous differentiable approximations which are not the case with finite element methods.

While, dealing with fracture analysis of various geometries discontinuities can be present in the domain in the form of strong or weak discontinuity. Theory of plasticity is basically designed for problems where displacement field and usually strain field remains continuous while fracture mechanics is formulated to deal with strong discontinuity where both strain and displacement fields are discontinuous across the crack surface.

There are different methods for handling of strong and weak discontinuities which will be discussed in ensuing sections. For modelling strong discontinuities the earliest work was done by enriching test and trial functions [24,52,67], afterwards modification were made in weight function such as the visibility method, the diffraction method and the transparency method [60,67,69–71], also methods based on the extrinsic PUM enrichment [72–74] proved to be very effective. The modeling of weak discontinuities was first done by domain partitioning approach [75] which produced very accurate displacement results however oscillations about the exact solution were inherent while taking derivatives of displacement. Later on a special technique for the incorporation of discontinuities in derivatives of meshless solutions was presented [16,36].

4.1.1 Modeling Of Weak Discontinuities

Weak (material) discontinuities are discontinuities in derivatives (strain) at material interfaces (bi-material) or inclusions. Three main approaches are present

to deal with material discontinuities which are domain partitioning approach, Lagrange multiplier approach and Jump function approach.

4.1.1.1 Modifications For Material Discontinuity (Domain Partitioning Approach)

Modifications were made to define material discontinuity in terms of domain of influence in homogeneous and inhomogeneous material. Few modifications and additions were introduced in EFGM to solve the weak discontinuity problems. These changes give EFGM an ability to solve the problems involving material discontinuities. The modifications in the approaches are discussed below:

In domain partitioning approach [75] the following weak/variational form of $\nabla \cdot \sigma + b = 0$ is considered in Ω along with associated boundary constraint applied using Lagrange multipliers λ

$$\int_{\Omega} \nabla_S \delta u : \sigma d\Omega - \int_{\Omega} \delta u b d\Omega - \int_{\Gamma_t} \delta u \bar{t} d\Gamma - \int_{\Gamma_u} \delta \lambda (u - \bar{u}) d\Gamma - \int_{\Gamma_u} \delta u \lambda d\Gamma = 0 \quad (4.1)$$

Corresponding to the satisfaction of the equilibrium equation $\nabla \cdot \sigma + b = 0$ on Ω in both Ω^+ and Ω^- ; the traction and displacement boundary conditions, $\sigma \cdot \bar{n} = \bar{t}$ on Γ_t in both Γ_t^+ and Γ_t^- , $u = \bar{u}$ on Γ_u in both Γ_u^+ and Γ_u^- . The discretization of the above Eq.(4.1) after imposing boundary conditions leads to the following set of linear equations:

$$\begin{bmatrix} \mathbf{K} & \mathbf{G} \\ \mathbf{G}^T & 0 \end{bmatrix} \begin{Bmatrix} \mathbf{u} \\ \boldsymbol{\lambda} \end{Bmatrix} = \begin{Bmatrix} \mathbf{f} \\ \mathbf{q} \end{Bmatrix} \quad (4.2)$$

In this method, the inhomogeneous material is viewed as a combination of two separate homogeneous materials and modifications are applied at the interface. The weight function selected for the simulation of the problem helps in separation of body into its homogeneous parts and the neighbors are decided on the basis of domain of influence specifically. For a homogeneous part, the neighbors at a point x are the nodes which contain x in their domain of influence [34]. In case of inhomogeneous materials, the interface is defined by a set of nodes that belong to both the materials. The line drawn by connecting these nodes is considered as the interface Γ_s between two materials (material-1 and material-2). Therefore, the

points enclosed in material-1 can only be influenced by the nodes in material-1 plus interface nodes; and points enclosed in material-2 can only be influenced by nodes restricted to material-2 in addition to interface nodes. Figs.(4.1-4.2) illustrate the selection of the neighbors for homogeneous and inhomogeneous materials respectively. The domains of influence are drawn for nodes labeled 1 through 5 in each figure to determine the neighbors for the points *a*, *b* and *c*. The domain of influence for each node is a circle centered at the node. For the homogeneous case (Fig.4.1), point *a* is inside the domain of influence of two nodes i.e. 4 and 5; therefore, nodes 4 and 5 are considered the neighbors of the point *a*. Similarly, point *b* has nodes 3 and 5 as neighbors, and point *c* has nodes 1 and 2 as neighbors. However, when an interface separating two materials is added as in Fig.4.2, the neighbors of the points *a*, *b* and *c* change. The domains of influence for node 4 and node 5 are unaffected by the interface. The domain of influence for node 4 does not intersect the interface, and node 5 is an interface node owned by both materials. Therefore, point *a* is still considered in the neighborhood of nodes 4 and 5. The domains of influence for nodes 1, 2 and 3 are truncated at the interface. The neighbors of point *b* still include nodes 3 and 5 since each is relevant to material-1 but, point *c* is not considered in the domain of influence of node 2 due to the truncation of the domain of influence of node 2 at the interface. Similarly, point *c* has only one neighbor labeled in Fig.4.2 i.e. node 1.

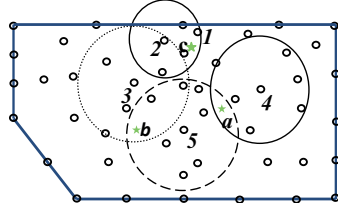


Fig.4.1 Domains of influence and nearest neighbors in homogeneous bodies

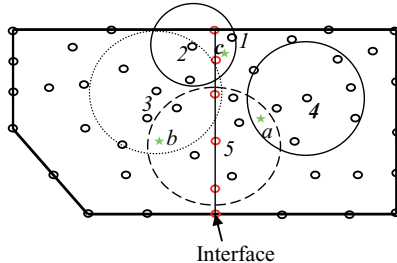


Fig.4.2 Domains of influence and nearest neighbors in inhomogeneous bodies

4.1.1.2 Lagrange Multiplier Approach

In this approach, the following interface constraint is applied apart from essential and traction boundary conditions [34]:

$$\int_{\Gamma_s} (\mathbf{u}^+ - \mathbf{u}^-) d\Gamma = 0 \quad (4.3)$$

Hence, the following weak form of $\nabla \cdot \sigma + \mathbf{b} = 0$ is used on Ω using interface condition:

$$\begin{aligned} & \int_{\Omega} \nabla_s \delta \mathbf{u} : \boldsymbol{\sigma} d\Omega - \int_{\Omega} \delta \mathbf{u} \mathbf{b} d\Omega - \int_{\Gamma_t} \delta \mathbf{u} \bar{\mathbf{t}} d\Gamma - \int_{\Gamma_u} \delta \lambda (\mathbf{u} - \bar{\mathbf{u}}) d\Gamma - \int_{\Gamma_u} \lambda \delta \mathbf{u} d\Gamma - \\ & \int_{\Gamma_s} (\mathbf{u}^+ - \mathbf{u}^-) \delta \gamma d\Gamma - \int_{\Gamma_s} \gamma (\delta \mathbf{u}^+ - \delta \mathbf{u}^-) d\Gamma = 0 \end{aligned} \quad (4.4)$$

The Lagrange multipliers λ , enforce the essential boundary constraint on Γ_u , while the Lagrange multiplier γ enforce the displacement discontinuity. The associated Euler equations are as follows:

$$\nabla \cdot \boldsymbol{\sigma} + \mathbf{b} = 0 \text{ in } \Omega^+ \text{ and } \Omega^-, \quad (4.5)$$

$$\mathbf{t} - \bar{\mathbf{t}} = 0 \quad \text{on } \Gamma_t^+ \text{ and } \Gamma_t^-, \quad (4.6)$$

$$\mathbf{u} - \bar{\mathbf{u}} = 0 \quad \text{on } \Gamma_u^+ \text{ and } \Gamma_u^-, \quad (4.7)$$

$$\lambda - \bar{\lambda} = 0 \quad \text{on } \Gamma_u^+ \text{ and } \Gamma_u^-, \quad (4.8)$$

$$\mathbf{u}^+ - \mathbf{u}^- = 0 \quad \text{on } \Gamma_s \quad (4.9)$$

$$\gamma + \mathbf{t}^+ = 0 \quad \text{on } \Gamma_s \quad (4.10)$$

$$\gamma + \mathbf{t}^- = 0 \quad \text{on } \Gamma_s \quad (4.11)$$

Corresponding to the satisfaction of the equilibrium equation $\nabla \cdot \sigma + \mathbf{b} = 0$ on Ω in both Ω^+ and Ω^- ; the traction and displacement boundary conditions, $\sigma \cdot \bar{\mathbf{n}} = \bar{\mathbf{t}}$ on Γ_t in both Γ_t^+ and Γ_t^- , $u = \bar{u}$ on Γ_u in both Γ_u^+ and Γ_u^- . Substituting Eq.(4.8) and Eq.(4.10) into Eq.(4.4), the following equations are obtained:

$$\int_{\Omega} \nabla_s \delta \mathbf{u} : \boldsymbol{\sigma} d\Omega - \int_{\Omega} \delta \mathbf{u} \mathbf{b} d\Omega - \int_{\Gamma_u} \delta \mathbf{u} \bar{\mathbf{t}} d\Gamma - \int_{\Gamma_u} \delta \mathbf{t} (\mathbf{u} - \bar{\mathbf{u}}) d\Gamma - \int_{\Gamma_u} \mathbf{t} \delta \mathbf{u} d\Gamma - \int_{\Gamma_s} (\mathbf{u}^+ - \mathbf{u}^-) \delta \mathbf{t}^- d\Gamma - \int_{\Gamma_s} \mathbf{t}^- (\delta \mathbf{u}^+ - \delta \mathbf{u}^-) d\Gamma = 0 \quad (4.12)$$

The discretization of the above Eq.(4.12), leads to the following set of linear equations:

$$Ku = f \quad (4.13)$$

where, the matrices K and f are defined as

$$K_{IJ} = \int_{\Omega} B_I^T D B_J d\Omega - \int_{\Gamma_u} \Phi_I S N D B_J d\Gamma + \int_{\Gamma_u} B_I^T D^T N^T S \Phi_J d\Gamma - \int_{\Gamma_s} (\Phi_I^+ - \Phi_I^-) N^- D^- B_J^- d\Gamma + \int_{\Gamma_s} (B_I^-)^T (D^-)^T (N^-)^T (\Phi_J^+ - \Phi_J^-) d\Gamma \quad (4.14)$$

$$f_I = \int_{\Gamma_i} \Phi_I \bar{\mathbf{t}} d\Gamma - \int_{\Gamma_u} B_I^T D^T N^T S \bar{\mathbf{u}} d\Gamma + \int_{\Omega} \mathbf{b} \Phi_I d\Omega \quad (4.15)$$

$$\mathbf{D} = \frac{E}{1-v^2} \begin{bmatrix} 1 & v & 0 \\ v & 1 & 0 \\ 0 & 0 & \frac{1-v}{2} \end{bmatrix} \text{ for plane stress} \quad (4.16)$$

$$\mathbf{B}_I = \begin{bmatrix} \Phi_{I,x} & 0 \\ 0 & \Phi_{I,y} \\ \Phi_{I,y} & \Phi_{I,x} \end{bmatrix} \quad (4.17)$$

$$\mathbf{N} = \begin{bmatrix} n_x & 0 & n_y \\ 0 & n_y & n_x \end{bmatrix} \quad \mathbf{S} = \begin{bmatrix} s_x & 0 \\ 0 & s_y \end{bmatrix} \quad (4.18)$$

$$s_x = \begin{cases} 1, & \text{if the prescribed } u_x \text{ on } \Gamma_u \\ 0, & \text{if the prescribed } u_y \text{ on } \Gamma_u \end{cases} \quad (4.19a)$$

$$s_y = \begin{cases} 0, & \text{if the prescribed } u_x \text{ on } \Gamma_u \\ 1, & \text{if the prescribed } u_y \text{ on } \Gamma_u \end{cases} \quad (4.19b)$$

4.1.1.3 Jump Function Approach

It is a well-established technique for handling various weak discontinuity problems using EFGM [16,38]. The enrichment of EFGM approximations is done by adding special shape functions (jump functions) that contain discontinuities in the derivative [36].

4.1.1.3.1 Discontinuities In Derivatives

One dimension

Consider the problem of constructing an approximation in one dimension with discontinuous first derivatives at a prescribed set of points $x_J, J = 1, \dots, n_d$. For simplicity, sufficient numbers of nodes between the discontinuities are assumed so that they do not interfere with each other these conditions are introduced later. The approximation is then given by

$$u^h(\mathbf{x}) = u^{EFGM}(\mathbf{x}) + q^J(s)\Psi_J(\mathbf{r}) \quad (4.20)$$

where, u^{EFGM} is the standard EFGM approximation, which is given as:

$$u^{EFGM}(\mathbf{x}) = \sum_{I=1}^n \Phi_I(\mathbf{x})u_I \quad (4.21)$$

q^J are amplitude parameters of the jumps, and $\Psi_J(r)$ are the Jump shape functions. s provides parameterization of the line of discontinuity, and q^J is discretized as follows:

$$q^J(s) = \sum_I N_I(s) q_I^J \quad (4.22)$$

where, $N_I(s)$ are one-dimensional shape functions which need to be C^1 continuous so that they do not introduce any discontinuities in derivatives other than across the

discontinuity line. From Eq.(4.20), it is clear that constant and linear fields will still be reproduced exactly when $q' = 0$.

The following two properties are deemed to be desirable:

1. The jump term has compact support so that the discrete equations remain banded.
2. The approximation Eq.(4.20) is able to reproduce the derivative in the form of a Heaviside step function exactly.

The jump function Ψ_j is constructed from polynomials with the discontinuity in derivatives built-in. Let Ψ_j be equal to $\Psi_j(\bar{r}_j)$, where $\bar{r}_j = r_j / d_{ml}$; r_j is the distance to the J^{th} point of discontinuity and d_{ml} is the domain of influence. The function Ψ_j is generated subject to the following conditions:

$$\Psi_j(1) = 0, \quad (4.23)$$

$$\Psi'_j(1) = 0, \quad (4.24)$$

$$\Psi'_j(0) = -0.5, \quad (4.25)$$

These will make the function and its derivative continuous everywhere except at x_j . If the continuity of second derivatives of the approximation is desired at points other than points of discontinuity, we also require $\Psi''_j(1) = 0$. Since there are now four conditions the minimal order of a polynomial that satisfies all of them is cubic. The cubic is given by:

$$\Psi_j(\bar{r}_j) = \begin{cases} \frac{-1}{6}\bar{r}_j^3 + \frac{1}{2}\bar{r}_j^2 - \frac{1}{2}\bar{r}_j + \frac{1}{6} & \bar{r}_j \leq 1 \\ 0 & \bar{r}_j \geq 1 \end{cases} \quad (4.26)$$

This form of jump term satisfies the compact support condition; however, Eq.(4.20) with the jump term in the form of Eq. (4.22) will only approximate a derivative in the form of a Heaviside shape function.

Extension to two dimensions

Consider a two-dimensional model with n_d lines at which discontinuities in derivatives are possible. The approximation becomes

$$u^h(\mathbf{x}) = u^{EFGM}(\mathbf{x}) + q^J(s)\Psi_J(\mathbf{r}) \quad (4.27)$$

with r denoting the distance to the closest point on the line of discontinuity (r is positive on one side of the discontinuity and negative on the other, an example to clarify the definition of r is shown in Fig.4.3) s provides a parameterization of the line of discontinuity. Now discretize q^J as follows:

$$q^J(s) = \sum_I N_I(s) q_I^J \quad (4.28)$$

where N_I are one-dimensional shape functions which need to be C^1 so they do not introduce any discontinuities in the derivatives other than across the discontinuity line.

A discontinuity in two dimensions is shown in Fig.4.3. The distance r from the node to the line of discontinuity is taken as positive for the nodes lying on the right side of the line of discontinuity while for the nodes on left side r is taken as negative. For example r_I and r_J are positive while r_K and r_L are negative.

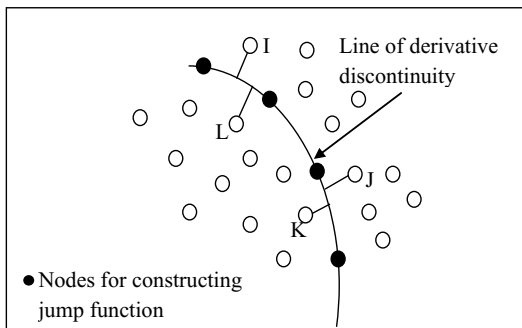


Fig.4.3 Discontinuity and sign convention for r in two dimensions.

4.1.2 Modeling Of Strong Discontinuities

Strong discontinuities such as cracks cause a discontinuity in both strain and displacement fields. There are basically six ways to model cracks in EFGM. These methods can be classified under two broad categories first are smoothening

techniques based on modification in weight function and then enrichment techniques based on PU concept which involve enrichment of basis function extrinsically or extrinsically.

4.1.2.1 Smoothening Techniques

This section discusses the techniques for modeling non-convex boundaries and strong discontinuities. The smoothness which is a natural property of meshless methods provides approximations of functions and their derivatives which are smooth and have the same continuity as the weight function, on the other hand in cases where a discontinuity is present in geometry or the material, this higher order smoothness causes difficulties which lead to a loss in accuracy. Due to this antecedent smoothness special treatments are given to non-convex boundaries [57] which will be elaborated.

4.1.2.1.1 Visibility Criterion

The was the first technique for dealing with strong discontinuities is the visibility criterion [14,41]. In this straightforward approach, the strong discontinuities such as cracks are considered to be opaque and domain of influence is considered as the field of vision at a node. All the nodes that are not truncated by the opaque boundary are not considered in the displacement field approximation. Consider node J in Fig.4.4, where the surface of the crack is within its domain of influence and is therefore truncated. This truncation creates a discontinuity in the shape function for node J which will lead to the desired discontinuity in the solution across the crack.

A difficulty with the visibility criterion arises for nodes in close proximity of crack tip. Consider node I in Fig.4.4. The field of vision is cut by the crack, leading to a discontinuity along line AC , i.e. the line of the crack. However, the field of vision is also truncated along line AB , which extends into the domain which is an undesired discontinuity.

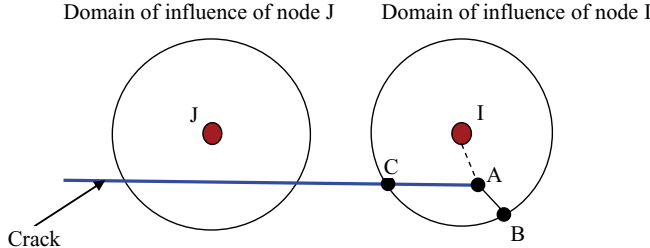


Fig.4.4: Domain of influence by visibility criterion near a crack

4.1.2.1.2 Diffraction Technique

Continuous and smooth approximations near nonconvex boundaries can be constructed quite easily by the diffraction technique. The domain of influence is wrapped around nonconvex boundaries similar to the way light diffracts around sharp corners as shown in Fig.4.5. This technique, which has also been called the wrap-around technique [60].

Consider Fig.4.5, where a line between the node x_I , and a sampling point x intersects a crack and the tip is within the domain of influence of the node. The weight function distance d_I , is described here by

$$d_I = \left(\frac{s_1 + s_2(x)}{s_0(x)} \right)^\lambda s_0(x) \quad (4.29)$$

where,

$$s_1 = \|x_I - x_c\|, \quad s_2(x) = \|x - x_c\|, \quad s_0(x) = \|x - x_I\| \quad (4.30)$$

And x_I is the node, x is the sampling point, and x_c is the crack tip. The parameter λ is used to adjust the distance of the support on the opposite side of the crack. It was found that $\lambda=1, 2$ perform well

The spatial derivatives of the weight function are computed using the chain rule:

$$\frac{dw}{dx_i} = \frac{\partial w}{\partial d_I} \frac{\partial d_I}{\partial x_i} \quad (4.31)$$

Since $\partial w / \partial d_I$ is unchanged, all that is necessary are expressions for $\partial d_I / \partial x_i$

$$\frac{\partial d_I}{\partial x_i} = \lambda \left(\frac{s_1 + s_2}{s_0} \right)^{\lambda-1} \frac{\partial s_2}{\partial x_i} + (1 - \lambda) \left(\frac{s_1 + s_2}{s_0} \right)^\lambda \frac{\partial s_0}{\partial x_i} \quad (4.32)$$

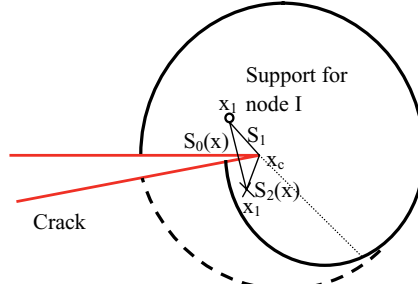


Fig.4.5 Diffraction (wrap-around) technique for constructing smooth weight functions around non-convex boundaries

where,

$$\frac{\partial s_0}{\partial x_i} = \frac{x_i - x_{l_i}}{s_0}, \quad \frac{\partial s_2}{\partial x_i} = \frac{x_i - x_{c_i}}{s_2} \quad (4.33)$$

The diffraction technique works well for general nonconvex boundaries as well. The tangent point between the node and the nonconvex boundary is used as the wrap-around point x_c .

4.1.2.1.3 Transparency Technique

Another technique for constructing continuous approximations considered as a substitute to diffraction technique is the transparency technique [60]. The basic concept of this technique is to bestow the crack tip with a varying measure of transparency such that it is completely transparent at the tip and becomes completely opaque a short distance behind the tip. By doing this, the abrupt truncation of field of vision of node close to crack tip does not take place, but rather diminishes smoothly to zero a short distance behind the tip of the crack.

When a ray passes between a node x_l and a sampling point x , and crosses the crack as shown in Fig.4.6, the distance parameter d_I in the weight function is modified (lengthened) by the following:

$$d_I(\mathbf{x}) = \mathbf{s}_0(\mathbf{x}) + d_{ml} \left(\frac{s_c(\mathbf{x})}{s_c} \right)^\lambda \quad \lambda \geq 2 \quad (4.34)$$

Where, $s_0(\mathbf{x}) = \|\mathbf{x} - \mathbf{x}_I\|$, d_{ml} is the radius of support for node I , and $s_c(\mathbf{x})$ is the intersection distance behind the crack.

The parameter s_c sets the distance behind the crack tip at which complete opacity occurs:

$$s_c = kh \quad (4.35)$$

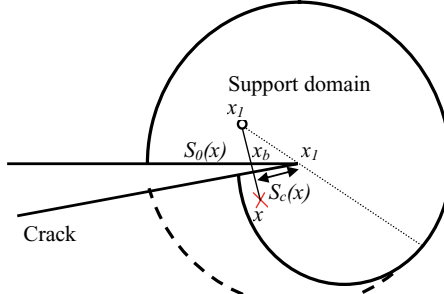


Fig.4.6 Transparency technique for computing smooth weight functions

Where, h is the nodal spacing and k is a constant, usually $0 < k < 1$.

The spatial derivatives of the distance parameter, d_I obtained by chain rule, are

$$\frac{\partial d_I}{\partial x_i} = \frac{\partial s_0}{\partial x_i} + \lambda d_{ml} \frac{s_c^{\lambda-1}}{s_c^{-\lambda}} \frac{\partial s_c}{\partial x_i} \quad (4.36)$$

Where, $\frac{\partial s_0}{\partial x_i} = \frac{x_i - x_b}{s_0}$, $\frac{\partial s_c}{\partial x_i} = \frac{x_b - x_c}{s_c} = \cos\theta$, $\frac{\partial s_c}{\partial x_i} = \frac{y_b - y_c}{s_c} = -\sin\theta$, θ is the angle between the crack and x -axis and x_b is the intersection point behind the crack tip.

One drawback of the transparency technique is that it does not work well when nodes are placed too close to the crack surface. Note the trough which appears in the shape function ahead of the crack. This trough appears because although the crack tip is transparent for this node, the change in the degree of transparency with respect to the change in angle is very sharp. To circumvent this problem in the

transparency technique, a restriction has been placed on the position of the nodes. All nodes should be placed so that the normal distance from the node to the crack surface is greater than roughly $1/4h$, where h is the nodal spacing.

4.1.2.2 Enrichment Techniques

The isoparametric finite elements can be enriched by the inclusion of near crack tip fields in trial functions to capture stress field oscillations or singular stress fields in finite elements. This method can provide the stress intensity factor directly as a part of solution. However, the results of elements enriched by singular fields are dependent on their size, and fail to exhibit uniform convergence. The other difficulty associated with these elements is that their implementation becomes intricate because the stiffness matrix and force vector have to be expanded to compensate for the extra unknowns.

4.1.2.2.1 Extrinsic Enrichment

In extrinsic enrichment of a meshfree approximation, trial functions are augmented to include the first term of the near-tip asymptotic expansion for the displacement fields. This can be done by two different ways.

4.1.2.2.1.1 Extrinsic MLS Enrichment

In extrinsic enrichment of a meshfree approximation, a function closely related to the solution is added to the polynomial expansion of MLS approximation. For example, in linear elastic fracture mechanics, the near tip asymptotic field or its constituents can be added. The approximation takes the form:

$$\mathbf{u}_\alpha^h(x) = \mathbf{P}^T(x)\mathbf{a}_\alpha(x) + \sum_{j=1}^{n_c} k_1^j Q_{1\alpha}^j(x) + k_2^j Q_{2\alpha}^j(x) \quad (4.37)$$

where $\mathbf{u}_\alpha^h(x)$ denotes the approximation for $\mathbf{u}_\alpha(x)$, $\mathbf{P}(x)$ is the standard polynomial basis defined earlier, n_c is the number of cracks in the model, $\mathbf{a}_\alpha(x)$ are the coefficients of the polynomial basis; k_1^j and k_2^j are global unknowns associated with crack. Lower case Greek subscripts have a range of 2 and refer to Cartesian components.

The functions $Q_{1\alpha}(x)$ and $Q_{2\alpha}(x)$, which describe the near-tip displacement field,

are

$$Q_{11}(x) = \frac{1}{2\mu} \sqrt{\frac{r}{2\pi}} \cos\left(\frac{\theta}{2}\right) [k - 1 + 2\sin^2\left(\frac{\theta}{2}\right)] \quad (4.38)$$

$$Q_{12}(x) = \frac{1}{2\mu} \sqrt{\frac{r}{2\pi}} \sin\left(\frac{\theta}{2}\right) [k + 1 - 2\cos^2\left(\frac{\theta}{2}\right)] \quad (4.39)$$

$$Q_{21}(x) = \frac{1}{2\mu} \sqrt{\frac{r}{2\pi}} \sin\left(\frac{\theta}{2}\right) [k + 1 + 2\cos^2\left(\frac{\theta}{2}\right)] \quad (4.40)$$

$$Q_{22}(x) = \frac{1}{2\mu} \sqrt{\frac{r}{2\pi}} \cos\left(\frac{\theta}{2}\right) [k - 1 - 2\sin^2\left(\frac{\theta}{2}\right)] \quad (4.41)$$

The coefficients $\mathbf{a}_\alpha(x)$, are functions of the spatial coordinates and are determined by the MLS methodology. However, additional terms arise from the inclusion of the near-tip field and so the MLS formulation will be again derived here in the interest of completeness. A weighted, discrete L_2 norm is written

$$L = \sum_{I=1}^n w(\mathbf{x} - \mathbf{x}_I) [\mathbf{p}^T(\mathbf{x}_I) \mathbf{a}_\alpha(\mathbf{x}) + \sum_{j=1}^n [k_1^j Q_{1\alpha}^j(\mathbf{x}_I) + k_2^j Q_{2\alpha}^j(\mathbf{x}_I)] - u_{I\alpha}]^2 \quad (4.42)$$

where, n is the number of points in the neighborhood of \mathbf{x} for which the weight function $w(\mathbf{x} - \mathbf{x}_I)$ is non-zero, and $u_{I\alpha}$ is the component of the nodal value at \mathbf{x}_I . The stationarity of L with respect to $\mathbf{a}_\alpha(\mathbf{x})$ leads to

$$\mathbf{A}(\mathbf{x}) \mathbf{a}_\alpha(\mathbf{x}) = \sum_{I=1}^n \mathbf{C}_I(\mathbf{x}) \left\{ u_{I\alpha} - \sum_{j=1}^n [k_1^j Q_{1\alpha}^j(\mathbf{x}_I) + k_2^j Q_{2\alpha}^j(\mathbf{x}_I)] \right\} \quad (4.43)$$

where,

$$\mathbf{A}(\mathbf{x}) = \sum_{I=1}^n w(\mathbf{x} - \mathbf{x}_I) \mathbf{P}(\mathbf{x}_I) \mathbf{P}^T(\mathbf{x}_I) \quad (4.44)$$

$$\mathbf{C}_I(\mathbf{x}) = w(\mathbf{x} - \mathbf{x}_I) \mathbf{P}(\mathbf{x}_I) \quad (4.45)$$

It should be noted that k_1^j and k_2^j are global parameters in this technique and they are considered fixed in the process of obtaining the parameters \mathbf{a}_α for the local fit. Solving Eq. (4.43) for $\mathbf{a}(\mathbf{x})$ gives

$$\mathbf{a}_\alpha(\mathbf{x}) = \sum_{I=1}^n \mathbf{A}^{-1}(\mathbf{x}) \mathbf{C}_I(\mathbf{x}) \left\{ u_{I\alpha} - \sum_{j=1}^{n_c} [k_1^j Q_{1\alpha}^j(\mathbf{x}_I) + k_2^j Q_{2\alpha}^j(\mathbf{x}_I)] \right\} \quad (4.46)$$

Expressing in terms of the nodal parameter $u_{I\alpha}$ and the enriched field parameters k_1^j and k_2^j yields

$$\mathbf{u}_\alpha^h(\mathbf{x}) = \sum_{I=1}^n \Phi_I(\mathbf{x}) \left\{ u_{I\alpha} - \sum_{j=1}^{n_c} [k_1^j Q_{1\alpha}^j(\mathbf{x}_I) + k_2^j Q_{2\alpha}^j(\mathbf{x}_I)] \right\} + \sum_{j=1}^{n_c} [k_1^j Q_{1\alpha}^j(\mathbf{x}) + k_2^j Q_{2\alpha}^j(\mathbf{x})] \quad (4.47)$$

$$\mathbf{u}_\alpha^h(\mathbf{x}) = \sum_{I=1}^n \Phi_I(\mathbf{x}) u_{I\alpha} + \sum_{j=1}^{n_c} k_1^j \left[Q_{1\alpha}^j(\mathbf{x}) - \sum_{I=1}^n \Phi_I(\mathbf{x}) Q_{1\alpha}^j(\mathbf{x}_I) \right] + \sum_{j=1}^{n_c} k_2^j \left[Q_{2\alpha}^j(\mathbf{x}) - \sum_{I=1}^n \Phi_I(\mathbf{x}) Q_{2\alpha}^j(\mathbf{x}_I) \right] \quad (4.48)$$

where, the shape function, $\Phi_I(\mathbf{x})$, is defined as

$$\Phi_I(\mathbf{x}) = \mathbf{P}^T(\mathbf{x}) \mathbf{A}^{-1}(\mathbf{x}) \mathbf{C}_I(\mathbf{x}) \quad (4.49)$$

These shape functions are capable of representing the smooth part of the solution. Eq. (4.48) will be written as

$$\mathbf{u}_\alpha^h(\mathbf{x}) = \sum_{I=1}^n \Phi_I(\mathbf{x}) \tilde{u}_{I\alpha} + \sum_{j=1}^{n_c} [k_1^j Q_{1\alpha}^j(\mathbf{x}) + k_2^j Q_{2\alpha}^j(\mathbf{x})] \quad (4.50)$$

where, the modified nodal coefficients, $\tilde{u}_{I\alpha}$, are

$$\tilde{u}_{I\alpha} = u_{I\alpha} - \sum_{j=1}^{n_c} [k_1^j Q_{1\alpha}^j(\mathbf{x}_I) + k_2^j Q_{2\alpha}^j(\mathbf{x}_I)] \quad (4.51)$$

4.1.2.2.1.2 Extrinsic PU Enrichment

Extrinsic enrichment of meshfree methods can be carried out using partition of unity (PU) techniques. In this technique, the approximation is augmented by enrichment functions added extrinsically to the existing EFGM approximation. This basis can consist of higher order polynomials or, for linear elastic fracture problems, terms from the asymptotic near tip field can be used. The extrinsic basis is smoothly added to the existing approximation by multiplying it by a partition of unity.

The essential element of this technique is the construction of a partition of unity, which can be obtained by the MLS methodology. A partition of unity $\Phi_I(\mathbf{x})^k$,

constructed from a complete polynomial basis of order k , is a local approximation for which

$$\sum_{I=1}^n \Phi_I(x) = 1 \quad (4.52)$$

It can easily be seen that MLS approximations are partitions of unity since Eq. (4.52) has the reproducing condition for a constant, which MLS approximations must satisfy. Approximations based on partitions of unity take the form

$$u^h(x) = \sum_{I=1}^n \Phi_I^k(x) u_I + \sum_{I=1}^n \sum_{i=1}^{m_e} \Phi_I^0(x) b_{ii} q_i(x) \quad (4.53)$$

where, u_I and b_{ii} are nodal coefficients, and n is the number of neighbors of point x . The vector $q(x)$ is called the extrinsic basis and is of length m_e . For enriching linear elastic fracture problems, this basis can contain the \sqrt{r} radial dependence or the \sqrt{r} radial and angular θ dependence. A superscript k is added to the shape functions Φ_I in the approximation to denote the polynomial order of the basis used in forming the partition of unity.

PU technique appears to provide a vehicle for local enrichment. The partition of unity, $\Phi_I(x)^k$, can be formed from a linear basis ($k = 2$), which yields linear consistency. Enrichment of the approximation may be carried out locally by adding the known form of the solution to the extrinsic basis $q(x)$, at nodes in the region in which it is needed. It should be noted that the enrichment should be added to each node whose domain of influence extends into the region to be enriched.

The concept of PUM enrichment strategy for meshless methods used is given below [52]

$$\mathbf{u}^h(x) = \sum_{I \in N} \Phi_I(x) \mathbf{u}_I + \sum_{J \in N^c} \Phi_J(x) H(x) a_J + \sum_{K \in N'} \Phi_K(x) \sum_{\alpha=1}^4 \mathbf{b}_K^\alpha c_{\alpha K} \quad (4.54)$$

where, $\Phi_I(x)$ are MLS shape functions. The Heaviside function and the branch functions are given by

$$H(\mathbf{x}) = \begin{cases} +1 & \text{if } (\mathbf{x} - \mathbf{x}^*) \cdot \mathbf{n} \geq 0 \\ -1 & \text{otherwise} \end{cases} \quad (4.55)$$

$$\mathbf{B} = [B_1, B_2, B_3, B_4] = \left[\sqrt{r} \sin \frac{\theta}{2}, \sqrt{r} \cos \frac{\theta}{2}, \sqrt{r} \sin \frac{\theta}{2} \cos \theta, \sqrt{r} \cos \frac{\theta}{2} \cos \theta \right] \quad (4.56)$$

where, r and θ are polar coordinates in the local crack front coordinate system. The set N^c includes the nodes whose support contains point x and cut by the crack, see Fig.4.7, whereas the set N^f are nodes whose support contains point x and the crack tip x_{tip} , see Fig.4.8.

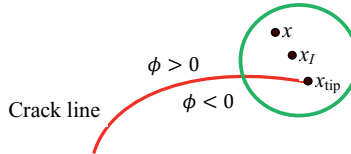


Fig.4.7 Elements of set N^c are nodes whose support contains point x and cut by the crack.

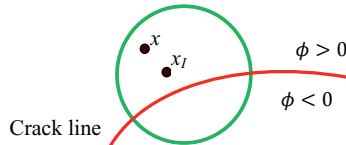


Fig.4.8 Elements of set N^f are nodes whose support contains point x and the crack tip x_{tip} .

Using the Galerkin procedure as described in previous sections, the usual discrete equations are obtained with only one difference in the B matrix which now becomes extended

$$\mathbf{B} = [\mathbf{B}^{fem} | \mathbf{B}^{enr}] \quad (4.57)$$

where \mathbf{B}^{fem} is the standard B matrix in two dimensions

$$\mathbf{B}_I^{fem} = \begin{bmatrix} \Phi_{I,x} & 0 \\ 0 & \Phi_{I,y} \\ \Phi_{I,y} & \Phi_{I,x} \end{bmatrix} \text{ and } \mathbf{B}^{enr} \text{ is the enriched } B \text{ matrix}$$

$$\mathbf{B}_I^{enr} = \begin{bmatrix} (\Phi_I)_{,x} \Psi_I + \Phi_I (\Psi_I)_{,x} & 0 \\ 0 & (\Phi_I)_{,y} \Psi_I + \Phi_I (\Psi_I)_{,y} \\ (\Phi_I)_{,y} \Psi_I + \Phi_I (\Psi_I)_{,y} & (\Phi_I)_{,x} \Psi_I + \Phi_I (\Psi_I)_{,x} \end{bmatrix} \quad (4.58)$$

where, $\Phi_I(\mathbf{x})$ can be either the Heaviside function $H(\mathbf{x})$, either the branch functions $B_\alpha(\mathbf{x})$

4.1.2.3 Intrinsic Enrichment

Meshless approximations can be intrinsically enriched by including a special function in the basis. For example, in fracture mechanics, one can include the asymptotic near-tip displacement field, or an important ingredient such as \sqrt{r} . The choice of functions depends on the coarse mesh accuracy desired. For higher accuracy, include the full asymptotic field, while for higher speed at some cost of accuracy, only the \sqrt{r} function can be included in the basis.

4.1.2.3.1 Full Enrichment

In full intrinsic enrichment of EFG approximations for fracture problems, the entire near-tip asymptotic displacement field is included in the basis. Following some trigonometric manipulation, it can be shown that all the functions in Eq.(2.8) are spanned by the basis

$$\mathbf{P}^T(\mathbf{x}) = \left[1, x, y, \sqrt{r} \cos \frac{\theta}{2}, \sqrt{r} \sin \frac{\theta}{2}, \sqrt{r} \sin \frac{\theta}{2} \sin \theta, \sqrt{r} \cos \frac{\theta}{2} \sin \theta \right] \quad (4.59)$$

(The linear terms are not related to the near-tip fields and are represented through the linear completeness of the EFG approximant). This basis leads the approximations of the form

$$u^h(\mathbf{x}) = \sum_{I=1}^n \underbrace{\mathbf{P}^T(\mathbf{x}) \mathbf{A}^{-1}(\mathbf{x}) \mathbf{C}_I(\mathbf{x})}_{\Phi_I(\mathbf{x})} u_I \quad (4.60)$$

where, $\Phi_I(\mathbf{x})$ is enriched EFGM shape function.

In contrast to the extrinsic techniques, this technique involves no additional unknowns. However, because of the increased size of the basis, an additional computational effort is required to invert the moment matrix $A(\mathbf{x})$. For multiple

cracks, four additional terms would have to be added to the basis for each crack.

4.1.2.3.2 Modifications In Intrinsic Enrichment Criterion

In case of a single crack, the enrichment is done for each evaluation/Gauss point of the domain, which consists of the additional terms related with the only crack present in the domain but in case of multiple cracks, enrichment decision with respect to a particular crack tip is made based on the minimum normalized distance between the evaluation/Gauss point and crack tips. According to this modification, the distances of an evaluation point from all the crack tips are evaluated and normalized by their corresponding crack lengths, and then the enrichment is decided on the basis of the minimum normalized distance [71].

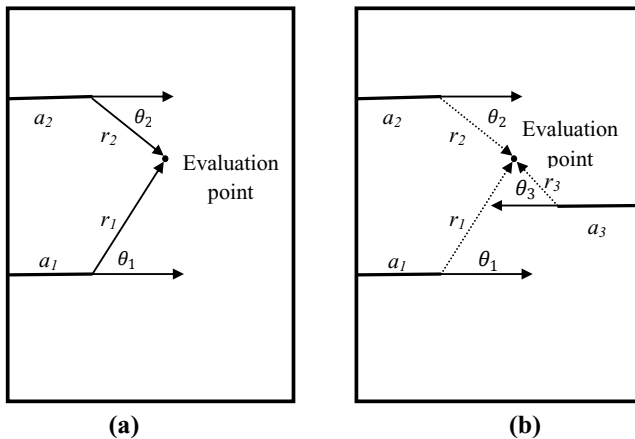


Fig.4.9 Multiple edge cracks: An evaluation point and crack tip parameters are shown

For example, two parallel cracks of length a_1 and a_2 are taken as shown in Fig.4.9a; the location of a particular evaluation/Gauss point with respect to different crack tips are (r_i, θ_i) and (r_2, θ_2) , respectively. Now at a particular evaluation point during numerical integration over the domain, the decision of enrichment needs to be made based on the normalized distances of each crack tip from the evaluation point i.e. r_i/a_i with $i = 1, 2$. This criterion works well to study and analyze the interaction effect of similar size cracks [71], but can't handle unequal size cracks

properly. Therefore, this intrinsic enriched criterion requires further improvement for the study of both equal and unequal size multiple cracks.

4.1.2.3.2.1 Intrinsic Enrichment Criterion For Multiple Cracks Of Unequal Crack Lengths

It is quite difficult to handle unequal size multiple cracks and their interactions by criterion explained in the previous section, therefore, in this section, modification of above explained intrinsic enrichment criterion to handle multiple cracks of unequal lengths [15] is elaborated. This criterion is also based on the normalized distances of an evaluation/Gauss points from the crack tips. According to this criterion, the distances of an evaluation point from all crack tips are evaluated and normalized by their corresponding crack lengths. The contributions of various cracks tips present in the domain are decided based on their normalized distances from the crack tips. In this criterion, all cracks contribute to the stiffness matrix (K_{IJ}) at each evaluation point, whereas in previous criterion, only one crack contributes to K_{IJ} at each evaluation point. For example, three cracks of length a_1 , a_2 , and a_3 are taken as shown in Fig.4.9b, and the location of a particular evaluation/ Gauss point with respect to various crack tips are (r_1, θ_1) , (r_2, θ_2) , and (r_3, θ_3) respectively. Now, during numerical integration at a particular evaluation/ Gauss point, the enriched basis and shape functions are constructed separately using Eq.(4.59) for each crack tip. Once the shape functions are obtained using enriched basis for each crack tip at an evaluation point, then the contribution of each crack tip to the stiffness matrix is decided on the basis of the normalized distances i.e. $d_i = r_i / a_i$ with $i = 1, 2, 3$. Mathematically, K_{IJ} at an evaluation/Gauss point in Eq.(3.13a) is evaluated as

$$[K_{IJ}]_{total} = [K_{IJ}]_1 \times R_1 + [K_{IJ}]_2 \times R_2 + \dots + [K_{IJ}]_N \times R_N \quad (4.61)$$

where, N denotes the number of cracks present in the domain, R_i is a parameter which decides the contribution of a particular crack, and $[K_{IJ}]_i$ is evaluated by Eq.(3.13a) as $[K_{IJ}]_i = \int_{\Omega} B_i^T D B_i Dd\Omega$ with a different \mathbf{B}_i for each crack. The value of R_i in Eq.(4.61) is numerically evaluated as:

$$R_i = \frac{S_i}{\sum_{j=1}^N S_j} \text{ with } \sum_{i=1}^N R_i = 1 \quad (4.62)$$

where, $S_i = d_i^C$ and d_i represent normalized crack tip distance ($d_i = r_i / a_i$) for a particular crack and C is a predefined constant, which is calculated by performing the sensitivity analysis of C , and its acceptable range is found to be $-50 < C < -100$ [15].

4.1.2.3.2.2 Partial Domain Intrinsic Enrichment Criterion

For cracks in non-convex domains full domain enrichment provides misleading results because during numerical integration the effect of enrichment with respect to particular crack tip is influenced by all the Gauss points lying in the domain irrespective of their locations. In partial domain enrichment (PDE) [76] two concentric circles can be defined around the crack tip as shown in Fig.4.10. Now the level of enrichment is decided by the location of evaluation point within these circles. Fig.4.10 represents a generalized problem domain with an edge crack of length a . The radius of smaller circle is equal to crack length and radius of larger circle is $c \times a$. As stated by Singh I.V. et. al [76] the value of c should be greater than 1. The three different region obtained namely A , B and C decide the location of the evaluation point and the following criterion is followed. For all the points lying in the inner most region A full enrichment is used and for all the points lying in region C no enrichment is used and standard linear basis is followed. If the evaluation point exists in region B both linear and standard basis will be used and their contributions to stiffness matrix will be decided by the following formularization:

$$[K]_{total} = [K]_{Enriched\ basis} \times R + [K]_{Linear/Standard\ basis} \times (I-R) \quad (4.63)$$

where R is a parameter that decides the contribution of each component to final stiffness matrix.

$$R = \frac{c \times a - r_g}{(c-1) \times a} \quad (4.64)$$

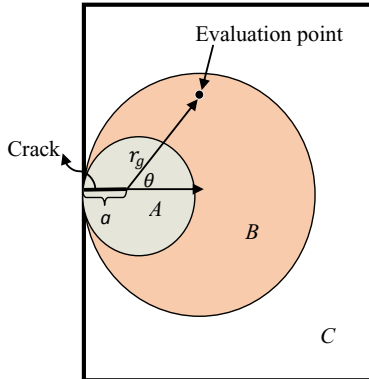


Fig.4.10 Partial domain enrichment criterion

c here is a constant that decides the size of region B , a is crack length and r_g is distance of evaluation point from crack tip.

4.1.2.4 Orthotropic Enrichment Functions

Orthotropic medium is different from isotropic medium hence orthotropic enrichment functions used in extended finite element method [77] were adopted for fracture analysis via EFGM [78].

The stress-strain law in an arbitrary linear elastic material can be written as

$$\varepsilon = c\sigma \quad (4.65)$$

where ε and σ are strain and stress vectors, respectively, and c is the compliance matrix, defined in 3D as:

$$c^{3D} = \begin{bmatrix} 1 & -v_{21} & -v_{31} & 0 & 0 & 0 \\ \frac{-v_{12}}{E_1} & \frac{1}{E_2} & \frac{-v_{32}}{E_3} & 0 & 0 & 0 \\ \frac{-v_{13}}{E_1} & \frac{-v_{23}}{E_2} & \frac{-v_{31}}{E_3} & 0 & 0 & 0 \\ 0 & 0 & 0 & \frac{1}{G_{23}} & \frac{1}{G_{13}} & \frac{1}{G_{12}} \\ 0 & 0 & 0 & 0 & \frac{1}{G_{13}} & 0 \\ 0 & 0 & 0 & 0 & 0 & \frac{1}{G_{12}} \end{bmatrix} \quad (4.66)$$

where E, v and G are Young's modulus, Poisson's ratio and shear modulus, respectively. For a plane stress case the compliance matrix is simplified into the following form:

$$c_{ij}^{2D} = c_{ij}^{3D} \quad i, j = 1, 2, 6 \quad (4.67)$$

and for a plane strain state

$$c_{ij}^{2D} = c_{ij}^{3D} - \frac{c_{i3}^{3D} \cdot c_{j3}^{3D}}{c_{33}^{3D}} \quad i, j = 1, 2, 6 \quad (4.68)$$

Now assume an anisotropic body subjected to arbitrary forces with general boundary conditions and a crack. global Cartesian coordinate (X, Y) , local Cartesian coordinate (x, y) , and local polar coordinate (r, θ) defined on the crack tip are illustrated in Fig.4.11. A fourth-order partial differential equation with the following characteristic equation can be obtained using equilibrium and compatibility conditions [78]

$$c_{ij}^{2D} s^4 - 2c_{16}^{2D} s^3 + (2c_{12}^{2D} + c_{66}^{2D}) s^2 - 2c_{12}^{2D} s + c_{22}^{2D} = 0 \quad (4.69)$$

Lekhnitskii[79] proved that the roots of Eq.(4.69) are always complex or purely imaginary ($s_k = s_{kx} + is_{ky}, k = 1, 2$) and occur in conjugate pairs as s_1, \bar{s}_1 and s_2, \bar{s}_2 . Accordingly, the two-dimensional displacement and stress fields in the vicinity of the crack tip are

Mode I:

$$u^1 = K_I \sqrt{\frac{2r}{\pi}} \operatorname{Re} \left[\frac{1}{s_1 - s_2} (s_1 p_2 \sqrt{\cos\theta + s_1 \sin\theta} - s_2 p_1 \sqrt{\cos\theta + s_1 \sin\theta}) \right] \quad (4.70)$$

$$v^1 = K_I \sqrt{\frac{2r}{\pi}} \operatorname{Re} \left[\frac{1}{s_1 - s_2} (s_1 q_2 \sqrt{\cos\theta + s_1 \sin\theta} - s_2 q_1 \sqrt{\cos\theta + s_1 \sin\theta}) \right] \quad (4.71)$$

$$\sigma_{xx}^I = \frac{K_I}{\sqrt{2\pi r}} \operatorname{Re} \left[\frac{s_1 s_2}{s_1 - s_2} \left(\frac{s_2}{\sqrt{\cos\theta + s_2 \sin\theta}} - \frac{s_1}{\sqrt{\cos\theta + s_1 \sin\theta}} \right) \right] \quad (4.72a)$$

$$\sigma_{yy}^I = \frac{K_I}{\sqrt{2\pi r}} \operatorname{Re} \left[\frac{1}{s_1 - s_2} \left(\frac{s_1}{\sqrt{\cos\theta + s_2 \sin\theta}} - \frac{s_2}{\sqrt{\cos\theta + s_1 \sin\theta}} \right) \right] \quad (4.72b)$$

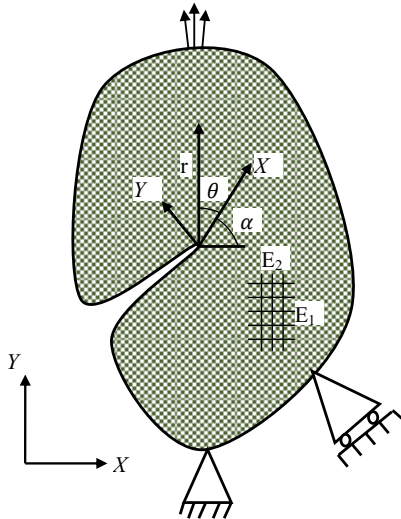


Fig.4.11 An arbitrary cracked orthotropic body

$$\sigma_{xy}^I = \frac{K_I}{\sqrt{2\pi r}} \operatorname{Re} \left[\frac{s_1 s_2}{s_1 - s_2} \left(\frac{1}{\sqrt{\cos\theta + s_1 \sin\theta}} - \frac{1}{\sqrt{\cos\theta + s_2 \sin\theta}} \right) \right] \quad (4.72c)$$

Mode II:

$$u^{II} = K_{II} \sqrt{\frac{2r}{\pi}} \operatorname{Re} \left[\frac{1}{s_1 - s_2} (p_2 \sqrt{\cos\theta + s_1 \sin\theta} - p_1 \sqrt{\cos\theta + s_1 \sin\theta}) \right] \quad (4.73)$$

$$v^{II} = K_{II} \sqrt{\frac{2r}{\pi}} \operatorname{Re} \left[\frac{1}{s_1 - s_2} (q_2 \sqrt{\cos\theta + s_1 \sin\theta} - q_1 \sqrt{\cos\theta + s_1 \sin\theta}) \right] \quad (4.74)$$

$$\sigma_{xx}^{II} = \frac{K_{II}}{\sqrt{2\pi r}} \operatorname{Re} \left[\frac{1}{s_1 - s_2} \left(\frac{s_2^2}{\sqrt{\cos\theta + s_2 \sin\theta}} - \frac{s_1^2}{\sqrt{\cos\theta + s_1 \sin\theta}} \right) \right] \quad (4.75a)$$

$$\sigma_{yy}^{II} = \frac{K_{II}}{\sqrt{2\pi r}} \operatorname{Re} \left[\frac{1}{s_1 - s_2} \left(\frac{1}{\sqrt{\cos\theta + s_2 \sin\theta}} - \frac{1}{\sqrt{\cos\theta + s_1 \sin\theta}} \right) \right] \quad (4.75b)$$

$$\sigma_{xy}^{II} = \frac{K_{II}}{\sqrt{2\pi r}} \operatorname{Re} \left[\frac{1}{s_1 - s_2} \left(\frac{s_1}{\sqrt{\cos\theta + s_1 \sin\theta}} - \frac{s_2}{\sqrt{\cos\theta + s_2 \sin\theta}} \right) \right] \quad (4.75c)$$

where Re denotes the real part of the statement and K_I and K_{II} are stress intensity factors for mode I and mode II, respectively. p_i and q_j are defined as

$$p_i = c_{11}s_i^2 + c_{12} - c_{16}s_i \quad i=1,2 \quad (4.76)$$

$$q_i = c_{12}s_i + \frac{c_{22}}{s_i} - c_{26} \quad i = 1,2 \quad (4.77)$$

4.1.2.4.1 Orthotropic Enrichment

Crack-tip enrichment functions have been obtained in a way that include all possible displacement states in the vicinity of crack tip mentioned in Eqs.(4.70,4.71) and Eqs.(4.73,4.74) [77]. These functions span the possible displacement space that may occur in the analytical solution. The enrichment functions were used as given in [77] are:

$$\begin{aligned} Q(r, \theta) &= [Q_1, Q_2, Q_3, Q_4] \\ &= [\sqrt{r}\cos\frac{\theta_1}{2}\sqrt{g_1(\theta)}, \sqrt{r}\cos\frac{\theta_2}{2}\sqrt{g_2(\theta)}, \sqrt{r}\sin\frac{\theta_1}{2}\sqrt{g_1(\theta)}, \sqrt{r}\sin\frac{\theta_2}{2}\sqrt{g_2(\theta)}] \end{aligned} \quad (4.78)$$

where

$$\theta_j = \arctan\left(\frac{s_{jy}\sin\theta}{\cos\theta + s_{jx}\sin\theta}\right) \quad (4.79)$$

$$g_j(\theta) = \sqrt{(\cos\theta + s_{jx}\sin\theta)^2 + (s_{jy}\sin\theta)^2} \quad (4.80)$$

with $j=1,2$. In the above equations s_{jx} and s_{jy} are real and imaginary parts of characteristics roots s_j , respectively.

All crack tip enrichment functions include the \sqrt{r} term, leading to the appearance of $1/\sqrt{r}$ in all spatial derivatives, as a result, strain and stress components become singular when r approaches zero. The existence of such a singular stress field should be cautiously considered in any integration and post-processing procedures such as evaluation of the J-integral which will be discussed in later chapter.

4.1.2.5 Modeling of Kinked Cracks

In intrinsic enriched EFGM, functions from the near-tip asymptotic displacement fields are included in the basis for the simulation of fracture mechanics problems [50,71]. An enriched basis defined earlier in Eq.4.59:

where, r denote the distance of an evaluation point from the crack tip, and θ is the angle measured in local coordinate system as shown in Fig.4.12.

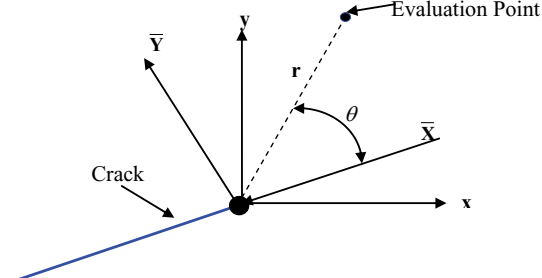


Fig.4.12: Local coordinate system (\bar{x}, \bar{y}) at crack

However, the basis function given by Eq. (4.59) predicts a discontinuity only along $\theta = \pm\pi$ from the crack line. For a kink crack modeling, suitable mapping is required to align the field discontinuity with actual crack segments. The criterion elaborated in this section for modeling a kinked crack is based on the modification in angular position of an evaluation point/node [80]. The angular position of an evaluation point/node is modified in such a way that all points in the vicinity of the crack segments approximate the discontinuity along $\theta = \pm\pi$. Fig.4.13 shows a kinked crack with segments AB and BC . The local coordinate system is aligned along the leading segment i.e. BC with the origin at the tip. Consider an evaluation point P located in the vicinity of crack. Let, the angular orientation of point P be α . In order to represent the discontinuity along the crack line, the angular orientation α should be mapped to a new coordinate system such that $\alpha \rightarrow \pm\pi$. The angular orientation of all the evaluation points is mapped to a new coordinate system in such a way that the evaluation points lying near the crack line exhibit a discontinuity in displacement fields.

The first step involved in the process of angular mapping is the division of domain into different regions. Fig.4.13-4.14 shows a kinked crack having segments AB , BC where C is the crack tip of the leading crack segment. A local coordinate system is fixed at the tip of leading crack. Normals are drawn at a common point to both crack segments, i.e. point B , so as to discretize the region above the crack. Thus, BQ and BP become normal to crack segments AB and BC respectively. Another normal is drawn at the tip of leading crack BC . The bisector of angle ABC is drawn

so that the region below the crack gets divided into two parts. In this way, the entire region near the crack segments is divided into six different regions. For a crack with multiple kinks, a similar procedure is employed for domain division. Finally, a suitable mathematical mapping (for angular orientation) is applied depending upon the spatial location of an evaluation point.

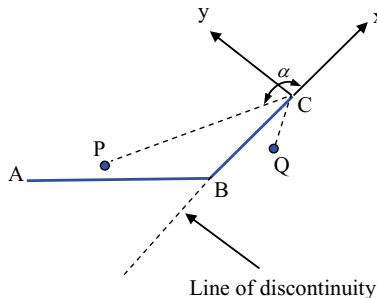


Fig.4.13 Mapping scheme for kinked crack

For the region in front of the tip of leading crack i.e. region 1, all the angular measurements are made with respect to local coordinate axis in such a way that

$$\theta' = \theta \quad \text{for } -\frac{\pi}{2} \leq \theta \leq \frac{\pi}{2}. \quad (4.81)$$

For regions 2,3,4,5 the angular location of an evaluation point is modified as given below:

$$\theta' = \begin{cases} \pi - \sin^{-1}\left(\frac{h'}{r}\right) & \text{above the crack} \\ -\pi + \sin^{-1}\left(\frac{h'}{r}\right) & \text{below the crack} \end{cases} \quad (4.82)$$

where, h' is the normal distance between the evaluation point/node and the crack segment lying in that region, r is the distance between an evaluation point and the tip of leading crack i.e. point C .

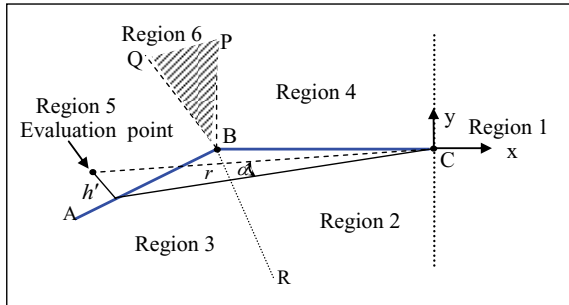


Fig.4.14 Domain description for modeling kinked crack

For the points lying in shaded region QBP , the distance h' is measured between an evaluation point and the point representing kink i.e. point B . In doing so, a transformation obtained such that as the valuation point approaches to the crack line, $h' \rightarrow 0$ then $\theta' \rightarrow \pm\pi$, and thus the required discontinuity is obtained along the crack line.

Finally, the standard enriched basis function is written in terms of modified angle θ' as follows

$$\mathbf{P}^T(\mathbf{x}) = \begin{bmatrix} 1, \underbrace{x, y}_{\text{standard basis}}, \underbrace{\sqrt{r} \cos \frac{\theta'}{2}, \sqrt{r} \sin \frac{\theta'}{2}, \sqrt{r} \sin \frac{\theta'}{2} \sin \theta', \sqrt{r} \cos \frac{\theta'}{2} \sin \theta'}_{\text{enrichment terms}} \end{bmatrix} \quad (4.83)$$

where, the first three terms represent the standard basis function $(1, x, y)$ while remaining four terms make the enrichment part for a kinked crack.

4.2 Conclusion

In dealing with weak discontinuities the following points are worth mentioning:

- Domain partitioning approach produced very accurate displacement results however oscillations about the exact solution were inherent while taking derivatives of displacement.

- Jump function approach for representation of discontinuity is particularly effective at crack tips. The method can be easily extended for branching and intersecting cracks.
- On comparing various techniques it is found that jump function approach gives best results for both vertical and horizontal interface problems.

In dealing with strong discontinuities the following points are worth mentioning:

- In smoothing techniques visibility criterion is best for cracks and see through technique is best for hole.
- Extrinsic enrichment can be used for multiple cracks with little expense.
- Intrinsic enrichment is easy to program.
- Both methods (Extrinsic and Intrinsic enrichment) offer significant reduction in number of unknowns required to obtain accurate solution by meshless method.
- Intrinsic enrichment provides better results for studying crack problems with comparison to extrinsic enrichment.
- Two types of EWFs are constructed in the works of Namakian et al. [81] one fully enriched and other partially enriched and their prowess is tested in many cases and these enriched functions provide high workability than standard extrinsic enrichment techniques.

CHAPTER 5

MODIFICATION IN EFGM

5.1 Coupled Techniques

The coupling of EFGM with other methods [30,44,46,82–85] is done to avoid engineering effort and save computational time. The various coupled techniques provide the advantages of two techniques in one method thereby optimizing the analysis in terms of speed and accuracy.

5.1.1 Coupled Finite Element And Element Free Galerkin Method (FE-EFG)

For analysis and modeling of crack in a complicated engineering structures, it is efficient to use EFG approximations around the crack tip region but rely on the comprehensive capabilities of a finite element software package in the remainder of the domain. This coupling of FEM and EFGM [42,86–90] is achieved by the use of interface elements between FE and EFGM nodes. The approximation in transition is given as:

$$u^h(x) = \sum_{I=1}^N \bar{\phi}_I(x) u_I \quad (5.1)$$

where $\bar{\phi}_I(x)$ are the shape functions and $u(x)$ is the displacement component of node I. The complete domain Ω is sub-divided into three domains (Ω^{FE}), (Ω^{EFGM}) and transition sub-domain (Ω^{TE}) as shown in Fig.5.1. Henceforth, the shape function depends upon the location of point x in the domain.

Case 1. If $x \in \Omega^{FE}$

The interpolation function of displacement u for an iso-parametric element is given by [91]

$$u^{FE}(x) = \sum_{I=1}^{n_e} N_I u_I \quad (5.2)$$

where n_e is the number of nodes in the element.

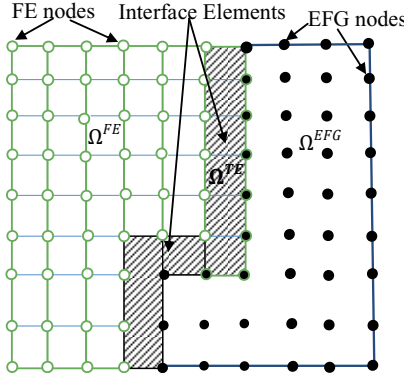


Fig.5.1 Schematic representation of FE-EFG

Case 2. If $x \in \Omega^{EFGM}$.

As it is already well known that for EFGM moving least square approximations are used, hence from Eq.(2.25)

$$u^{EFGM}(\mathbf{x}) = \sum_{I=1}^n \Phi_I(\mathbf{x}) u_I = \Phi^T(\mathbf{x}) \mathbf{u} \quad (5.3)$$

where,

$$\Phi^T(\mathbf{x}) = \{\Phi_1(\mathbf{x}), \Phi_2(\mathbf{x}), \Phi_3(\mathbf{x}), \dots, \Phi_n(\mathbf{x})\} \quad (5.4)$$

$$\mathbf{u}_I = [u_1, u_2, u_3, \dots, u_n] \quad (5.5)$$

The meshfree shape function $\Phi_I(\mathbf{x})$ is defined as:

$$\Phi_I(\mathbf{x}) = \sum_{j=1}^m p_j(\mathbf{x}) (\mathbf{A}^{-1}(\mathbf{x}) \mathbf{B}(\mathbf{x}))_{ji} = \mathbf{p}^T \mathbf{A}^{-1} \mathbf{B}_I \quad (5.6)$$

Case 3. If $x \in \Omega^{TE}$

In order to determine the consistency in transition region the approximate displacement is denoted by:

$$u^h(x) = u^{FE}(x) + R(x)[u^{EFGM}(x) - u^{FE}(x)] \quad (5.7)$$

where u^{FE} and u^{EFGM} are finite element and element free Galerkin approximations respectively. $R(x)$ is a ramp function defined by [42] for coupling interface elements. The ramp function is equal to the sum of the FE shape functions associated with the transition element nodes on the EFG boundary. It varies linearly, to ensure the continuity along transition element boundaries adjacent to other transition elements.

$$R(x) = \sum_I N_I(x), x_I \in \Omega^{EFG} \quad (5.8)$$

The transition element shape functions can be obtained by substituting the FE and EFG displacement approximations Eqs.(5.2)-(5.3) respectively into Eq.(5.7),

$$u^h(x) = \sum_{I=1}^{n_e} \bar{N}_I(x) u_I \quad (5.9)$$

where the transition element shape functions $\bar{N}_I(x)$ can be defined as,

$$\bar{N}_I(x) = [1 - R(x)]N_I(x) + R(x)\Phi_I(x) \quad (5.10)$$

The derivatives of transition shape function are given by

$$\bar{N}_{I,x} = -R_x N_I + [1 - R]N_I(x) + R_{,x}\Phi_I + R\Phi_{I,x} \quad (5.11)$$

Now, the shape function for coupled FE-EFG method can be defined as,

$$\bar{\Phi}_I(x) = \begin{cases} N_I(x), & x \in \Omega^{FE} \\ \Phi_I(x), & x \in \Omega^{EFG} \\ \bar{N}_I(x), & x \in \Omega^{TE} \end{cases} \quad (5.12)$$

5.1.2 Coupled Fractal Finite Element And Element Free Galerkin Method (FFE-EFG)

The coupling of FFEM and EFGM [44] can be achieved by introduction of interface elements in between the domains as shown in Fig.5.2. In these interface elements, a hybrid displacement approximation is defined that satisfies displacement continuity across the interface boundaries. The coupling is employed by use of ramp function similar to described in previous section of coupled FE-EFG approach.

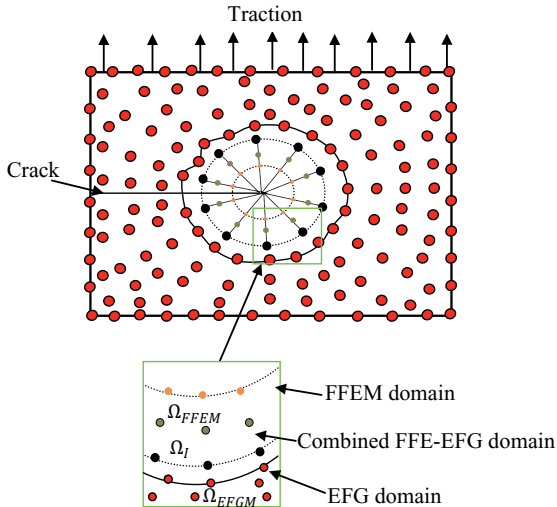


Fig.5.2 Schematic representation of FFE-EFG coupling

5.1.3 Coupled Radial Point Interpolation And Element Free Galerkin Method (EFG-RPIM)

The basic approach involves the evaluation of real value of nodes at the interface between the RPIM and the EFG regions using MLS approximation for EFG and then assign these values to the RPIM nodal set. From preceding sections we know that the MLS shape functions given in Eq.(2.28) do not, in general, satisfy Kronecker delta condition, while the RPIM shape functions given in Eq.(2.74) do. Therefore, there exists the imposition of essential boundary condition problems in EFG methods based on MLS approximation , while the meshfree methods based on the radial basis point interpolation can impose essential boundary conditions as conveniently as in conventional FEM. From previous works [92,93], we also know that the accuracy of RPIM method is less than that of EFG method, and RPIM method is much more time –consuming than EFG method. So, the coupled element-free Galerkin (EFG)-radial point interpolation method(RPIM) can exploit their advantages while avoiding their disadvantages. Fig.5.3 shows a general layout of coupled EFG-RPIM approach.

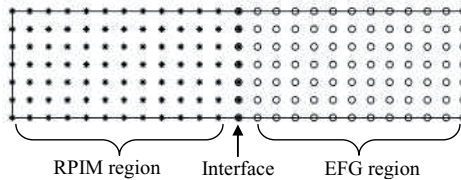


Fig.5.3 Schematic representation of EFG-RPIM coupling

As in coupled FEM-EFG method, the problem domain was divided into two sub-domains in coupled EFG-RPIM method. But coupled EFG-RPIM method can remove the meshes needed in coupled FEM-EFG method. Therefore , coupled EFG-RPIM method is a true meshfree method compared with coupled FEM-EFG method.

5.1.3.1 Discrete Formulations

Both RPIM and EFG use similar forms in approximating displacements adopted in the Galerkin procedure. Using RPIM Eq. (2.73) or MLS Eq. (2.25),we can get

$$u = \begin{Bmatrix} u \\ v \end{Bmatrix} = \sum_{j=1}^n \begin{bmatrix} \phi_j & 0 \\ 0 & \phi_j \end{bmatrix} \begin{Bmatrix} u_j \\ v_j \end{Bmatrix} = \sum_{i=1}^n \Phi_i u_i \quad (5.13)$$

If essential boundary conditions are satisfied at nodes, we need only to use the standard principle of minimum potential energy, i.e., to find $u(x) \in H^l$ such that

$$\Pi = \frac{1}{2} \int_{\Omega} \varepsilon^T D \varepsilon d\Omega - \int_{\Omega} u^T \cdot b d\Omega - \int_{\Gamma_t} u^T \cdot \bar{t} d\Gamma \quad (5.14)$$

is stationary, where H^l denotes the Sobolev space of order i; ε and $\sigma = D\varepsilon$ are strain and stress tensors and D is the strain-stress matrix.

Then substituting Eq.(5.13) into Eq.(5.14) leads to the following total potential energy in the matrix form, as

$$\Pi = \frac{1}{2} u^T \cdot K \cdot u - u^T \cdot f \quad (5.15)$$

and invoking $\delta\Pi = 0$ results in the following linear system of

$$Ku = f \quad (5.16)$$

In which, the stiffness matrix K is built from 2×2 matrices K_{ij} , and the right hand side vector f is built from the 2×1 matrices f_i . These matrices are

$$K_{ij} = \int_{\Omega} B_i^T D B_j d\Omega \quad (i = 1, 2, \dots, n) \quad (5.17)$$

and

$$f_i = \int_{\Omega} \phi_i b d\Omega + \int_{\Gamma_t} \phi_i \bar{t} d\Gamma \quad (i = 1, 2, \dots, n) \quad (5.18)$$

Where

$$B_i = \begin{bmatrix} \phi_{i,x} & 0 \\ 0 & \phi_{i,y} \\ \phi_{i,y} & \phi_{i,x} \end{bmatrix}, \quad D = \frac{E}{1-\nu^2} \begin{bmatrix} 1 & \nu & 0 \\ \nu & 1 & 0 \\ 0 & 0 & \frac{1-\nu}{2} \end{bmatrix} \quad (\text{for plane stress problem})$$

It is worth pointing out that the stiffness matrix K in Eq.(5.17) is symmetric.

5.2 Optimized Element Free Galerkin Method (OEFG)

5.2.1 Modified Algorithm For Calculation Of Size Of Support Domain

In EFGM the radius of the support domain are determined by the following mathematical formula[52]:

$$r_i = d_{max} c_i \quad (5.19)$$

where r_i is the radius of support domain d_{max} is the scaling parameter and c_i is the distance between neighboring nodes. It is well established that the value of scaling parameter is ideal between 1.5-2.5 and the results of simulation are sensitive to it [12]. Therefore, the number of nodes in support domain (n_d) depend on the scaling parameter not on the total amount of nodes (n_T) in the problem geometry. A varying amount of nodes in support domain are introduced using this formulation for every iteration and there occurs a loss in accuracy.

To ensure equal number of nodes in support domain an algorithm is derived based on distances between Gauss points and nodes. The algorithm is implemented during the construction of global stiffness matrix when the loop is iterated for all the Gauss points in the problem geometry. The procedure of the new algorithm employs the following steps:

1. Selection of a desired random number of nodes n_r for each support domain.
2. Calculation of the distance d_α of all the Gauss points G_j ($j = 1 \dots n$) from all the nodes N_i ($i = 1 \dots m$) in the region, given by:

$$d_\alpha = \sqrt{(x_G - X_N)^2 + (y_G - Y_N)^2} \quad (5.20)$$

where x_G, y_G, X_N, Y_N are the coordinates of Gauss points and nodes respectively

3. Sorting the matrix d_α in ascending order and extract the n_{r+1} column.
4. The various values in n_{r+1} column will be the radius of support domain for various Gauss points.

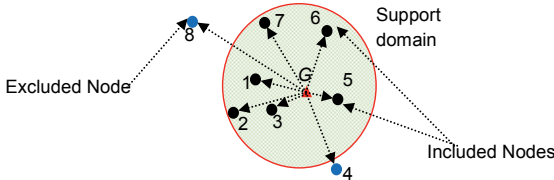


Fig.5.4. Schematic representation of modified algorithm

Fig.5.4 explains the working of the algorithm. The distances (d_α) of all the nodes shown are calculated from a Gauss point G . According to above algorithm if the desired random number of nodes $n_r = 6$ and (d_α) is arranged in ascending order we get $d_5 < d_3 < d_1 < d_6 < d_7 < d_2 < d_4 < d_8$. As only 6 nodes are selected under the support domain (shown by red circle) the sixth largest value of $d_\alpha = d_2$ is selected as radius of domain. Hence, all the nodes at distances greater than d_2 are excluded.

The desired random number of nodes(n_r) should be carefully selected as a low number will generate very flawed results and too high will increase the computational time and increase error. To remove the predicament an optimization is carried out by Taguchi method.

5.2.2 Optimization Of EFGM Parameters

The total nodes in the problem geometry(n_T), order of Gauss quadrature selected and total number of nodes in domain(n_d) influences the integration of the domain,

therefore play a major role in EFG simulation. The above defined algorithm ensures equal number of nodes for each support domain but it does not provide an idea about the optimum number of nodes preferred for efficient calculation of results. Till date no parametric study concerning optimization of these parameters has been presented. To remove this discrepancy an optimization of these EFG parameters considering an edge crack problem is performed. The relative deviation(RD) from previous results is considered as objective function and Taguchi method[94,95] is used. The effect of three parameters/control factors namely (i) total number of nodes in problem geometry (n_T) (ii) Gauss quadrature and (iii) desired random number of nodes in support domain (n_r) on objective function is determined. The optimization is performed with an intent to get a general idea about the parameters best suited for an EFG simulation.

To find the optimized EFGM parameters a rectangular domain with mechanical properties ($E = 1 \times 10^6, \nu = 0.3$) subjected to tensile load is preferred as a model for this study as used by Salari-Rad et al.[96]. The domain's dimensions are height (H) = 2 units and width (W)= 1 units and the applied load is $\sigma_0 = 1$ units under plane stress conditions. The position of crack with crack length $a = 0.4$ units is fixed in all the simulations at co-ordinates $x = 0$ and $y = H/2$, with the crack is parallel to the horizontal axis. The selection criterion of control factors is explained in next paragraph.

Based on previous works by researchers it can be comprehended that an EFGM simulation for similar type of fracture problem(mentioned above) presented[96] can be carried out efficiently by an average of 800-1000 nodes[15,80,96] with 6 point gauss quadrature scheme[97]. To decide the range of control factors/parameters a simulation of the above mentioned problem is performed with EFGM by considering a variable range of 150 to 2400 nodes in problem geometry(n_T) with a varying 2 to 8 point Gauss quadrature and changeable values of d_{max} from 1 to 3. For various nodal arrangements and varying Gauss quadrature the minimum to maximum variation of nodes in support domain(n_d) remained the same for a particular value of the scaling parameter. With the help of the results in Table.5.1 and literature works[15,80,96] the maximum and minimum values of all the control factors are selected and displayed in Table.5.2. For the simulations with $n_T = 150$ having varying Gauss quadrature(2-8) when the value of n_d exceeds 15

i.e. above a scaling parameter of 2 ($d_{max} > 2$) the simulation leads to extremely erroneous results hence the value of n_r is limited to 15 in Table.5.2.

The worth of the projected criterion is probed with 16 trial cases of simulations in accordance with L-16 Taguchi orthogonal array[98]. Table. 3 displays the results of simulations with various control factors/parameters of L-16 Taguchi orthogonal array. The time taken for each simulation is also displayed in Table.5.3. Mode-I SIF(K_1^{EFGM}) values from various EFGM simulations are compared with Mode-1 SIF of Ref.1($K_1^{Ref.1}$)[96] and the relative deviation(RD) is calculated. Mathematically RD is given as:

$$RD = \left| \left(\frac{K_1^{Ref.1} - K_1^{EFGM}}{K_1^{Ref.1}} \right) \times 100 \right| \quad (5.21)$$

The analysis was performed by widely used software specifically used for design of experiment applications known as MINITAB 17. For simulation of results using MATLAB Dell machine with i5-5200U-CPU with 8GB RAM and

64 bit operating system was used. The experimental observations are further converted into a signal-to-noise (S/N) ratio. The S/N ratios available depend on the type of characteristics. The characteristic that lower value represents better accuracy of simulation such as lower relative deviation is called "lower is better" LB. Henceforth LB for relative deviation(RD) is obtained for optimum simulation results. The loss function L for objective is defined as follows:

$$L_{LB} = \frac{1}{n} \sum_{i=1}^n y_{RD}^2 \quad (5.22)$$

where Y_{RD} is response for relative deviation(RD) and n represents number of experiments.

The S/N ratio can be calculated as a logarithmic transformation of response function given by:

$$S/N \text{ ratio for } RD = -10 \log_{10}(L_{LB}) \quad (5.23)$$

Table.5.1 Range of n_d using EFGM

S.No.	n_T	Gauss	d_{\max}	n_d (Min-Max)
Quadrature				
1.	150-2400	2-8	1	6-9
2.	150-2400	2-8	1.5	9-13
3.	150-2400	2-8	2	11-15
4.	150-2400	2-8	2.5	16-24
5.	150-2400	2-8	3	23-33

The mean of S/N ratio from Table.5.3 of deviation is -17.93db. The S/N ratio response table shown in Table.5.4 show the effect of control factors on relative deviation.

Table.5.2. Levels for various control factors

Level						
Control factor	Symbol	I	II	III	IV	
Total number of nodes in problem	A	150	600	1350	2400	
Gauss quadrature	B	2×2	4×4	6×6	8×8	
Desired random number of nodes in support domain(n_r)	C	6	9	12	15	

It can be concluded from the results obtained in Tables.(5.3-5.5) that factors at levels A₁, B₄ and C₃ (i.e. $n_T = 150$, Gauss quadrature of 8×8 and $n_r = 12$) contribute most towards minimization of relative deviation, the simulation carried out using the optimized parameters generated a value of 2.3652 units minimizing the relative deviation(RD) to 0.35%. The time taken for simulation with optimized parameters was 35.6 seconds. Table.5.5 represents the optimized values though means which complement the S/N ratio values establishing that the optimization is accurately done.

Table5.3 Orthogonal array for L16 (4³) Taguchi design

L16 (4 ³)	A	B	C	K _t	K _t (Ref.1)	RD(%)	S/N	Comp.
(EFGM)					RATIO(db)		Time(Sec)	
1	150	2	6	0.7318	2.3570	68.95	-36.7708	5
2	150	4	9	2.1641	2.3570	8.18	-18.2585	11
3	150	6	12	2.4686	2.3570	4.73	-13.5113	22
4	150	8	15	2.3809	2.3570	1.01	-0.1550	41
5	600	2	9	3.2337	2.3570	37.19	-31.4101	22
6	600	4	6	-0.1204	2.3570	105.10	-40.4329	40
7	600	6	15	2.4742	2.3570	4.97	-13.9317	148
8	600	8	12	2.3454	2.3570	0.48	6.2062	234
9	1350	2	12	2.5203	2.3570	6.93	-16.815	92
10	1350	4	15	2.2688	2.3570	3.73	-11.4556	258
11	1350	6	6	0.0040	2.3570	99.82	-39.9852	471
12	1350	8	9	2.3546	2.3570	0.09	20.1856	934
13	2400	2	15	2.8705	2.3570	21.78	-26.7649	345
14	2400	4	12	2.5148	2.3570	6.69	-16.5155	875
15	2400	6	9	2.4119	2.3570	2.32	-7.3459	1843
16	2400	8	6	0.0018	2.3570	99.92	-39.9932	3966

Table.5.4 Response Table for Signal to Noise Ratios

Level	A	B	C
1	-17.174	-27.940	-39.296
2	-19.892	-21.666	-12.207
3	-12.018	-18.694	-10.159
4	-22.655	-3.439	-11.077
Delta	10.637	24.501	30.088

Table.5.5 Response Table for Means

Level	A	B	C
1	20.722	33.717	93.453
2	36.942	30.932	11.952
3	27.649	27.967	4.713
4	32.684	25.382	7.880
Delta	16.220	8.335	88.740

5.3 Conclusion

The evolution of EFGM has been focused on improving the inherent flaws in conventional EFGM. The coupling procedures remove the difficulties associated with implementation of boundary conditions and the optimization improves the overall working of this method. Following points can be drawn from this chapter:

- Coupled FE-EFG produced very accurate displacement results the EFG approximation was used near the crack tip only to reduce computational costs.
- It is easy to implement essential boundary conditions via coupled EFG-RPIM method as RPIM shape functions posses Kronecker delta property.
- The optimization helps in establishing an optimum value of domain nodes that can be used for simulating fracture mechanics problems using OEFG.
- An average 80% reduction in computational time can be achieved and a very few number of nodes are needed to perform the simulation in comparison to conventional EFGM.

CHAPTER 6

NUMERICAL INTEGRATION AND STRESS INTENSITY FACTOR CALCULATION IN EFGM

6.1 Numerical Integration

A complete integration of domain is required for the evaluation of stiffness matrix (K), displacement matrix (u) and force vector (f) in Eq.(3.12), which corresponds to area integration in two dimensions. A numerical integration scheme such as Gauss quadrature is necessary for computation of stiffness matrix and force vector, for which the subdivision of domain is done. Many integration techniques are proposed in meshless methods over the years [52] e.g. direct nodal integration, stabilized nodal integration, [99] stress point integration, support based integration but in the case of fracture analysis using EFGM two types of subdivision techniques as shown in Fig.6.1 are mostly used for the purpose of integration. Element quadrature as shown in Fig.6.1a uses a finite element mesh generator to create a cell structure which matches with the problem domain. The second integration technique, which is often called cell quadrature, uses background cells, which is independent of the problem domain as shown in Fig.6.1b. During integration over the problem domain, a particular quadrature point is checked whether it lies inside the domain or not.

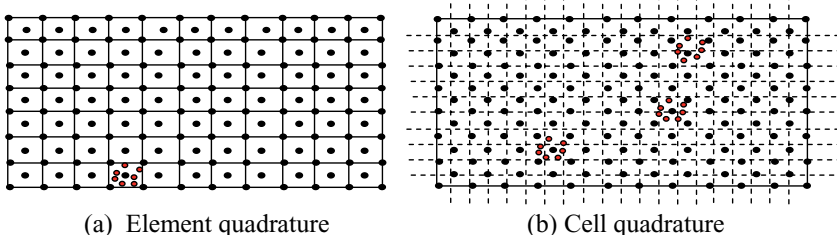


Fig.6.1. Integration techniques of EFGM

To enhance the accuracy of Gauss quadrature, a sub-triangle technique is used [78] as it circumvents the difficulties related to discontinuities are present within a background cell. Sukumar et al. [100] established that a continuous increment in order of Gauss integration will not always improve the integration over a

discontinuous element/cell. This numerical difficulty was surmounted by using an approach similar to one projected by Dolbow [101] for extended finite element method (XFEM). According to this technique, any background cell which intersects with a crack is subdivided at both sides into sub-triangles whose edges are adapted to crack faces, as shown in Fig.6.2. It is imperative to note that, while triangulation of the crack tip element considerably improves the accuracy of integration by increasing the order of Gauss quadrature, it also shuns the numerical complications of singular fields at the crack tip because none of the Gauss points are placed on the position of the crack tip.

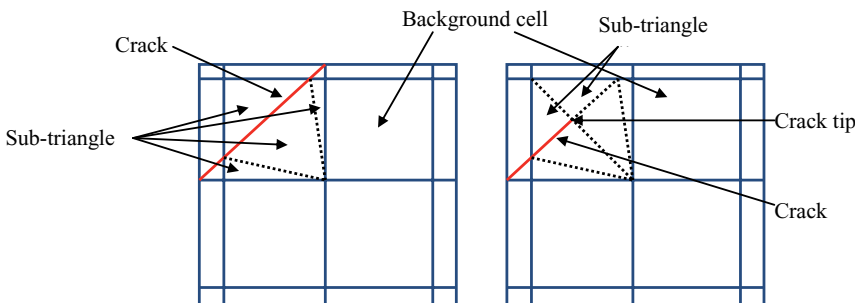


Fig.6.2 Sub-triangle technique for partitioning the cracked background cell:
(a) crack edge and (b) crack tip.

6.2 Calculation Of Stress Intensity Factor

A great deal of research has gone into methods for determining stress intensity factors for various geometries and loadings. The development of numerical methods such as finite elements and boundary elements has facilitated the calculation of crack tip stress fields and many methods have been developed for inferring stress intensity factors e.g., displacement and stress extrapolation, displacement and stress correlation, enriched elements, J integral. The J -integral method developed by Rice[102] is most widely used to evaluate SIFs in the codes implemented in EFGM.

6.2.1 J-Integral

Rice [102] proposed a path independent energy-momentum tensor that could be used as a fracture parameter when the contour enclosed a crack tip. The J integral is given by:

$$J = \int_{\Gamma} \left[W \delta_{ij} - \sigma_{ij} \frac{\partial u_i}{\partial x_j} \right] n_j d\Gamma \quad (6.1)$$

where $W = \int_0^e \sigma d\varepsilon$ is the strain energy density, σ is the stress, and n is the outward unit normal to an arbitrary contour enclosing the crack tip. The path independence property allows the J integral to be evaluated using far field information which is generally more accurate than near-tip results for numerical methods. Path independence is easily shown by considering the closed contour $\Gamma = \Gamma_1 + C_+ + \Gamma_2 + C_-$ around the tip of a straight crack with \mathbf{m} as the normal to the closed contour (see Fig. 24). Along the entire contour, Eq. (6.1) can be written as:

$$J' = \int_{\Gamma_1} \left[W \delta_{ij} - \sigma_{ij} \frac{\partial u_i}{\partial x_j} \right] m_j d\Gamma + \int_{\Gamma_2} \left[W \delta_{ij} - \sigma_{ij} \frac{\partial u_i}{\partial x_j} \right] m_j d\Gamma + \int_{C_+ + C_-} \left[W n_1 - \sigma_{ij} \frac{\partial u_i}{\partial x_j} \right] m_j d\Gamma = 0 \quad (6.2)$$

where, the prime is used to indicate that J is written for a closed contour. Along the crack faces $C_+ + C_-, m_1 = 0$ and $\sigma_{ij} m_j = t_i = 0$ (traction-free crack faces) so that the last integral in Eq. (6.2) equals zero. Reversing the direction of the normal \mathbf{m} on the inside contour Γ_1 to be the outward normal \mathbf{n}_{Γ_1} leads to $J_{\Gamma_1} = J_{\Gamma_2}$

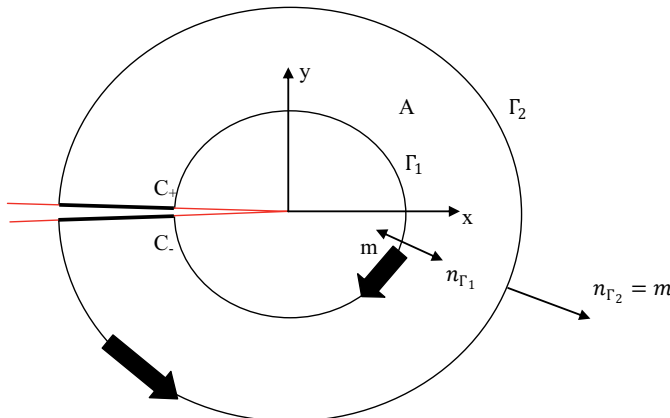


Fig.6.3 Path independent closed contour about the tip of a crack

6.2.2 SIF Computation For Isotropic Material

The J -integral is equal to the energy release rate for elastic materials. For a general mixed-mode case J -integral is defined as:

$$J = G = \frac{1}{E'} (K_I^2 + K_{II}^2) \quad (6.3)$$

where,

$$E' = \begin{cases} E & \text{plane stress} \\ \frac{E}{1-\nu^2} & \text{plane strain} \end{cases} \quad (6.4)$$

The interaction integral by Shih C.F. [103] is an effective tool for extracting the mixed-mode stress intensity factors, and a complete procedure is given below.

Consider two independent equilibrium states of a cracked body. State 1 is defined here to be the actual state for the given boundary conditions while state 2 is defined to be an auxiliary state which will be given later. The J -integral for two superposed states is given by:

$$J^s = J^{tot} = \int_{\Gamma} \left[W^{tot} \delta_{ij} - (\sigma_{ij}^{(1)} + \sigma_{ij}^{(2)}) \frac{\partial(u_i^{(1)} + u_i^{(2)})}{\partial x_j} \right] n_j d\Gamma \quad (6.5)$$

where,

$$W^{tot} = \frac{1}{2} (\sigma_{ij}^{(1)} + \sigma_{ij}^{(2)}) (\varepsilon_{ij}^{(1)} + \varepsilon_{ij}^{(2)}) \quad (6.6)$$

Eq. (6.5) can be expanded and rearranged as

$$\begin{aligned} J^{tot} &= \int_{\Gamma} \left[W^{(1)} \delta_{ij} - \sigma_{ij}^{(1)} \frac{\partial u_i^{(1)}}{\partial x_j} \right] n_j d\Gamma + \int_{\Gamma} \left[W^{(2)} \delta_{ij} - \sigma_{ij}^{(2)} \frac{\partial u_i^{(2)}}{\partial x_j} \right] n_j d\Gamma \\ &\quad + \int_{\Gamma} \left[W^{(1,2)} \delta_{ij} - \sigma_{ij}^{(1)} \frac{\partial u_i^{(2)}}{\partial x_j} - \sigma_{ij}^{(2)} \frac{\partial u_i^{(1)}}{\partial x_j} \right] n_j d\Gamma \\ &= J^{(1)} + J^{(2)} + M^{(1,2)} \end{aligned} \quad (6.7)$$

Where, $J^{(1)}$ and $J^{(2)}$ are the J integral for states 1 and state 2, respectively. $M^{(1,2)}$ is the interaction integral for the two equilibrium states

$$M^{(1,2)} = \int_{\Gamma} \left[W^{(1,2)} \delta_{ij} - \sigma_{ij}^{(1)} \frac{\partial u_i^{(2)}}{\partial x_j} - \sigma_{ij}^{(2)} \frac{\partial u_i^{(1)}}{\partial x_j} \right] n_j d\Gamma \quad (6.8)$$

and $W^{(1,2)}$ is the mutual strain energy

$$W^{(1,2)} = \frac{1}{2} (\sigma_{ij}^{(1)} \varepsilon_{ij}^{(2)} + \sigma_{ij}^{(2)} \varepsilon_{ij}^{(1)}) \quad (6.9)$$

Irwin's relation for the superposed states is written as ($J^S = J^{tot}$)

$$\begin{aligned} J^{tot} &= \left[(K_I^{(1)})^2 + (K_H^{(1)})^2 \right] + \left[(K_I^{(2)})^2 + (K_H^{(2)})^2 \right] + \left[K_I^{(1)} K_I^{(2)} + K_H^{(1)} K_H^{(2)} \right] \\ &= J^{(1)} + J^{(2)} + (K_I^{(1)} K_I^{(2)} + K_H^{(1)} K_H^{(2)}) \end{aligned} \quad (6.10)$$

Comparing Eq. (6.7) with Eq. (6.10) leads to the following relationship

$$M^{(1,2)} = \frac{2}{E'} (K_I^{(1)} K_I^{(2)} + K_H^{(1)} K_H^{(2)}) \quad (6.11)$$

where, $M^{(1,2)}$ is computed using Eq. (6.8).

The computation of individual stress intensity factors from actual field requires that the auxiliary field should be chosen judiciously. To do so, let's consider the auxiliary field to be the mode 1 asymptotic stress field and displacement field defined by Eqs.(6.12)-(6.13).

$$\sigma_{xx} \approx \frac{K_I}{\sqrt{2\pi r}} \cos \frac{\theta}{2} \left(1 - \sin \frac{\theta}{2} \sin \frac{3\theta}{2} \right) \quad (6.12a)$$

$$\sigma_{yy} \approx \frac{K_I}{\sqrt{2\pi r}} \cos \frac{\theta}{2} \left(1 + \sin \frac{\theta}{2} \sin \frac{3\theta}{2} \right) \quad (6.12b)$$

$$\sigma_{xy} \approx \frac{K_I}{2\sqrt{2\pi r}} \sin \theta \cos \frac{3\theta}{2} \quad (6.12c)$$

The associated compatible displacement field is

$$u_x \approx \frac{K_I}{2\mu} \sqrt{\frac{r}{2\pi}} \cos \frac{\theta}{2} (\kappa - \cos \theta) \quad (6.13a)$$

$$u_y \approx \frac{K_I}{2\mu} \sqrt{\frac{r}{2\pi}} \sin \frac{\theta}{2} (\kappa - \cos \theta) \quad (6.13b)$$

For this case, $K_I^{(2)}=1$, $K_H^{(2)}=0$ and Eq.(6.11) reduces to

$$M^{(1,2)} = \frac{2}{E'} (K_I^{(1)}) \quad (6.14)$$

Computing $M^{(1,2)}$ from Eq.(6.8) allows the solution for the mode 1 stress intensity factor as

$$K_I^{(1)} = \frac{2}{E'} M^{(1,2)} \quad (6.15)$$

Similarly, the mode 2 stress intensity factor can be found by choosing the auxiliary field to be the mode 2 asymptotic solution with $K_I^{(2)}=0$, $K_H^{(2)}=1$. The integral $M^{(1,2)}$ in Eq. (6.8) is computed with this auxiliary field, and the mode 2 stress intensity factor can be obtained as

$$K_H^{(2)} = \frac{2}{E'} M^{(1,2)} \quad (6.16)$$

The contour integral in Eq.(6.14) can be converted to an equivalent domain integral by Gauss's theorem, and can be written as:

$$M^{(1,2)} = \int_A \left[\sigma_{ij}^{(1)} \frac{\partial u_i^{(2)}}{\partial x_j} + \sigma_{ij}^{(2)} \frac{\partial u_i^{(1)}}{\partial x_j} - W^{(1,2)} \delta_{ij} \right] \frac{\partial q}{\partial x_j} dA \quad (6.17)$$

where, "q" is defined weight having some value inside the domain and zero otherwise.

6.2.3 SIF Computation Using Orthotropic Enrichment Functions

In this section the generalized equations for calculation for SIFs using orthotropic enrichment functions are presented. The technique developed by Kim and Paulino [104] to evaluate mixed-mode stress intensity factor is applied. Auxiliary stress and displacement fields are defined by asymptotic fields near the crack tip given by analytical solutions Eqs.(4.70-4.75)

The initial steps of the computation can be considered same as in Eqs. (6.3-6.9). Now the strain of auxiliary field, in this case, is defined as:

$$\varepsilon_{ij}^2 = \frac{1}{2} (u_{i,j}^2 + u_{j,i}^2) \quad (6.18)$$

After some manipulations, M can be written in the following form [77]

$$M = 2e_{11}K_I K_I^2 + e_{12}(K_I K_{II}^2 + K_I^2 K_{II}) + 2e_{22}K_{II} K_{II}^2 \quad (6.19)$$

where

$$e_{11} = \frac{-c_{22}}{2} lm\left(\frac{s_1+s_2}{s_1 s_2}\right) \quad (6.20)$$

$$e_{12} = \frac{-c_{22}}{2} lm\left(\frac{1}{s_1 s_2}\right) + \frac{c_{11}}{2} lm(s_1 s_2) \quad (6.21)$$

$$e_{22} = \frac{c_{11}}{2} lm(s_1 + s_2) \quad (6.22)$$

Having calculated M form Eq.(6.19), the SIF's can be obtained by considering the two states (state I: $K_I^{aux}=1, K_{II}^{aux}=0$; state II: $K_I^2=0, K_{II}^2=1$) and solving the following system of linear algebraic equation,

$$M^{(1,state\ I)} = 2e_{11}(K_I) + 2e_{12}(K_{II}) \quad (6.23)$$

$$M^{(1,state\ II)} = 2e_{12}(K_I) + 2e_{22}(K_{II}) \quad (6.24)$$

6.2.4 SIF Computation For Isotropic Functionally Graded Material

For linear elastic material models, it can be proved that $W = \sigma_{ij} \varepsilon_{ij}/2$. Using Gauss divergence theorem the contour integral in Eq.(6.3) can be converted into equivalent domain form and can be written as

$$J = \int_A \left(\sigma_{ij} \frac{\partial u_i}{\partial x_1} - W \delta_{1j} \right) \frac{\partial q}{\partial x_j} dA + \int_A \frac{\partial}{\partial x_j} \left(\sigma_{ij} \frac{\partial u_i}{\partial x_1} - W \delta_{1j} \right) q dA \quad (6.25)$$

Where, "q" is defined weight having some value inside the domain and zero otherwise and A is the area inside the contour. Now just expanding the second integrand in Eq. (6.25) we get

$$J = \int_A \left(\sigma_{ij} \frac{\partial u_i}{\partial x_1} - W \delta_{1j} \right) \frac{\partial q}{\partial x_j} dA + \int_A \left(\frac{\partial \sigma_{ij}}{\partial x_j} \frac{\partial u_i}{\partial x_1} + \sigma_{ij} \frac{\partial^2 u_i}{\partial x_j \partial x_1} - \sigma_{ij} \frac{\partial \varepsilon_{ij}}{\partial x_1} - \frac{1}{2} \varepsilon_{ij} \frac{\partial D_{ijkl}}{\partial x_1} \varepsilon_{kl} \right) q dA \quad (6.26)$$

For non-homogeneous materials, even though the equilibrium and compatibility conditions are satisfied, the material gradient term of the second integrand of Eq.(6.26) does not vanish. So \tilde{J} -integral [105], which is written as

$$J = \int_A \left(\sigma_{ij} \frac{\partial u_i}{\partial x_1} - W \delta_{1j} \right) \frac{\partial q}{\partial x_j} dA + \int_A \left(\frac{1}{2} \varepsilon_{ij} \frac{\partial D_{ijkl}}{\partial x_1} \varepsilon_{kl} \right) q dA \quad (6.27)$$

In order to derive interaction integral for FGMs, consider again actual (state 1), auxiliary (state 2), and superimposed (state S) equilibrium states. For the actual state, Eq.(6.27) can be directly invoked to represent the \tilde{J} -integral. However, a more general form, such as Eq.(6.25), must be used for auxiliary and superimposed states. For example, the \tilde{J} -integral for the superimposed state S can be written as

$$\tilde{J}^S = \int_A \left(\left(\sigma_{ij}^{(1)} + \sigma_{ij}^{(2)} \right) \frac{\partial(u_i^{(1)} + u_i^{(2)})}{\partial x_1} - W^{(S)} \delta_{1j} \right) \frac{\partial q}{\partial x_j} dA + \int_A \left(\frac{\partial}{\partial x_j} \left(\sigma_{ij}^{(1)} + \sigma_{ij}^{(2)} \right) \frac{\partial(u_i^{(1)} + u_i^{(2)})}{\partial x_1} - W^{(S)} \delta_{1j} \right) q dA \quad (6.28)$$

Clearly, the evaluations of \tilde{J}^S and the resulting interaction integral depend on how the auxiliary field is defined. There are two methods (i) homogeneous auxiliary

field and (ii) non-homogeneous auxiliary field [105]. The generalized equation of interaction integral from both these methods is given below:

$$\tilde{M}^{Method-1} = \int_A \left(\sigma_{ij}^{(1)} \frac{\partial u_i^{(2)}}{\partial x_1} + \sigma_{ij}^{(2)} \frac{\partial u_i^{(1)}}{\partial x_1} - W^{(S)} \delta_{1j} \right) \frac{\partial q}{\partial x_j} dA + \int_A \frac{1}{2} \left[\sigma_{ij}^{(1)} \frac{\partial \varepsilon_{ij}^{(2)}}{\partial x_1} - \frac{\partial \sigma_{ij}^{(2)}}{\partial x_1} \varepsilon_{ij}^{(1)} + \sigma_{ij}^{(2)} \frac{\partial \varepsilon_{ij}^{(1)}}{\partial x_1} - \frac{\partial \sigma_{ij}^{(1)}}{\partial x_1} \varepsilon_{ij}^{(2)} \right] q dA \quad (6.29)$$

$$\begin{aligned} \tilde{M}^{Method-2} &= \\ \int_A \left(\sigma_{ij}^{(1)} \frac{\partial u_i^{(2)}}{\partial x_1} + \sigma_{ij}^{(2)} \frac{\partial u_i^{(1)}}{\partial x_1} - W^{(S)} \delta_{1j} \right) \frac{\partial q}{\partial x_j} dA + \int_A \left(\sigma_{ij}^{(1)} \left(\frac{\partial^2 u_i^{(2)}}{\partial x_i \partial x_1} - \frac{\partial \varepsilon_{ij}^{(2)}}{\partial x_1} \right) - \right. \\ &\quad \left. \varepsilon_{ij}^{(1)} \frac{\partial D_{ijkl}}{\partial x_1} \varepsilon_{kl}^{(2)} \right) q dA \end{aligned} \quad (6.30)$$

The SIFs can be obtained using Eqs. (6.16-6.17) by a similar procedure as explained in the previous section.

The interaction integral scheme can be extended to simulate thermo-elastic loadings as well by addition of thermal stress/strain terms. The study of fracture under thermo-elastic loads has been efficiently performed in the works by Goli et al.[106] and Garg and Pant[51]

6.3 Conclusions

This chapter presents the issues on integration techniques and derivations of SIFs. The integration technique and its successful application is backbone of EFGM. Various forms are available to derive SIFs which may cause difficulty in coding. Following conclusions can be drawn from this chapter:

- The background integration scheme is most accurate in comparison to other schemes.
- Several formulation of interaction integral for non-homogeneous materials have been developed [105,107,108]. The non-equilibrium formulation used in the work by Garg and Pant[109] produces a very simple final form of M-integral. In terms of accuracy the results are as good as the incompatibility formulation and in comparison to constant constitutive tensor formulation this form can produce more efficient results[108].

CHAPTER 7

NUMERICAL RESULTS

7.1 Numerical Examples

This chapter aims to discuss a variety of problems based on topics/techniques discussed in previous chapters. The problems successfully demonstrate the versatile ability of EFGM in handling a multitude of variations effectively.

7.1.1 A Plate With An Edge Crack

The dimensions of the problem considered for this problem are shown in Fig.7.1, where $H = 200$ mm, $W = 100$ mm. A far field stress $\sigma_0 = 100$ MPa is applied as shown in Fig.7.1. The material is ASTM 36 steel with modulus of elasticity, $E = 200$ GPa, and Poisson's ratio, $\nu = 0.3$.

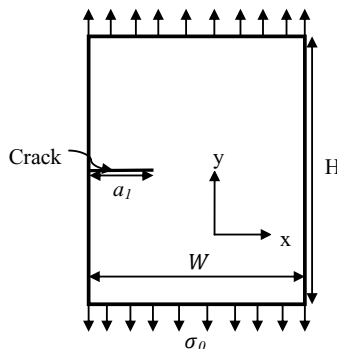


Fig.7.1 Problem geometry, dimension and loading conditions

The main crack has been taken at a distance of $H/2$ i.e. 100 mm from the bottom with crack orientation of $\alpha = 0^\circ$ ($\alpha = 0^\circ$ implies that the crack is parallel to the x -axis, Fig.7.1). The results are compared with those obtained by commercial finite element package (ANSYS, version 13) throughout the work.

Single edge crack along with its geometry and boundary conditions is shown in Fig.7.1. The bottom edge has been constrained along y -direction, and an external far field stress is applied at the top edge. The plate domain has been discretized using 800 (20x40) regularly arranged nodes throughout this case. Six point Gauss

quadrature has been used for the numerical integration [19] of the Galerkin weak form. A plane stress condition has been assumed. The values of mode – I and mode – II stress intensity factors i.e. K_I and K_{II} have been calculated using domain based interaction integral approach. A comparison of results modeled by intrinsic and visibility criterion with finite element results is shown in Fig.7.2 and it is clear that the accuracy of intrinsic enrichment is more than visibility method.

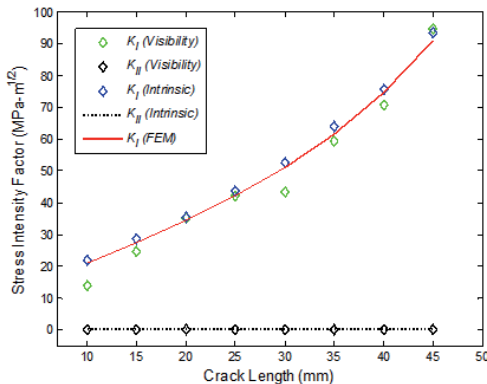


Fig.7.2. Comparison between intrinsic and visibility criterion

7.1.2 A Plate With Parallel Cracks

In this subsection, the effect of a parallel crack on SIF of the main crack at the crack tip is studied. The analysis is done using modified intrinsic enrichment criterion described in section 4.1.2.3.2. There are other configurations of multiple cracks possible [15,71] which can be analyzed by the same criterion and its improved version as explained in section 4.1.2.3.2.1, but for justification only parallel crack configuration is used in this article.

The problem geometry involves crack lengths of both the cracks equal to 40 mm and they are offset by a distance $d = 20$ mm. The material properties, loading conditions and dimensions of the problem are similar to the edge crack problem as shown in Fig.7.1.

The main crack has been taken at a distance of $H/2$ i.e. 100 mm from the bottom with crack orientation of $\alpha = 0^\circ$ ($\alpha = 0^\circ$ implies that the crack is parallel to the x -

axis, Fig.7.3), whereas the other crack is placed at 20 mm offset from the main crack. The problem of parallel crack plate is shown in Fig.7.3.

By using element free Galerkin (EFG) method the stress intensity factor (SIF) is calculated as $59.9147 \text{ MPa}\cdot\text{m}^{1/2}$ for mode – I and $11.8486 \text{ MPa}\cdot\text{m}^{1/2}$ for mode – II.

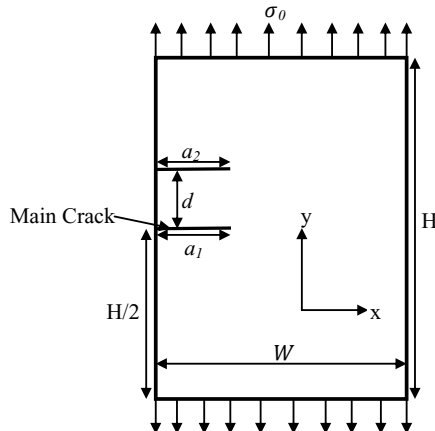


Fig.7.3 Problem geometry, plate with parallel edge cracks

For validation of results finite element package (ANSYS, version 13) is applied for the calculation of SIF and it is equal to $60.911 \text{ MPa}\cdot\text{m}^{1/2}$ for mode – I and $11.172 \text{ MPa}\cdot\text{m}^{1/2}$ for mode – II. The EFG results are very close to the results obtained by ANSYS. The maximum percentage error between the results obtained by EFGM and finite element method (ANSYS) is 1.63%.

The nodal density (20×40) distribution of a plate with a parallel crack of equal length plotted by MATLAB is shown in Fig.7.4. In this nodal arrangement the total number of nodes are equal to 800, out of which 20 nodes are arranged in horizontal direction and 40 nodes are arranged in vertical direction, in such a way so that all the nodes are equally distributed over the domain.

The deformed shape of the cracked plate when the crack is at 20 mm offset from the original position, by EFGM is shown in the plotted Fig.7.5.

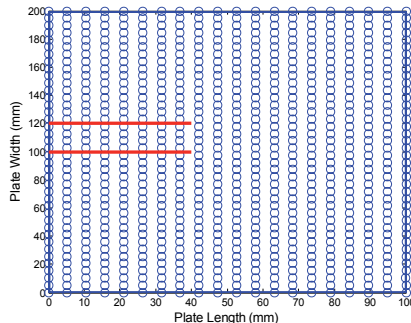


Fig.7.4 Nodal density distribution of a plate with parallel edge crack

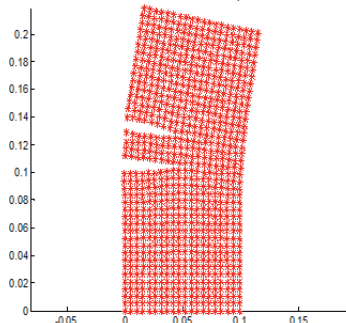


Fig.7.5 Deformed shape by EFGM

7.1.3 Bi-Material Plate With Crack At Interface

This problem is taken into account in this article to show the prowess of EFGM in handling strong and weak discontinuities. The cracked region that is a strong discontinuity has been modeled using intrinsic enrichment criterion explained in section 4.1.2.3.1. and the material discontinuity at the interface has been treated by jump function approach elaborated in section 4.1.1.3. Cubic spline weight function has been used for generating the EFGM shape functions. The value of scaling parameter (d_{max}) is taken as 1.5 for the entire simulation. The essential boundary conditions have been imposed using Lagrange multiplier approach. Element quadrature scheme has been used for the numerical integration of weak form. The

problem domain has been divided into background cells, and in each background cell, four points Gauss quadrature [55] i.e. 16 Gauss points have been used for the numerical integration [57] of the Galerkin weak form. The geometry has been discretized using 25 uniformly distributed nodes along x-direction and 50 nodes along y-direction i.e. total 1250 (25×50) nodes and 1176 (24×49) background cells.

For this problem, the mixed mode stress intensity factors K_I and K_{II} are evaluated using the domain form [103] of the contour interaction integral explained earlier. The auxiliary displacement fields for an interfacial crack can be extracted using the stated equations used in interaction integral method, and the interaction integral is related to the stress intensity factors through the relation [110]

$$M^{(1,2)} = \frac{2}{\cosh^2(\pi\varepsilon)E^*} \left[(K_I^{(1)}K_I^{(2)} + K_{II}^{(1)}K_{II}^{(2)}) \right] \quad (7.1)$$

E^* is the equivalent Young's modulus and ε the bi-material constant [110] of the bi-material system.

7.1.3.1 Bi-Metallic Plate With An Interfacial Edge Crack

A bi-metallic plate having an edge crack of length a , is subjected to a tensile load on upper and lower boundaries as shown in Fig.7.6. The plate dimensions are scaled with $W = 3$ units, $H = 9$ units, and far field applied stress $\sigma_0 = 1$ unit. The values of Poisson's ratios are taken as $\nu_1 = \nu_2 = 0.3$. The problem was earlier solved by [38] wherein the results were obtained for several ratios of Young's moduli $E_2/E_1 = 2, 3, 10, 100$, where E_1 is kept constant at 100 units and crack lengths $a/W = 0.2, 0.3, 0.4, 0.5, 0.6$. In this article only the results concerning Young's moduli ratio 2 and 3 are simulated and shown. Normalized stress intensity factors are shown in Fig.7.7(a)-7.7(b) where the results marked as Ref.1 and Ref.2 are taken from [111] and [112] respectively.

Fig.7.7a shows the variation of normalized stress intensity factors i.e. K_I and K_{II} with varying crack length for $E_2/E_1 = 2$. The results show that with increase in crack length, K_I is increasing while K_{II} goes on decreasing. Next, the EFGM results are obtained for $E_2/E_1 = 3$ as shown in Fig.7.7b respectively.

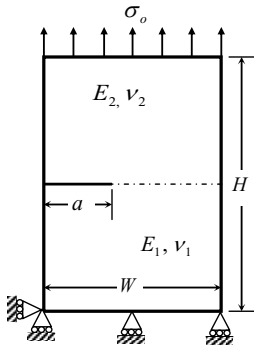


Fig.7.6 A bi-metallic interface edge crack

It can be clearly seen from Fig.7.7 that the values obtained by EFGM are quite close to the reference values, and the maximum percentage difference in EFGM results with reference solutions is less than 5%.

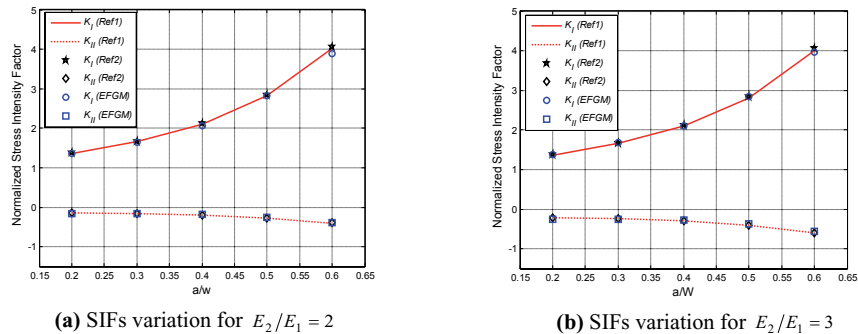


Fig.7.7: SIF variation for bi-material edge crack

7.1.4 Kinked Crack Modeling

The kinked crack problem is solved using criterion explained in section 4.1.2.5, the problem previously solved by Pant et. al [80] is taken and two kink crack problems are considered. Fig.7.8 shows the dimensions of the cracked body having $H = 200$ mm, $W = 100$ mm. The bottom edge has been constrained along y-direction, and an external far field stress is applied at the top edge. A regular nodal distribution of 648 nodes has been considered in both simulations. Six point Gauss quadrature has been used for the numerical integration of the Galerkin weak form. The problem

domain has been divided into background cells, and in each background cell six points Gauss quadrature i.e. 36 Gauss points in each cell have been used for the numerical integration of the Galerkin weak form. A plane stress condition has been assumed. The material properties for this study are taken as: modulus of elasticity (E) = 200 GPa, Poisson's ratio (ν) = 0.3. A far field stress, (σ_o) = 100 MPa is applied at the top edge. Three different crack configurations having two, three and four kinked segments have been modeled as shown in Figs.7.8(a),(b),(c) respectively. In order to have a clear visualization of near tip stress fields, stress contours have been generated for different crack configurations as shown in Figs.7.9-7.10. The modeling capability of criterion aforementioned has been verified for different crack configurations with different spatial and angular orientation. All the problems have been simulated by writing EFG codes (algorithms) written in MATLAB. In order to validate the proposed technique the Stress intensity factor results were compared with the Finite element method (ANSYS software) results. For modeling the problem domain in ANSYS a uniformly distributed nodal density of 1200 nodes was used. A PLANE82 finite element was used for discretization of problem geometry. The stress contours generated for different kinked crack configurations reveal the effective modeling capability of the criterion. In the next section the same criterion is used for modeling quasi-static crack propagation in two dimensional domains subjected to mixed-mode loading conditions. The next section also shows the modeling capabilities of EFGM in treating domains with holes.

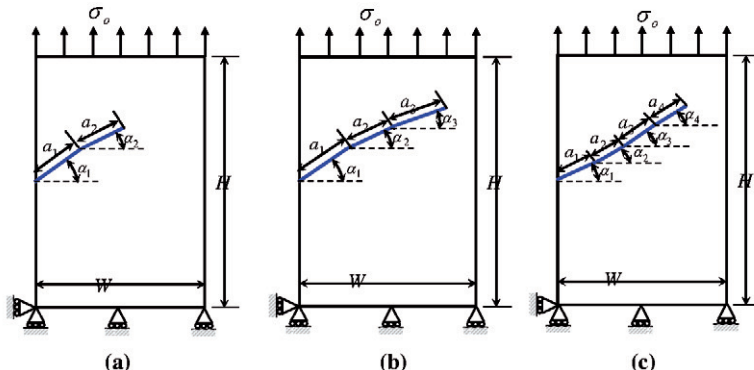


Fig.7.8. Kinked crack geometry along with boundary conditions

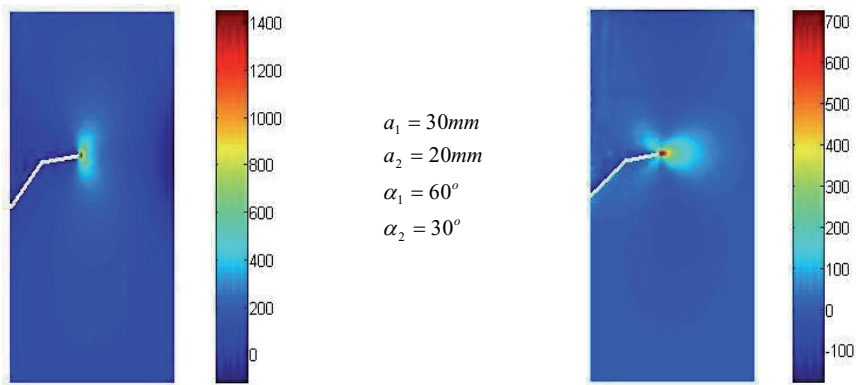


Fig.7.9 Stress contours for kinked cracks: (a) σ_{yy} ; (b) σ_{xx}

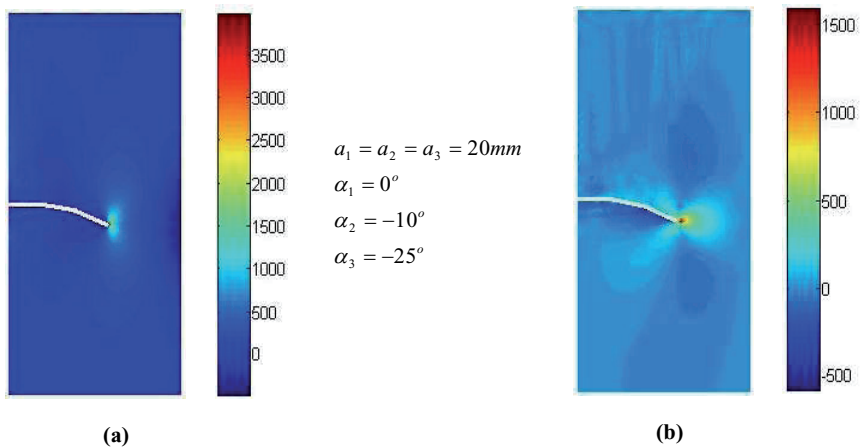


Fig.7.10 Stress contours for kinked cracks: (a) σ_{yy} ; (b) σ_{xx}

7.1.5 Quasi-Static Crack Growth

The simulation of quasi-static crack growth consists of evaluating equivalent stress intensity factor, and if it exceeds the fracture toughness of the material then the crack is extended by some finite length Δa in a particular direction found out by a

suitable crack growth criterion. The step size Δa is a user defined parameter, and should be chosen small enough to get an accurate crack growth path. The stress intensity factors are recalculated for the new crack geometry, and the crack is again extended in a new direction. This phenomenon continues until either the crack gets arrested or final failure takes place.

In this sub-section, two different model problems of quasi-static crack growth have been simulated by the criterion for modeling the kinked cracks [80]. All problems are subjected to mixed-mode loading either due to crack orientation or applied loading. Although, small crack segments predict a crack path more accurately than larger ones but here crack segment of 10 mm for quasi-static crack growth with initial crack length of 20 mm is considered. The crack propagation angle θ_m and equivalent mode-I stress intensity factor K_{leq} are calculated using following equations

$$\theta_m = 2 \tan^{-1} \frac{1}{4} \left[\frac{K_I}{K_{II}} \pm \sqrt{\left(\frac{K_I}{K_{II}} \right)^2 + 8} \right] \quad (7.2)$$

For this value of θ_m , $\sigma_{\theta\theta}$ is a principal stress field thus, $\sigma_{\theta\theta}$ may be written in terms of equivalent mode-I stress intensity factor (K_{leq}) which provides a single measure of the mixed-mode stress field.

$$\sigma_{\theta\theta} = \frac{1}{\sqrt{2\pi r}} \cos\left(\frac{\theta}{2}\right) \left[K_I \cos^2\left(\frac{\theta}{2}\right) - \frac{3}{2} K_{II} \sin\theta \right] = \frac{K_{leq}}{\sqrt{2\pi r}} \quad (7.3)$$

where,

$$K_{leq} = K_I \cos^3\left(\frac{\theta_m}{2}\right) - 3K_{II} \cos^2\left(\frac{\theta_m}{2}\right) \sin\left(\frac{\theta_m}{2}\right) \quad (7.4)$$

Fig. 35a shows the geometrical configuration of a plate with an inclined crack subjected to tensile stress of 100 MPa at the top edge. The crack located on the left edge has an initial inclination of 40° with the horizontal. The crack propagation path obtained for this case is shown in Fig.7.11(a), and the variation of equivalent mode-I stress intensity factor (K_{leq}) with crack length is plotted in Fig.7.11(b). From the crack growth path shown in Fig.7.11(a), it is observed that although

initially the crack is under mixed mode loading but it propagates in such a way that it attains a mode-I loading condition. From the results presented in Fig.7.11(b) it is seen that the value of equivalent stress intensity factor keeps on increasing with the increase in crack length.

In this final problem, the crack growth of an edge crack in the presence of a hole is investigated. The geometry of the plate along with loading and boundary conditions is shown in Fig.7.12(a). The crack is located on the left edge with an inclination of 40° with the horizontal. The crack propagation path for this problem is shown in Fig.7.12(a). From the crack growth path, it can be seen that the crack propagates in such a way that it gets arrested at the hole. From Fig. 7.12(b), it is seen that the equivalent mode-I SIF keeps on increasing with the increase in crack length, and a sudden rise in the value of SIF is found near the hole.

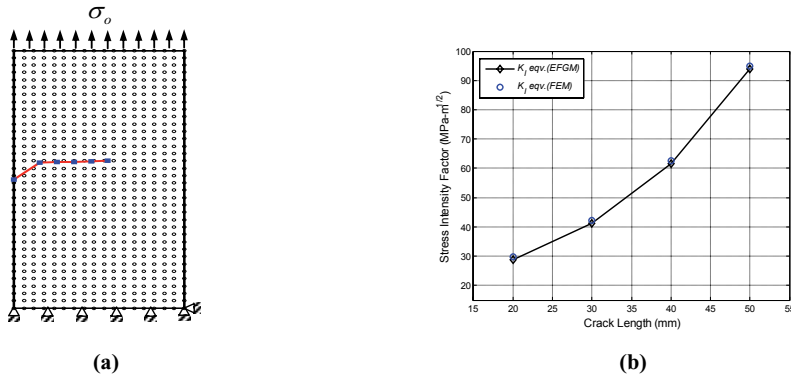


Fig.7.11 (a) Crack growth path (b) Equivalent mode-I stress intensity factor vs. crack length

(For initially inclined single edge crack subjected to tensile loading)

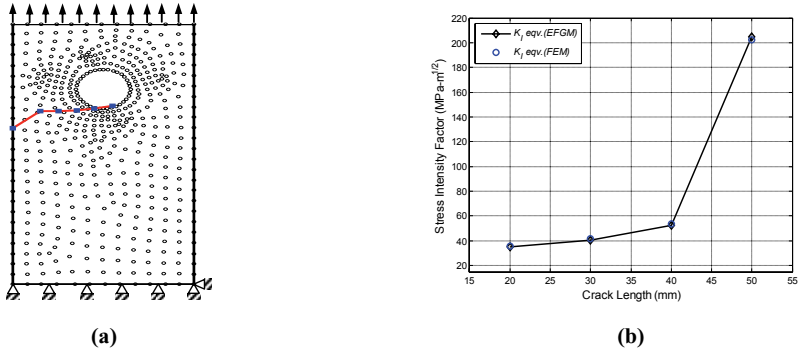


Fig.7.12 (a) Crack growth path (b) Equivalent mode-I stress intensity factor vs. crack length

(For an inclined edge crack in presence of a hole)

7.1.6 An Edge Crack In A Rectangular FGM Domain

An edge cracked functionally graded domain with material properties variation defined by hyperbolic tangent function is analyzed in this section. The boundary conditions are given with respect to the reference temperature $\Theta = T - T_0$, where T is the applied temperature and T_0 is the ambient temperature. The material properties like Young's modulus(E), Poisson's ratio(v), Thermal conductivity(k), Coefficient of thermal expansion(β) follow hyperbolic-tangent gradation.

$$E(X_1) = \frac{E^- + E^+}{2} + \frac{E^- - E^+}{2} \tanh[\xi(X_1 + d)] \quad (7.5)$$

$$\nu(X_1) = \frac{\nu^- + \nu^+}{2} + \frac{\nu^- - \nu^+}{2} \tanh[\bar{\delta}(X_1 + d)] \quad (7.6)$$

$$\beta(X_1) = \frac{\beta^- + \beta^+}{2} + \frac{\beta^- - \beta^+}{2} \tanh[\tilde{\delta}(X_1 + d)] \quad (7.7)$$

$$k(X_1) = \frac{k^- + k^+}{2} + \frac{k^- - k^+}{2} \tanh[\bar{\delta}(X_1 + d)] \quad (7.8)$$

where

$$(E^-, E^+) = (1, 3) \text{ GPa}, \quad (\nu^-, \nu^+) = (0.3, 0.1), \quad (\beta^-, \beta^+) = (0.01, 0.03)^\circ \text{C}^{-1}, \quad (k^-, k^+) = (1, 3) \text{ W/m}^\circ \text{C}, \quad \xi = 15, \quad \delta = 5, \quad d = 0$$

Fig.7.13(a) shows the dimensions ($W = 2\text{m}$ and $H = 2\text{m}$) of FGM domain along with an edge crack of length a . The top and bottom edges are constraint in the y -direction. The problem domain is subjected to a steady state thermal loading having $T_1 = -10^\circ\text{C}$ and $T_2 = 0^\circ\text{C}$ on left and right edges respectively. The top and bottom edges are considered to be insulated so that there is no flow of heat flux across them.

Fig.7.13(b) shows the temperature distribution over the domain under steady state condition. The relative deviation is calculated from results in Ref.3 FEM solution by KC and Kim[113] and it shows that OEFG yields accurate results.

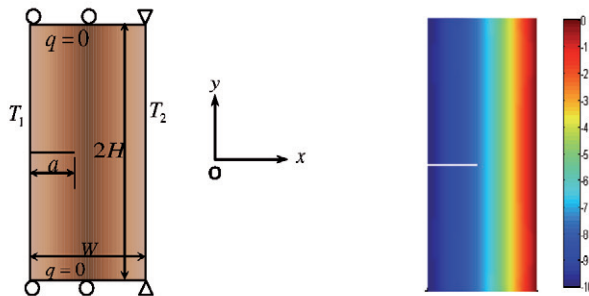


Fig.7.13 Adiabatic edge crack(a)Problem geometry (b)Temperature distribution($^\circ\text{C}$)

To generate accurate results conventional EFGM required 800 nodal points and in the previous works by KC and Kim using FEM[113] 1001 nodes were used, similarly in the work done by Goli et al.[106] using XFEM around 500 nodes were used. The OEFG formulation enabled accurate results by using only 200 nodes.

The solution of the above problem establishes the prowess of OEFG in simulating thermal fracture in FGMs in reduced computational time with adequate accuracy in results.

In another problem a rectangular FGM domain with dimensions ($W = 0.5\text{m}$ and $H = 0.5\text{m}$) along with an edge crack of length $a = 0.3\text{m}$ under isothermal conditions is

considered as shown in Fig.7.14(a). For this simulation extra nodes are defined on the crack surface as the crack is a part of essential boundary [50,114]. The crack surface is kept at $T_1 = -10^\circ\text{C}$ while the surrounding temperature is $T_2 = 0^\circ\text{C}$. The continuous temperature distribution is obtained in this case. The temperature profile at an inclination angle ($\alpha = 30^\circ$) is shown in Fig.7.14(b). This simulation is performed to test the efficiency of OEGF to simulate mixed mode condition of fracture.

Under the prescribed thermal loading and boundary conditions, the adiabatic edge crack exhibits a mode-I displacement. The values of mode-I SIF i.e. K_I has been calculated for different $\left(\frac{a}{W}\right)$ ratio. The EFGM and OEGF results are found in good agreement with the Ref.3 FEM solution by KC and Kim [113] as shown in Fig.7.15(a). The decrease in value of K_I with the increase in crack length is due to the gradation in material properties.

Fig.7.15(b) presents the plot of variation of K_I and K_{II} with inclination angle ($\alpha = 0^\circ - 60^\circ$) for single edge isothermal crack. The plot shows a decreasing trend in the values of K_I while the values of K_{II} surge which is quite predictable as the crack enters mixed mode conditions.

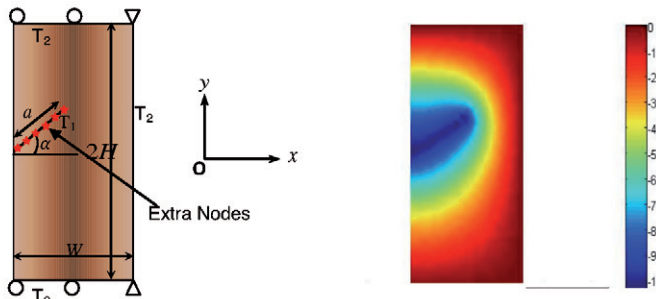


Fig.7.14 Isothermal inclined edge crack (a)Problem geometry (b)Temperature profile(${}^\circ\text{C}$) ($\alpha = 30^\circ$)

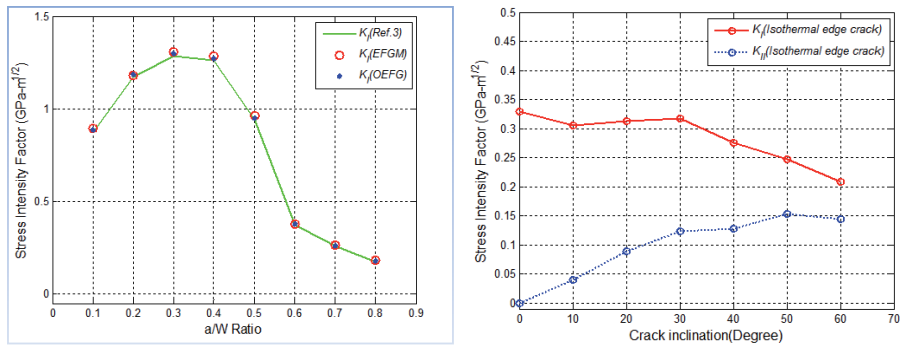


Fig.7.15 Variation of K_I and K_{II} for single edge crack (a) Adiabatic crack (b) Isothermal crack

CHAPTER 8

CONCLUSION AND FUTURE SCOPE

8.1 Conclusion

We have presented an overview of application of EFGM in fracture mechanics with the development that took place to improve the working capability of EFGM. The article presents the major developments and modifications in EFGM and their applicability to fracture problems and few examples taken in this work to show the prowess of this method. The book will provide researchers with a quick review of concise material for improving the analysis by combining the modifications that took place over the years for improving the accuracy and removing difficulties associated with EFGM. The work will help in comprehending the modifications in EFGM for improving its capability and also guides in selection of best procedures for implementing EFGM to fracture problems.

The first step in the analysis of a problem using EFGM is construction of shape function and enforcement of boundary conditions. We have elaborated the most common procedures for construction of shape function and also given a mention to method like weighted orthogonal basis for removing difficulties associated with the derivation of shape function process. The article also covers other methods for shape function construction using radial basis function in conjugation with MLS approach but this method failed to reach desired accuracy in results.

The MLS shape functions lack Kronecker delta property hence enforcement of boundary conditions is difficult, also the use of Lagrange multiplier method leads to an escalation in number of unknowns which is troublesome for the solver. Many approaches to circumvent the use of Lagrange multiplier along with maintaining the satisfaction of essential boundary conditions have been discussed. From these approaches it is inferred that Lagrange multiplier approach provides best accuracy in results compared to other methods mentioned in the literature. The following comparisons can be drawn between Lagrange multiplier and other methods (i) the modified variational principle provided a set of banded equations but these equations are not necessarily positive-definite also it was somewhat less accurate than Lagrange multiplier method (ii) penalty method which leads to banded

positive-definite equations but did not provide desired accuracy (iii) transformation method for enforcement of boundary conditions is also not as accurate as Lagrange multiplier approach.

Many integration techniques have been summarized out of which background integration is most widely used as it is the most accurate way for constructing the discrete equations. The sub-triangulation technique as explained the article has been used to further improve the accuracy of integration.

In analyzing fracture problems discontinuities can be present in the domain the form of strong or weak discontinuities. In case of weak discontinuities domain partitioning approach is not efficient and produces misleading results whereas jump function approach can be called as best approach for handling material discontinuities. For handling strong discontinuities provided the enriched EFG formulations for analysis of fracture problems smoothening techniques for treating cracks and holes in the domain are discussed. Both intrinsic and extrinsic enrichment techniques offer significant reduction in number of unknowns required to obtain accurate solution by meshless method, the intrinsic enrichment is easy to program whereas extrinsic enrichment can provide better results for multiple crack simulations. The drawback of the extrinsic MLS enrichment is that it uses global enrichment in contrast to local enrichment typically employed in PU based methods. In comparison of smoothing techniques visibility criterion is best for cracks and see through technique is best for hole.

We have discussed the coupling of EFGM with other methods like FEM, FFEM and RPIM. These coupled methods provide significant reduction in time and cost of analysis. These coupling procedures cover the inherent flaws in EFGM and provide benefits in maintaining the desired accuracy as well as removing the troublesome difficulties of standard EFGM. The combination of these methods provide a much better prospect for future in the field of fracture mechanics.

8.2 Future Scope

EFGM has been successful in establishing itself as an efficient and accurate method for analysis of fracture problems and its capability to handle large deformations with ease has provided a platform for its further development into a dedicated software based on meshless methods in the future. In terms of

competition from other techniques such as extended finite element method (XFEM) it is benefited by higher order continuity as smoother stress field approximations can be obtained in the singularity dominated zone.

EFGM as an efficient method for modeling cracks in FGMs and reflects its potential to solve a variety of practical fracture problems. The simplicity and accuracy of this implementation shows that it can be further extended to study and analyze the fracture in graded materials with multi-loading and complex geometry conditions.

References

- [1] N. Moës, J. Dolbow, T. Belytschko, A finite element method for crack growth without remeshing, *Int. J. Numer. Meth. Engng.* 46 (1999) 131–150. doi:10.1002/(SICI)1097-0207(19990910)46:1<131::AID-NME726>3.0.CO;2-J.
- [2] T. Belytschko, T. Black, Elastic crack growth in finite elements with minimal remeshing, *Int. J. Numer. Methods Eng.* 45 (1999) 601–620. doi:10.1002/(sici)1097-0207(19990620)45:5<601::aid-nme598>3.0.co;2-s.
- [3] E. Budyn, G. Zi, N. Moes, T. Belytschko, A method for multiple crack growth in brittle materials without remeshing, *Int. J. Numer. Methods Eng.* 61 (2004) 1741–1770. doi:10.1002/nme.1130.
- [4] A. Asadpoure, S. Mohammadi, A. Vafai, Crack analysis in orthotropic media using the extended finite element method, *Thin-Walled Struct.* 44 (2006) 1031–1038. doi:10.1016/j.tws.2006.07.007.
- [5] S. Bordas, V.P. Nguyen, C. Dunant, A. Guidoum, H. Nguyen-Dang, An extended finite element library, *Int. J. Numer. Methods Eng.* 71 (2007) 703–732. doi:10.1002/nme.
- [6] G.R. Liu, M.B. Liu, Smoothed Particle Hydrodynamics: A Meshfree Particle Method, 2003. doi:10.1142/9789812564405.
- [7] P.J. Cossins, Smoothed Particle Hydrodynamics, *Reports Prog. Phys.* 68 (2005) 55. doi:10.1088/0034-4885/68/8/R01.
- [8] M.B. Liu, G.R. Liu, Smoothed particle hydrodynamics (SPH): An overview and recent developments, 2010. doi:10.1007/s11831-010-9040-7.
- [9] J.H. Jeong, M.S. Jhon, J.S. Halow, J. Van Osdol, Smoothed particle hydrodynamics: Applications to heat conduction, *Comput. Phys. Commun.* 153 (2003) 71–84. doi:10.1016/S0010-4655(03)00155-3.
- [10] A.M. Tartakovsky, P. Meakin, Pore scale modeling of immiscible and miscible fluid flows using smoothed particle hydrodynamics, *Adv. Water Resour.* 29 (2006) 1464–1478. doi:10.1016/j.advwatres.2005.11.014.
- [11] L.D. Libersky, A.G. Petschek, T.C. Carney, J.R. Hipp, F. a. Allahdadi, High Strain Lagrangian Hydrodynamics, *J. Comput. Phys.* 109 (1993) 67–75. doi:10.1006/jcph.1993.1199.
- [12] T. Belytschko, Y.Y. Lu, L. Gu, Element free Galerkin methods, *Int. J. Numer. Methods Eng.* 37 (1994) 229–256. doi:10.1002/nme.1620370205.
- [13] T. Belytschko, L. Gu, Y.Y. Lu, Fracture and crack growth by element-free Galerkin methods., *Model. Simul. Mater. Sci. Eng.* 2 (1994) 519–534. doi:10.1088/0965-0393/2/3A/007.
- [14] R. Brighenti, Application of the element-free Galerkin meshless method to 3-D fracture mechanics problems, *Eng. Fract. Mech.* 72 (2005) 2808–2820.

doi:10.1016/j.engfracmech.2005.06.002.

- [15] I. V. Singh, B.K. Mishra, M. Pant, An enrichment based new criterion for the simulation of multiple interacting cracks using element free Galerkin method, *Int. J. Fract.* 167 (2010) 157–171. doi:10.1007/s10704-010-9536-z.
- [16] K. Sharma, V. Bhasin, I.V. Singh, B.K. Mishra, R.K. Singh, Simulation of Bi-metallic Interfacial Cracks Using Element Free Galerkin Method, *Procedia Eng.* 86 (2014) 685–692. doi:10.1016/j.proeng.2014.11.070.
- [17] A. Jameel, G.A. Harmain, Fatigue crack growth in presence of material discontinuities by EFGM, *Int. J. Fatigue.* 81 (2015) 105–116. doi:10.1016/j.ijfatigue.2015.07.021.
- [18] D. Shepard, A two-dimensional interpolation function for irregularly-spaced data, 23rd ACM Natl. Conf. (1968) 517–524. doi:10.1145/800186.810616.
- [19] G. Yagawa, T. Furukawa, Recent developments of free mesh method, *Int. J. Numer. Methods Eng.* 47 (2000) 1419–1443. doi:10.1002/(SICI)1097-0207(20000320)47:8<1419::AID-NME837>3.0.CO;2-E.
- [20] F.C. Günther, W.K. Liu, Implementation of boundary conditions for meshless methods, *Comput. Methods Appl. Mech. Eng.* 163 (1998) 205–230. doi:10.1016/S0045-7825(98)00014-0.
- [21] T. Belytschko, Y.Y. Lu, L. Gu, Crack propagation by element free Galerkin methods, in: Proc. 1993 ASME Winter Annu. Meet. Novemb. 28, 1993 - December 3, 1993: pp. 191–205.
- [22] P. Lancaster, K. Salkauskas, Surfaces generated by moving least squares methods, *Math. Comput.* 37 (1981) 141–141. doi:10.1090/S0025-5718-1981-0616367-1.
- [23] Y.Y. Lu, T. Belytschko, L. Gu, A new implementation of the element free Galerkin method, *Comput. Methods Appl. Mech. Eng.* 113 (1994) 397–414. doi:10.1016/0045-7825(94)90056-6.
- [24] Z. Zhang, K.M. Liew, Y. Cheng, Y.Y. Lee, Analyzing 2D fracture problems with the improved element-free Galerkin method, *Eng. Anal. Bound. Elem.* 32 (2008) 241–250. doi:10.1016/j.enganabound.2007.08.012.
- [25] Å. Björck, Numerics of Gram-Schmidt orthogonalization, *Linear Algebra Appl.* 197–198 (1994) 297–316. doi:10.1016/0024-3795(94)90493-6.
- [26] L. Gavete, S. Falcon, J.C. Bellido, Dirichlet Boundary Conditions in Element Free Galerkin method, in: Eur. Congr. Comput. Methods Appl. Sci. Eng., Barcelona, 2000: pp. 1–14.
- [27] S.-H. Lee, Y.-C. Yoon, Numerical prediction of crack propagation by an enhanced element-free Galerkin method, *Nucl. Eng. Des.* 227 (2004) 257–271. doi:10.1016/j.nucengdes.2003.10.007.
- [28] J. Xu, T. Belytschko, Discontinuous Radial Basis Function Approximations for Meshfree Methods, *Meshfree Methods Partial Differ. Equations II.* 43

- (2005) 231–243. doi:10.1007/b138605.
- [29] N.T. Nguyen, T.Q. Bui, C. Zhang, T.T. Truong, Crack growth modeling in elastic solids by the extended meshfree Galerkin radial point interpolation method, *Eng. Anal. Bound. Elem.* 44 (2014) 87–97. doi:10.1016/j.enganabound.2014.04.021.
 - [30] T. Belytschko, T. Rabczuk, A. Huerta, S. Fernández-Méndez, Meshfree Methods, *Encycl. Comput. Mech.* (2004) 1–48.
 - [31] P.H. Wen, M.H. Aliabadi, Y.W. Liu, Meshless method for crack analysis in functionally graded materials with enriched radial base functions., *Comput. Model. Eng. Sci.* 30 (2008) 133–147.
 - [32] O.F. Valencia, F.J. Gómez-Escaloniella, J.L. Díez, Influence of selectable parameters in element-free Galerkin method: One-dimensional bar axially loaded problem, *Proc. Inst. Mech. Eng. Part C J. Mech. Eng. Sci.* . 222 (2008) 1621–1633. doi:10.1243/09544062JMES782.
 - [33] O.F. Valencia, F.J. Gómez-Escaloniella, J. López-Díez, The influence of selectable parameters in the element-free Galerkin method: A one-dimensional beam-in-bending problem, *Proc. Inst. Mech. Eng. Part C J. Mech. Eng. Sci.* . 223 (2009) 1579–1590. doi:10.1243/09544062JMES1198.
 - [34] L.W. Cordes, B. Moran, Treatment of material discontinuity in the Element-Free Galerkin method, *Comput. Methods Appl. Mech. Eng.* 139 (1996) 75–89. doi:10.1016/S0045-7825(96)01080-8.
 - [35] M. Pant, K. Sharma, A Comparative Study of Modeling Material Discontinuity Using Element Free Galerkin Method, *Procedia Eng.* 86 (2014) 758–766. doi:10.1016/j.proeng.2014.11.095.
 - [36] R.C. Batra, M. Porfiri, D. Spinello, Treatment of material discontinuity in two meshless local Petrov-Galerkin (MLPG) formulations of axisymmetric transient heat conduction, *Int. J. Numer. Methods Eng.* 61 (2004) 2461–2479. doi:10.1002/nme.1156.
 - [37] T. Rabczuk, S. Bordas, G. Zi, A three-dimensional meshfree method for continuous multiple-crack initiation, propagation and junction in statics and dynamics, *Comput. Mech.* 40 (2007) 473–495. doi:10.1007/s00466-006-0122-1.
 - [38] M. Pant, I.V. Singh, B.K. Mishra, Evaluation of mixed mode stress intensity factors for interface cracks using EFGM, *Appl. Math. Model.* 35 (2011) 3443–3459. doi:10.1016/j.apm.2011.01.010.
 - [39] G. Ventura, J.X. Xu, T. Belytschko, A vector level set method and new discontinuity approximations for crack growth by EFG, *Int. J. Numer. Methods Eng.* 54 (2002) 923–944. doi:10.1002/nme.471.
 - [40] M. Fleming, Y. Chu, B. Moran, T. Belytschko, Enriched element-free Galerkin methods for crack tip fields, *Int. J. Numer. Methods Eng.* 40 (1997)

1483–1504. doi:10.1002/(SICI)1097-0207(19970430)40:8<1483::AID-NME123>3.0.CO;2-6.

- [41] T. Belytschko, Y. Krongauz, M. Fleming, D. Organ, W.K. Snm Liu, Smoothing and accelerated computations in the element free Galerkin method, *J. Comput. Appl. Math.* 74 (1996) 111–126. doi:10.1016/0377-0427(96)00020-9.
- [42] T. Belytschko, D. Organ, Y. Krongauz, A coupled finite element-element-free Galerkin method, *Comput. Mech.* 17 (1995) 186–195. doi:10.1007/BF00364080.
- [43] A. Asadpoure, S. Mohammadi, A. Vafai, Modeling crack in orthotropic media using a coupled finite element and partition of unity methods, *Finite Elem. Anal. Des.* 42 (2006) 1165–1175. doi:10.1016/j.finel.2006.05.001.
- [44] K.N. Rajesh, B.N. Rao, Two-dimensional analysis of anisotropic crack problems using coupled meshless and fractal finite element method, *Int. J. Fract.* 164 (2010) 285–318. doi:10.1007/s10704-010-9496-3.
- [45] R.M. Reddy, B.N. Rao, Continuum shape sensitivity analysis of mixed-mode fracture using fractal finite element method, *Eng. Fract. Mech.* 75 (2008) 2860–2906. doi:10.1016/j.engfracmech.2008.01.001.
- [46] Y. Cao, L. Yao, Y. Yin, New treatment of essential boundary conditions in EFG method by coupling with RPIM, *Acta Mech. Solida Sin.* 26 (2013) 302–316. doi:10.1016/S0894-9166(13)60028-2.
- [47] T. Belytschko, L. Gu, Y.Y. Lu, Fracture and crack growth by element free Galerkin methods, *Model. Simul. Mater. Sci. Eng.* 2 (1994) 519–534. doi:10.1088/0965-0393/2/3A/007.
- [48] T. Belytschko, Y.Y. Lu, L. Gu, M. Tabbara, Element-free galerkin methods for static and dynamic fracture, *Int. J. Solids Struct.* 32 (1995) 2547–2570. doi:10.1016/0020-7683(94)00282-2.
- [49] J.-S. Chen, H.-P. Wang, New boundary condition treatments in meshfree computation of contact problems, *Comput. Methods Appl. Mech. Eng.* 187 (2000) 441–468. doi:10.1016/S0045-7825(00)80004-3.
- [50] M. Pant, I.V. Singh, B.K. Mishra, Numerical simulation of thermo-elastic fracture problems using element free Galerkin method, *Int. J. Mech. Sci.* 52 (2010) 1745–1755. doi:10.1016/j.ijmecsci.2010.09.008.
- [51] S. Garg, M. Pant, Numerical simulation of adiabatic and isothermal cracks in functionally graded materials using optimized element-free Galerkin method, *J. Therm. Stress.* 0 (2017) 1–20. doi:10.1080/01495739.2017.1287534.
- [52] V.P. Nguyen, T. Rabczuk, S. Bordas, M. Duflot, Meshless methods: A review and computer implementation aspects, *Math. Comput. Simul.* 79 (2008) 763–813. doi:10.1016/j.matcom.2008.01.003.
- [53] G. Liu, D. Karamanlidis, Mesh Free Methods: Moving Beyond the Finite

- Element Method, *Appl. Mech. Rev.* 56 (2003) B17. doi:10.1115/1.1553432.
- [54] T. Fries, H. Matthias, Classification and overview of meshfree methods, Brunswick, Germany, 2004.
- [55] J. Dolbow, T. Belytschko, Numerical integration of the Galerkin weak form in meshfree methods, *Comput. Mech.* 23 (1999) 219–230. doi:10.1007/s004660050403.
- [56] G.W. Stewart, The decompositional approach to matrix computation, *Comput. Sci. Eng.* 2 (2000) 50–59. doi:10.1109/5992.814658.
- [57] T. Belytschko, Y. Krongauz, D. Organ, M. Fleming, P. Krysl, Meshless Methods: An Overview and Recent Developments, *Comput. Method Appl. Mech. Eng.* 139 (1996) 3–47. doi:10.1016/S0045-7825(96)01078-X.
- [58] I. Kaljevic, S. Saigal, An improved element free Galerkin formulation, *Int. J. Numer. Methods Eng.* 40 (1997) 2953–2974. doi:10.1002/(SICI)1097-0207(19970830)40:16<2953::AID-NME201>3.0.CO;2-S.
- [59] B.N. Rao, S. Rahman, An efficient meshless method for fracture analysis of cracks, *Comput. Mech.* 26 (2000) 398–408. doi:10.1007/s004660000189.
- [60] D. Organ, M. Fleming, T. Terry, T. Belytschko, Continuous meshless approximations for nonconvex bodies by diffraction and transparency, *Comput. Mech.* 18 (1996) 225–235. doi:10.1007/BF00369940.
- [61] M. Duflot, H. Nguyen-Dang, A meshless method with enriched weight functions for fatigue crack growth, *Int. J. Numer. Methods Eng.* 59 (2004) 1945–1961. doi:10.1002/nme.948.
- [62] M. Duflot, A meshless method with enriched weight functions for three-dimensional crack propagation, *Int. J. Numer. Methods Eng.* 65 (2006) 1970–2006. doi:10.1002/nme.1530.
- [63] R.L. Hardy, Multiquadric equations of topography and other irregular surfaces, *J. Geophys. Res.* 76 (1971) 1905. doi:10.1029/JB076i008p01905.
- [64] P.H. Wen, M.H. Aliabadi, A variational approach for evaluation of stress intensity factors using the element free Galerkin method, *Int. J. Solids Struct.* 48 (2011) 1171–1179. doi:10.1016/j.ijsolstr.2011.01.002.
- [65] M. a. Golberg, C.S. Chen, S.R. Karur, Improved multiquadric approximation for partial differential equations, *Eng. Anal. Bound. Elem.* 18 (1996) 9–17. doi:10.1016/S0955-7997(96)00033-1.
- [66] T. Zhu, S.N. Atluri, A modified collocation method and a penalty formulation for enforcing the essential boundary conditions in the element free Galerkin method, *Comput. Mech.* 21 (1998) 211–222. doi:10.1007/s004660050296.
- [67] T. Belytschko, M. Fleming, Smoothing, enrichment and contact in the element-free Galerkin method, *Comput. Struct.* 71 (1999) 173–195. doi:10.1016/S0045-7949(98)00205-3.

- [68] G. Ventura, An augmented Lagrangian approach to essential boundary conditions in meshless methods, *Int. J. Numer. Methods Eng.* 53 (2002) 825–842. doi:10.1002/nme.314.
- [69] P. Krysl, T. Belytschko, Element-free Galerkin method: Convergence of the continuous and discontinuous shape functions, *Comput. Methods Appl. Mech. Eng.* 148 (1997) 257–277. doi:10.1016/s0045-7825(96)00007-2.
- [70] D.C. Simkins, S. Li, Meshfree simulations of thermo-mechanical ductile fracture, *Comput. Mech.* 38 (2006) 235–249. doi:10.1007/s00466-005-0744-8.
- [71] I. V Singh, B.K. Mishra, M. Pant, A modified intrinsic enriched element free Galerkin method for multiple cracks simulation, *Mater. Des.* 31 (2010) 628–632. doi:10.1016/j.matdes.2009.06.002.
- [72] T. Rabczuk, P.M. Areias, T. Belytschko, A simplified mesh-free method for shear bands with cohesive surfaces, *Int. J. Numer. Methods Eng.* 69 (2007) 993–1021. doi:10.1002/nme.1797.
- [73] T. Rabczuk, G. Zi, A Meshfree Method based on the Local Partition of Unity for Cohesive Cracks, *Comput. Mech.* 39 (2007) 743–760. doi:10.1007/s00466-006-0067-4.
- [74] G. Zi, T. Rabczuk, W. Wall, Extended meshfree methods without branch enrichment for cohesive cracks, *Comput. Mech.* 40 (2006) 367–382. doi:10.1007/s00466-006-0115-0.
- [75] G.R. Liu, Y.T. Gu, A meshfree method: meshfree weak-strong (MWS) form method, for 2-D solids, *Comput. Mech.* 33 (2004) 2–14. doi:10.1007/s00466-003-0477-5.
- [76] I.V. Singh, B.K. Mishra, M. Pant, An efficient partial domain enriched element free Galerkin method criterion for cracks in nonconvex domains, *Int. J. Model. Simulation. Sci. Comput.* 2 (2011) 317–336.
- [77] A. Asadpoure, S. Mohammadi, Developing new enrichment functions for crack simulation in orthotropic media by the extended finite element method, *Int. J. Numer. Methods Eng.* 69 (2007) 2150–2172. doi:10.1002/nme.1839.
- [78] S.S. Ghorashi, S. Mohammadi, S.-R. Sabbagh-Yazdi, Orthotropic enriched element free Galerkin method for fracture analysis of composites, *Eng. Fract. Mech.* 78 (2011) 1906–1927. doi:10.1016/j.engfracmech.2011.03.011.
- [79] W.A. Wooster, *Theory of elasticity of an anisotropic elastic body* by S. G. Lekhnitskii, *Acta Crystallogr.* 17 (1964) 793–793. doi:10.1107/S0365110X64002171.
- [80] M. Pant, I.V. Singh, B.K. Mishra, A novel enrichment criterion for modeling kinked cracks using element free Galerkin method, *Int. J. Mech. Sci.* 68 (2013) 140–149. doi:10.1016/j.ijmecsci.2013.01.008.
- [81] R. Namakian, H.M. Shodja, M. Mashayekhi, Fully enriched weight functions

- in mesh-free methods for the analysis of linear elastic fracture mechanics problems, *Eng. Anal. Bound. Elem.* 43 (2014) 1–18. doi:10.1016/j.enganabound.2014.02.006.
- [82] S. Fernández-Méndez, A. Huerta, Imposing essential boundary conditions in mesh-free methods, *Comput. Methods Appl. Mech. Eng.* 193 (2004) 1257–1275. doi:10.1016/j.cma.2003.12.019.
 - [83] Y. Gu, G. Liu, Meshless Methods Coupled with Other Numerical Methods, *Tsinghua Sci. Technol.* 10 (2005) 8–15. doi:Doi: 10.1016/s1007-0214(05)70003-1.
 - [84] A. Huerta, S. Fernández, Enrichment and coupling of the finite element and meshless methods, *Int. J. Numer. Methods Eng.* 48 (2000) 1615–1636. doi:10.1002/1097-0207(20000820)48:11<1615::AID-NME883>3.0.CO;2-S.
 - [85] C.P. Wu, K.H. Chiu, R.Y. Jiang, A meshless collocation method for the coupled analysis of functionally graded piezo-thermo-elastic shells and plates under thermal loads, *Int. J. Eng. Sci.* 56 (2012) 29–48. doi:10.1016/j.ijengsci.2012.03.001.
 - [86] B.N. Rao, S. Rahman, A coupled meshless-finite element method for fracture analysis of cracks, *Int. J. Press. Vessel. Pip.* 78 (2001) 647–657. doi:10.1016/S0308-0161(01)00076-X.
 - [87] I. V. Singh, B.K. Mishra, M. Brahmkar, V. Bhasin, K. Sharma, I.A. Khan, Numerical Simulations of 3-D Cracks Using Coupled EFGM and FEM, *Int. J. Comput. Methods Eng. Sci. Mech.* 15 (2014) 227–231. doi:10.1080/15502287.2014.882438.
 - [88] Q.Z. Xiao, M. Dhanasekar, Coupling of FE and EFG using collocation approach, *Adv. Eng. Softw.* 33 (2002) 507–515. doi:10.1016/S0965-9978(02)00069-8.
 - [89] S. Kumar, I. V. Singh, B.K. Mishra, A multigrid coupled (FE-EFG) approach to simulate fatigue crack growth in heterogeneous materials, *Theor. Appl. Fract. Mech.* 72 (2014) 121–135. doi:10.1016/j.tafmec.2014.03.005.
 - [90] H. Pathak, A. Singh, I.V. Singh, Simulation of 3-D Thermo-elastic Fracture Problems Using Coupled FE-EFG Approach, *Procedia Mater. Sci.* 6 (2014) 1927–1935. doi:10.1016/j.mspro.2014.07.226.
 - [91] S. Cheung, A.R. Luxmoore, A finite element analysis of stable crack growth in an aluminium alloy, *Eng. Fract. Mech.* 70 (2003) 1153–1169. doi:10.1016/S0013-7944(02)00093-0.
 - [92] J.G. Wang, G.R. Liu, A point interpolation meshless method based on radial basis functions, *Int. J. Numer. Methods Eng.* 54 (2002) 1623–1648. doi:10.1002/nme.489.
 - [93] G.R. Liu, Y.T. Gu, An Introduction to Meshfree Methods and Their Programming, 2010. doi:10.1007/1-4020-3468-7.

- [94] S. Kosaraju, V.G. Anne, B.B. Popuri, Taguchi Analysis on Cutting Forces and Temperature in Turning Titanium Ti-6Al-4V, *Int. J. Mech. Ind. Eng.* 1 (2012) 55–59.
- [95] H. Wang, Y. Liu, P. Yang, R. Wu, Y. He, Parametric study and optimization of H-type finned tube heat exchangers using Taguchi method, *Appl. Therm. Eng.* 103 (2016) 128–138. doi:10.1016/j.applthermaleng.2016.03.033.
- [96] H. Salari-Rad, M. Rahimi-Dizadji, S. Rahimi-Pour, M. Delforouzi, Meshless EFG Simulation of Linear Elastic Fracture Propagation Under Various Loadings, *Arab. J. Sci. Eng.* 36 (2011) 1381–1392. doi:10.1007/s13369-011-0125-x.
- [97] S. De, K.J. Bathe, The method of finite spheres with improved numerical integration, *Comput. Struct.* 79 (2001) 2183–2196. doi:10.1016/S0045-7949(01)00124-9.
- [98] M.P. Elizalde-Gonzalez, L.E. Garcia-Diaz, Application of a Taguchi L16 orthogonal array for optimizing the removal of Acid Orange 8 using carbon with a low specific surface area, *Chem. Eng. J.* 163 (2010) 55–61. doi:10.1016/j.cej.2010.07.040.
- [99] J. Chen, C. Wu, S. Yoon, Y. You, A stabilized conforming nodal integration for Galerkin mesh-free methods, *Int. J. Numer. Methods Eng.* 50 (2001) 435–466. doi:10.1002/1097-0207(20010120)50:2<435::AID-NME32>3.0.CO;2-A.
- [100] N. Sukumar, N. Moës, B. Moran, T. Belytschko, Extended finite element method for three-dimensional crack modelling, *Int. J. Numer. Methods Eng.* 48 (2000) 1549–1570. doi:10.1002/1097-0207(20000820)48:11<1549::AID-NME955>3.0.CO;2-A.
- [101] J. Dolbow, N. Moës, T. Belytschko, Discontinuous enrichment in finite elements with a partition of unity method, *Finite Elem. Anal. Des.* 36 (2000) 235–260. doi:10.1016/S0168-874X(00)00035-4.
- [102] J.R. Rice, A Path Independent Integral and the Approximate Analysis of Strain Concentration by Notches and Cracks, *J. Appl. Mech.* 35 (1968) 379. doi:10.1115/1.3601206.
- [103] B. Moran, C.F. Shih, Crack tip and associated domain integrals from momentum and energy balance, *Eng. Fract. Mech.* 27 (1987) 615–642. doi:10.1016/0013-7944(87)90155-X.
- [104] J.-H. Kim, G.H. Paulino, The interaction integral for fracture of orthotropic functionally graded materials: evaluation of stress intensity factors, *Int. J. Solids Struct.* 40 (2003) 3967–4001. doi:10.1016/S0020-7683(03)00176-8.
- [105] B.N. Rao, S. Rahman, Mesh-free analysis of cracks in isotropic functionally graded materials, *Eng. Fract. Mech.* 70 (2003) 1–27. doi:10.1016/S0013-7944(02)00038-3.

- [106] E. Goli, H. Bayesteh, S. Mohammadi, Mixed mode fracture analysis of adiabatic cracks in homogeneous and non-homogeneous materials in the framework of partition of unity and the path-independent interaction integral, Eng. Fract. Mech. 131 (2014) 100–127. doi:10.1016/j.engfracmech.2014.07.013.
- [107] J. Sladek, V. Sladek, Evaluation of T-stresses and stress intensity factors in stationary thermoelasticity by the coservation integral method, Int. J. Fract. 86 (1997) 199–219.
- [108] J.-H. Kim, G.H. Paulino, Consistent Formulations of the Interaction Integral Method for Fracture of Functionally Graded Materials, J. Appl. Mech. 72 (2005) 351. doi:10.1115/1.1876395.
- [109] S. Garg, M. Pant, Numerical simulation of thermal fracture in functionally graded materials using element-free Galerkin method, Sadhana - Acad. Proc. Eng. Sci. 42 (2016) 417–431. doi:10.1007/s12046-017-0612-1.
- [110] N. Sukumar, Z.Y. Huang, J.H. Prevost, Z. Suo, J.-H. Prévost, Z. Suo, Partition of unity enrichment for bimaterial interface cracks, Int. J. Numer. Methods Eng. 59 (2004) 1075–1102. doi:10.1002/nme.902.
- [111] T. Matsumoto, M. Tanaka, R. Obara, Computation of stress intensity factors of interface cracks based on interaction energy release rates and BEM sensitivity analysis, Eng. Fract. Mech. 65 (2000) 683–702. doi:10.1016/S0013-7944(00)00005-9.
- [112] X.Y. Liu, Q.Z. Xiao, B.L. Karihaloo, XFEM for direct evaluation of mixed mode SIFs in homogeneous and bi-materials, Int. J. Numer. Methods Eng. 59 (2004) 1103–1118. doi:10.1002/nme.906.
- [113] A. KC, J.-H. Kim, Interaction integrals for thermal fracture of functionally graded materials, Eng. Fract. Mech. 75 (2008) 2542–2565. doi:10.1016/j.engfracmech.2007.07.011.
- [114] M. Duflot, The extended finite element method in thermoelastic fracture mechanics, Int. J. Numer. Methods Eng. 74 (2008) 827–847. doi:10.1002/nme.2197.



yes I want morebooks!

Buy your books fast and straightforward online - at one of the world's fastest growing online book stores! Environmentally sound due to Print-on-Demand technologies.

Buy your books online at
www.get-morebooks.com

Kaufen Sie Ihre Bücher schnell und unkompliziert online – auf einer der am schnellsten wachsenden Buchhandelsplattformen weltweit!
Dank Print-On-Demand umwelt- und ressourcenschonend produziert.

Bücher schneller online kaufen
www.morebooks.de

OmniScriptum Marketing DEU GmbH
Bahnhofstr. 28
D - 66111 Saarbrücken
Telefax: +49 681 93 81 567-9

info@omnascriptum.com
www.omnascriptum.com



